

ABSTRACT

Title of dissertation: Construction, Optimization, and Applications
of a Small Trapped-Ion Quantum Computer

Kevin Antony Landsman
Doctor of Philosophy, 2019

Dissertation directed by: Professor Christopher Monroe
Department of Physics

A large-scale quantum computer will have the ability to solve many computational problems beyond the capabilities of today's most powerful computers. Significant efforts to build such a computer are underway, many of which are small prototypes that are believed to be extensible to larger systems. Such systems, like the one in this thesis built off of $^{171}\text{Yb}^+$ ions, are enticing scientific endeavors for their potential to inform the production of large-scale systems, as well as the interesting experiments they can perform. In this work, experimental research is presented on both topics: scalability as well as compelling computations.

The first half of this thesis discusses building and optimizing a quantum computer to have high-fidelity qubit operations. An experimental architecture that allows for individual addressing and individual detection of qubits is presented alongside a discussion of errors and error-reduction. We derive the coherent manipulation of qubits using Raman lasers for rotational gates and the criteria necessary for multi-qubit entangling gates. Methods for efficiently fulfilling these criteria are presented

with experimental data. Lastly, we consider coherence-related properties of the system necessary to perform these operations and how they can be experimentally improved.

The second half of the thesis features three experimental applications of the quantum computer: quantifying quantum scrambling, applying a quantum error correction code, and measuring Rényi entropy. Quantum scrambling is the coherent delocalization of information through a quantum system and is notably difficult to quantify experimentally. We present an efficient scheme to measure it using quantum teleportation. Quantum error correction is a set of techniques for mitigating the effect of imperfect operations performed on a quantum computer, and we demonstrate some of these techniques in order to fault-tolerantly prepare a logical qubit. Lastly, Rényi entropy is an information theoretic quantity that can be used to directly quantify the amount of entanglement in a system. We present a method for measuring it efficiently using a quantum gate known as a Fredkin gate.

CONSTRUCTION, OPTIMIZATION, AND APPLICATIONS OF A SMALL TRAPPED-ION QUANTUM COMPUTER

by

Kevin Antony Landsman

Dissertation submitted to the Faculty of the Graduate School of the
University of Maryland, College Park in partial fulfillment
of the requirements for the degree of
Doctor of Philosophy
2019

Advisory Committee:

Professor Christopher Monroe, Chair/Advisor

Professor Mohammad Hafezi, Co-Advisor

Professor Jeffrey Bub

Professor Howard Milchberg

Professor Thomas E. Murphy

© Copyright by
Kevin Antony Landsman
2019

for Alana

Acknowledgements

First and foremost, I would like to thank my advisor, Chris Monroe. Chris did all of the things you hoped for in an advisor. He offered great scientific guidance, gave me the opportunity to work on a world-class experiment, surrounded me with smart scientists, and had me attend enriching academic conferences. But above all, I thank Chris for being a generous advisor who was respectful and kind to me.

Norbert Linke was a constant presence throughout my doctoral work, to whom I am *exceedingly* grateful. His mastery of trapped ion systems pushed our experiment to great heights that benefited us all greatly. His patient, didactic spirit taught me nearly everything I know about operating and building atomic physics experiments. His friendship was a welcome bonus, as well.

Caroline Figgatt and Shantanu Debnath were the graduate students with whom I worked most closely with. I was very lucky to spend time with these hard-working, friendly people. Their love of science and dedication to research was inspiring. In the beginning of my time in the lab, Shantanu was a great supervisor who got me engaged in the research very early on. I owe him *much* thanks as all of the work in this dissertation was done on an experiment that he had a huge role in building. I spent more time with Caroline than any other student, and I enjoyed her friendship a great deal as we solved many problems in tandem. She challenged me to be a better scientist and a better person. After they left, Daiwei Zhu started working with me. I enjoyed seeing Daiwei dive deeply into many aspects of our work and find places for improvement. His fervor for understanding the depths of our work often generated wonderful discussions.

Towards the end of my time in the lab, I split my time and worked in two laboratories. One lab lead by students Cinthia Huerta, Nhung Nguyen, and Mika Chmielewski. And the other featured Kristi Beck, Laird Egan, Drew Risinger, Michael Goldman, and Marko Cetina. Though brief, I thoroughly enjoyed time spent with these people. In addition to these scientists, there are many more scientists who were in the ion trapping orbit at the University of Maryland who enriched my experience significantly.

I want to thank my parents, Dawn and David, for giving me a privileged upbringing full of opportunities and education. You supported me in all my endeavors and instilled into me a sense of duty, perseverance, and kindness that makes me the person I am today. You put me on a path to success, which has lead me to a doctorate in a field I am passionate about and a job I am excited for. Along with my brother and sister-in-law, Marc and Ariel, you all support me every single day with your unconditional love.

Last, but certainly not least, I want to thank my wonderful wife, Alana. You are the kindest and most giving person I know, and you were an amazing source of advice throughout my graduate studies. Just spending a few moments with you was enough to keep me grounded and content regardless of what was happening inside my laboratory. Without your presence, my life as a student would have been far more difficult and far less enjoyable. I view the completion of this dissertation, which is dedicated to you, as a promise to give to you and our family as much as you always give to me.

Table of Contents

Dedication	ii
Acknowledgments	iii
List of Tables	vii
List of Figures	viii
List of Abbreviations	xi
 I Building an Ion Trap Quantum Computer	 1
1 Introduction	2
1.1 Quantum Computers	2
1.2 Quantum Circuits	5
1.3 Thesis layout	7
2 Trapping Ytterbium Ions	9
2.1 Ytterbium Qubits	9
2.2 rf Paul Traps in Theory	11
2.2.1 Ultra-High Vacuum Systems	15
2.3 Trapping Ions in Practice	16
2.4 Loading the Ion Trap with Ytterbium Ions	17
2.5 Ytterbium Energy Levels	21
2.5.1 Doppler Cooling	21
2.5.2 Initialize	25
2.5.3 Detection	25
2.5.4 Experimental Setup for Detection	29
2.5.5 Other Methods for State Classification	36
2.6 Coulomb Crystals	40
2.6.1 Ion Positions	41
2.6.2 Phonon Modes	43

3	Coherent Ion-Laser Interactions	47
3.1	Coherent Qubit Operations	47
3.2	Raman Transitions	48
3.3	Exciting Motion Raman Transitions	57
3.4	Exciting Motion	61
3.5	Generating Entanglement	61
3.6	Digital Quantum Gates	64
3.7	Experimental Apparatus	70
3.7.1	Raman Frequency Comb	73
3.7.2	Coherent RF Control	78
3.8	Coherence	82
3.8.1	Laser Coherence	84
3.8.2	Phononic Coherence	87
3.9	Experimental Entangling Gates	91
3.9.1	Two-Qubit Entanglement	95
3.9.2	Amplitude Modulation (AM) Gates	97
3.9.3	Frequency Modulation (FM) Gates	100
3.10	Gates on Longer Chains	107
II	Applications	114
4	Quantum Scrambling	115
4.1	Background	115
4.2	Measuring Scrambling	118
4.3	Two Simultaneous Measurements	124
4.4	Experimental Setup	129
4.5	Results	135
5	Quantum Error Correction	141
5.1	Introduction	141
5.2	Experimental Effort	143
6	Measuring Rényi Entropy	155
6.1	Measuring Entanglement	155
6.2	Hamiltonian Mapping	160
6.3	Trotterization	163
6.4	Experimental Results	165
	Bibliography	171

List of Tables

5.1	A summary of results from preparing logical states and applying stabilizer measurements	152
-----	---	-----

List of Figures

Introduction	2
1.1 Classical vs. Quantum Bits	3
1.2 Toy Quantum Circuit	7
Trapping Ytterbium Ions	9
2.1 Photograph of trap	18
2.2 Photograph of trap along axis	18
2.3 Ytterbium ion level diagram	20
2.4 S-P transition utilities	24
2.5 Detection histogram	27
2.6 Displayed counts from PMT array	28
2.7 Measurement errors	34
2.8 Fidelity of measuring 7-qubit states	35
2.9 Comparing detection techniques	39
2.10 Photograph of a 17-ion chain.	39
2.11 Local phonon hopping	45
2.12 Motional modes depicted	45
Coherent Ion-Laser Interactions	47
3.1 Raman system level diagram	49
3.2 Rabi flopping on sideband-cooled ions	60
3.3 Gate identity for reducing experimental entanglement parameter	66
3.4 Another gate identity for reducing experimental entanglement parameter	67
3.5 Gate identity for SK1 composite pulses	67
3.6 Comparison of rotation gates with SK1 composite gate	69
3.7 Raman beam crosstalk onto neighboring ions	72
3.8 Fourier transform of pulsed lasers in a Raman scheme	77
3.9 Measuring phase of maximally entangled states	81
3.10 Basis transformation of an entangling	81

3.11	Ramsey experiments to measure coherence times	86
3.12	Circuit schematic for locking the rf voltage	89
3.13	Photograph of the circuit used for locking rf voltage	89
3.14	Measured values of the trap confinement over time with and without an rf voltage lock	90
3.15	Secular frequency versus position	93
3.16	9 ion sideband spectroscopy	94
3.17	Amplitude modulation gate profile	99
3.18	Frequency modulation gate profile	105
3.19	Frequency modulation gate performance	105
3.20	Frequency modulation gate robustness	106
3.21	Sideband spectroscopy on 17-Ion chain	111
3.22	Gate profile for entangling 2 qubits on a 17-Ion Chain	111
3.23	Low-fidelity gate performance on 17-ion chain	112
3.24	High-fidelity gate performance on 17-ion chain	113
Quantum Scrambling		115
4.1	Quantum circuit for measuring quantum scrambling using a telepor- tation protocol	123
4.2	Quantum circuit for measuring qubits in the Bell basis.	125
4.3	Quantum circuit for preparing two qubits in the $ \Psi^+\rangle$ Bell state. . . .	126
4.4	Quantum circuit for running a Grover's search variant of the scram- bling measurement circuit	128
4.5	Circuit for implementing unitary for Grover's search variant.	128
4.6	Rabi flopping on a sideband-cooled chain of nine ions	130
4.7	Gate sequence that affects a scrambling unitary #1	131
4.8	Gate sequence that affects a scrambling unitary #2	131
4.9	Optimized quantum circuit used to measure quantum scrambling . . .	134
4.10	Results from parameterizing both the amount of mismatch between \hat{U}_s and \hat{U}_s and the amount of quantum scrambling	136
4.11	Results from teleporting different basis states via quantum scrambling	139
4.12	Results from teleporting information with a Grover's search variant .	140
Quantum Error Correction		141
5.1	Circuit for preparing $ 00\rangle_L$	146
5.2	Error propagation example 1	146
5.3	Error propagation example 2	146
5.4	Measuring $ 00\rangle_L$	148
5.5	Stabilizer circuit S_X	150
5.6	Stabilizer circuit S_Z	150
5.7	Preparing $ 00\rangle_L$ and performing stabilizers	151
5.8	Error correction with miscalibrated gates	154

Measuring Rényi Entropy	155
6.1 State-to-state transfer matrix after applying a Fredkin gate	159
6.2 Circuit for measuring Rényi entropy	159
6.3 Quantum circuit for measuring Rényi entropy of the Fermi-Hubbard model	168
6.4 Experimental results of simulating the Fermi-Hubbard Hamiltonian as well as measuring its Rényi entropy	169

List of Abbreviations

AOM	Acousto-Optic Modulator
AWG	Arbitrary Waveform Generator
<i>CNOT</i>	Controlled-NOT gate
dc	Direct Current (also implies static or slowly varying)
EOM	Electro-Optic Modulator
FPGA	Field Programmable Gate Array
NA	Numerical Aperture
OTOC	Out of Time Order Correlator
PMT	Photo-Multiplier Tube
QEC	Quantum Error Correction
rf	Radio Frequency
SK1	1 st order Solovay-Kitaev composite pulse
SPAM	State Preparation And Measurement
TTL	Transistor-Transistor Logic
Yb	Ytterbium

Part I

Building an Ion Trap Quantum Computer

Chapter 1: Introduction

1.1 Quantum Computers

Quantum computers (QC's) leverage the laws of quantum mechanics to solve computational problems. While regular bits of information can be either 0 or 1, quantum bits (qubits) can be in a superposition of 0 and 1. Therefore, we can define a piece of information as having the state amplitudes:

$$|\psi\rangle = \alpha |0\rangle + \beta |1\rangle$$

At first glance, one might reduce this phenomenon to discrete values versus continuous values of 0's and 1's, as depicted in **Figure 1.1a** and b, but the reality is far deeper. α and β are complex numbers, and the likelihood of measuring the qubit in either state is not α or β , rather it is $|\alpha|^2$ or $|\beta|^2$. Therefore, we can define them

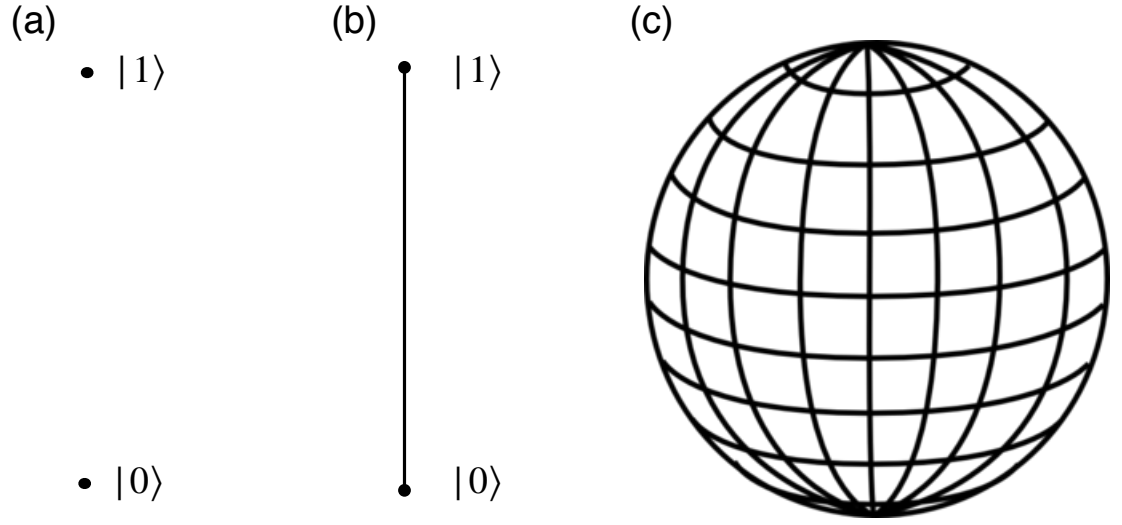


Figure 1.1: Comparison of information stored discretely (a), continuously using 1 variable (b), and continuously using two variables (c). Classical information is represented by (a) and two-level quantum information is represented in (c).

using trigonometry as:

$$\alpha = \cos\left(\frac{\theta}{2}\right)$$

$$\beta = e^{i\phi} \sin\left(\frac{\theta}{2}\right)$$

This formalism shows that **two** cyclic variables (θ and ϕ) are required to depict the qubit state, which is most naturally represented on a sphere (**Figure 1.1c**), which is commonly referred to as a Bloch sphere [1]. The distinction between classical and quantum information is very clear: two possible points on a line versus any possible point on a sphere. By re-imagining digital information in this way, exponentially more data can be stored on a register of qubits than on a similarly sized register of classical bits.

The other major distinction between classical and quantum computing is entanglement, a quantum mechanical correlation between two qubits that appears:

$$|\psi\rangle_{ent} = \cos(\frac{\theta}{2})|00\rangle + \sin(\frac{\theta}{2})e^{i\phi}|11\rangle$$

If two qubits are entangled, the amplitude and phase of their shared, correlated state cannot be discovered by measuring either qubit: both must be measured. In some sense, the two disparate qubits behave like a single qubit, which is why their state amplitudes are written here in a similar fashion as the single-qubit states. These entangled states were described in a seminal paper by Albert Einstein, Boris Podolsky, and Nathan Rosen where they explore the unique, “spooky” characteristics of entangled states [2]. An example of the spookiness of these states is demonstrated by considering how rotating the phase of the first qubit in the entangled state is completely equivalent to rotating the phase of the second qubit. This rotation is a local operation that is only experienced by qubit one, and yet its effect is shared by both qubits equally.

Quantum entanglement is a central topic in this thesis. In section 1, results from performing different methods for generating entanglement are presented. Then, in section 2, we present data from three quantum algorithms that require high-fidelity entangling gates. In one case, entanglement is used to mitigate inherent errors in the qubits. In the other two cases, entangling gates generate interesting information theoretic quantities we measured. Though both superposition and entanglement are the backbone of quantum computing, generating entanglement is

universally more difficult to do with high fidelity on large systems.

Thanks to both quantum superposition and quantum entanglement quantum computers can famously solve several extremely difficulty computational problems efficiently [3–5]. Since those early, seminar discoveries, many theoretical applications of quantum computers have developed in the fields of quantum physics [6], chemistry [7, 8], biology [9], materials science [10], and many more.

1.2 Quantum Circuits

The horizontal lines in a quantum circuit depict the operations performed on a specific qubit and the operations are indicated by symbols or text. These circuits are similar to digital logic circuits where lines represent wires that direct pieces of classical information into some logical operation. Examples of classical and quantum exclusive-or (XOR) gates are respectively depicted in **Figure 1.2a-b** alongside truth tables, which map out the relationship between input states to output states. There are several important distinctions between the classical and quantum versions of this gate that will help elucidate quantum computing generally.

In the classical version of the gate, the wires before the double curved lines carry the classical input information. The wires carry discrete voltages (either 3.3 V or 0 V) to denote the 1 state or the 0 state. The symbol denotes the XOR gate, which can be constructed by properly connecting transistors together and the single output would be contained by the wire to the right of the XOR. The XOR's output (Out1) is 1 if and only if one of the two input states (In1 or In2) are 1. If both or

neither are 1, then the output is 0. By looking at the output of the classical XOR, it is impossible to know the input states as it could always be one of two such states. Since information about the input states is lost at the end of the gate, it is simply dissipated as heat.

In the quantum version of the XOR, known more colloquially as a controlled-not (CNOT) gate, the “wires” are non-physical and only serve to denote the distinct qubits and the time-ordering of the qubit operations (time flows left to right). Here, the CNOT gate does not resemble a collection of transistors. Instead, the gate is a set of either laser or microwave pulses that manipulate the qubits in a controlled and coherent manner. This is the first major distinction between quantum and classical circuits: digital quantum logic is performed by coupling oscillating electromagnetic fields to the qubits instead of sending the classical bits through physical objects. For the experimental approach discussed in this thesis, the qubits are not connected by any physical object whatsoever and they only interact due to laser beams and Coulomb forces between them.

Another distinction between the classical and quantum circuits is the location of the information. As mentioned, classical circuits store information in wires that connect the logical components. In contrast, quantum information remains local to the physical qubit instead of flowing on a wire. Sometimes, as multi-qubit operations are performed on the quantum register, the information might be shared between qubits via entangled states. This non-locality is very nuanced because the information is physically stored in invisible correlations between qubits and can only be extracted by disentangling the qubits or measuring the qubits’ projections onto

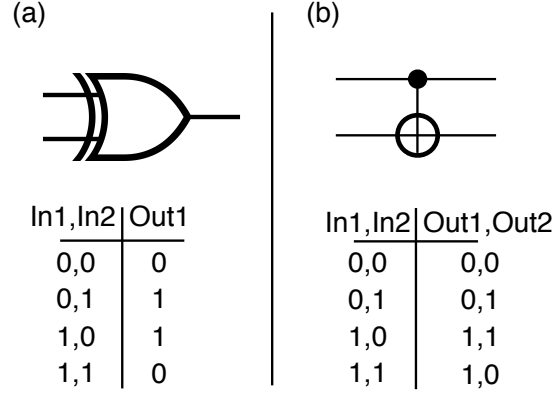


Figure 1.2: Two similar circuits are displayed. a) A classical XOR gate and its truth table. b) The quantum XOR gate more commonly known as a CNOT gate is presented with its truth table.

different axes of their entangled Bloch spheres. In many cases, the entanglement is undone at the end of a quantum circuit, and the information is returned to a local environment: a single qubit.

Despite these differences, the classical and quantum XOR have identical truth tables. In the quantum version, the classical output is repeated onto the second qubit's output state (Out2), while the first qubit (Out1) is unperturbed by the gate. This effects 4 distinct output states corresponding to 4 distinct input states.

1.3 Thesis layout

The experiments in this thesis were performed on a QC that was designed and assembled by myself and colleagues under the purview of our advisor, Christopher Monroe. Please see the thesis of Shantanu Debnath ([11]) for a more complete description of the physical hardware, and Caroline Figgatt's thesis ([12]) for an in-depth discussion of the experimental control software and its architectural structure.

In this thesis, I will first write about the disparate elements of the experiment that I was most involved with and their background. In chapter 2, I will introduce the devices and physics we use to create a qubit out of $^{171}\text{Yb}^+$ ions. In chapter 3, I will discuss how we coherently manipulate the qubits using a pulsed laser. In the remaining chapters, I focus on different computational problems that we studied using our quantum computer: quantum scrambling, quantum error correction, and measuring Rényi entropy in respective chapters 4, 5, and 6.

Chapter 2: Trapping Ytterbium Ions

2.1 Ytterbium Qubits

Ion trap quantum computing is the overarching theme of this thesis, yet it was only in the realm of imagination when ion trapping was invented. The early experiments using trapped ions focused on atomic physics phenomena [13–15]. Many of the techniques developed then are harnessed today to build QCs [16]. With the advent of commercially available lasers, these techniques have been nearly perfected and the typical criteria for quantum computing, known as the DiVincenzo criteria [17], are achieved on trapped ions. The DiVincenzo criteria and their realization on trapped ions are:

- I: initializing the qubits to a known state at the beginning of each experiment [18]
- II: relative coherence times are long compared with the time it takes to perform operations [18, 19]
- III: high-fidelity readout of the qubit register [20, 21]
- IV: high-fidelity control of the qubits [22]
- V: ability to extend the quantum computer to a large-scale system [23, 24]

Since every cooled, trapped ion features identical spectral properties, we can argue that ions are perfectly reproducible. This is a crucial observation for the scalability of QC's. Though it does not completely solve the scalability problem, it simplifies the requirements greatly. Other experimental candidates for quantum computing require engineered repeatability for success. Superconducting properties can change from qubit to qubit and between temperature cycling. To engineer systems of nitrogen-vacancy qubits, positioning of the nitrogen atom on the order of the diamond lattice spacing is required. In contrast, all trapped ion qubits will feature identical electronic transitions every time an ion is loaded into the trap. For the purposes of quantum computing, the most important atomic transition is the qubit transition, and there are many impressive, commonly-trapped candidates.

Some of the best trapped-ion qubits have hyperfine-split ground states that have microwave splittings and make wonderful qubits. $^{43}\text{Ca}^+$ ions can be truly insensitive to magnetic field fluctuations in the presence of 146 G magnetic fields [19]. $^{133}\text{Ba}^+$ has a microwave splitting; optical transitions for cooling and detection [25]; and emits photons that are entangled to the qubit which have been converted to wavelengths favorable for transmission through optical fibers [26]. In this work, the qubit we use is the hyperfine-split ground states of $^{171}\text{Yb}^+$. We define $|0\rangle$ as $|F=0, m_F=0\rangle$ and $|1\rangle$ as $|F=1, m_F=0\rangle$ in the $^2S_{1/2}$ manifold. A qubit can be expressed in the lab frame as:

$$|\psi\rangle = \cos(\theta/2) |0\rangle + \sin(\theta/2)e^{i(\omega_{hf}+\delta)t} |1\rangle \quad (2.1)$$

where $\omega_{hf} = 2\pi \times 12.6428$ GHz and $\delta = 2\pi 310.8 B^2$; B is in units of Gauss and δ is in units of Hertz. These frequencies define the resonance condition of the qubit. The dependence on the magnetic field is quadratic and the shift can be very small, which means that the qubit resonance is incredibly stable and can be driven coherently by electromagnetic fields of a similar frequency. In contrast, if the frequency of a qubit splitting is too noisy, the electromagnetic drive will dephase from the qubit. In this regard, the $^{171}\text{Yb}^+$ qubit has a naturally long coherence time of ~ 1 second [18]. Using spin-echo pulses, researchers have been able to extend this coherence time to ~ 10 minutes [27]. This is comparable to true “atomic clock” transitions that are insensitive to magnetic field fluctuations [28], despite having a weak dependence on magnetic field. Since our experiments are typically only a few milliseconds long, the coherence time of the qubit does not limit us.

Furthermore, the radiative decay lifetime of $|1\rangle$ to $|0\rangle$ is ~ 16 minutes, effectively zero for the experimental timescales we consider [29]. For this reason, a qubit prepared in any arbitrary state will remain in that state as long as no light is applied to it.

2.2 rf Paul Traps in Theory

Trapping ions using electromagnetic fields dates back to the mid 21th century. Hans Dehmelt and Wolfgang Paul shared a Nobel prize for their work on two types of ion traps [30, 31]. Hans Dehmelt is accredited with developing the Penning trap, which uses static electric and magnetic fields to trap charged particles. These devices

have been used to make world-class instruments for precision measurements [32–34] as well as quantum simulators [35, 36]. Wolfgang Paul, on the other hand, worked on traps which use static and oscillating electric fields to trap ions. These Paul traps will be a focus of this chapter and form a bedrock of the research presented in this thesis. We can begin our discussion of Paul traps by considering confining charged particles in Cartesian coordinates:

$$V(x, y, z) = \frac{V_0}{2r_0^2}(\alpha x^2 + \beta y^2 + \gamma z^2) \quad (2.2)$$

where r_0 is the distance of the particle from central trapping region and α , β , and γ are coefficients of the quadratic potentials. Applying Gauss' Law, we arrive at the under-constraining equality:

$$\nabla^2 V(\vec{r}) = \alpha + \beta + \gamma = 0 \quad (2.3)$$

In a single dimension, it is simple enough to set α to 0 and $\beta = -1 = -\gamma$:

$$V(x, y, z) = \frac{V_0}{2r_0^2}(\beta y^2 - \gamma z^2) \quad (2.4)$$

and

$$E_x = 0, E_y = -\frac{V_0}{r_0^2}y, E_z = \frac{V_0}{r_0^2}z, \quad (2.5)$$

Due to the symmetries of the trapping fields, a charged particle injected into the trap will experience a saddle potential, which only confines in one direction.

Instead, rf Paul traps work by time-varying β and γ together as $\beta(t) = -\gamma(t) = \cos(\Omega_{rf}t)$, causing the signs of E_y and E_z to oscillate around 0 periodically. These fields can be thought of as a rotating saddle pseudo-potential, causing the particle to experience a harmonic potential.

Now, we can introduce a static component alongside the oscillating potential of the form:

$$V(x, y, z) = \frac{V_{dc}}{2} + \frac{V_{rf}(y^2 - z^2)}{2r_0^2} \cos(\Omega_{rf}t) \quad (2.6)$$

Where Ω_{rf} is the rf oscillation frequency supplied to the electrodes and V_{rf} is the voltage of that rf signal. Inside this potential, a charged particle will move according to the following differential equations:

$$\ddot{y} + \frac{e}{mr_0^2}(V_{dc} + V_{rf}\cos(\Omega_{rf}t))y = 0 \quad (2.7)$$

$$\ddot{z} + \frac{e}{mr_0^2}(V_{dc} + V_{rf}\cos(\Omega_{rf}t))z = 0 \quad (2.8)$$

Here, e is the electron charge and m is the mass of the charged particle. This set of equations takes the form of Mathieu differential equations which are solved using the Floquet theorem. See ref. [37] for a thorough derivation of the particle's equations of motion. The results can be summed up:

$$y(t) \approx Y_0 \cos(\omega_y t) \left(1 + \frac{eV_{rf}}{mr_0^2 \Omega_{rf}^2} \cos(\Omega_{rf}t)\right) \quad (2.9)$$

$$z(t) \approx Z_0 \cos(\omega_z t) \left(1 + \frac{eV_{rf}}{mr_0^2 \Omega_{rf}^2} \cos(\Omega_{rf}t)\right) \quad (2.10)$$

Where Y_0 and Z_0 are the amplitudes of the ion's slowly oscillating secular motion, and ω_y and ω_z are the radial secular frequencies. Additionally, we can see another term which is typically an order of magnitude smaller than the trapping potentials that oscillates at the rf drive frequency. This term crucially depends on the distance of the particle from the null of the potential. If $\frac{Z_0 e V_{rf}}{m r_0^2 \Omega_{rf}^2} \ll 1$, $\frac{Y_0 e V_{rf}}{m r_0^2 \Omega_{rf}^2} \ll 1$, then the equations of motion in **Equation 2.9** are dominated by the terms oscillating at the secular frequencies. Outside of this region, the particle will experience small excursions from its nominal position, known as micromotion. It is useful to think of a rotating saddle potential to imagine micromotion [31]. The particle, no longer at the center of the saddle, will be repeatably perturbed by the potential barrier. Although this dislocation is highly coherent and can be considered a feature of an ion trap, it can also heat ions, causing them to be ejected from the trap, or alter the laser-atom interactions we use to manipulate the ions. Therefore, minimizing micromotion is often a crucial step in setting up an ion trap experiment [38]. By changing the static confinement, the ions can be moved into the region of the trap where micromotion is minimized.

Typically, the static axial confining term is quadratic, though it can also include a quartic term. Such confinement would feature an electric potential of the form:

$$V(x, y, z) = \frac{V_0}{2} + \frac{V_{rf}(y^2 - z^2)}{2r_0^2} \cos(\Omega_{rf}t) + \alpha_0^2 x + \frac{1}{3} \alpha_1 x^3 \quad (2.11)$$

With a purely quadratic term in the Hamiltonian, the axial confinement is harmonic, which causes the ions to bunch together in the middle of the trap and the

ion positions can be solved for numerically [39]. The additional anharmonic term allows for more evenly-spaced ions, and also has numerical approaches for solving for ion position [40].

2.2.1 Ultra-High Vacuum Systems

Aside from being trapped by appropriate trapping potentials, ions need to be isolated from the outside world using ultra-high vacuum chambers with pressures of 10^{-11} Torr. These vacuum chambers are built with fused silica windows, allowing physicists to either shine laser beams onto the ions and change their internal states or collect photons that they emit.

Though the ions are insulated from interacting with matter outside their chamber, there are still collisions between trapped ions and background gases inside the chamber. Stainless steel is generally the material of choice for making ultra-high vacuum systems, which is infused with H_2 molecules during production [41, 42]. These molecules diffuse out of the steel over time and into the vacuum chamber. Methods to rid the steel of H_2 are being researched, including baking the systems at high temperatures and treating their surfaces [43]. Nevertheless, in ours and many other experimental systems, H_2 remains the dominant background gas after other gases have been thoroughly removed. It can collide with a trapped ion and create hydride molecules, induce significant heating and melt the ionic crystal, or simply make a glancing collision and require more laser cooling before the experiment returns to a useful state. Since the likelihood of background collisions scales

linearly with ion number, current systems of < 100 qubits will not be limited by their collision rates [30].

2.3 Trapping Ions in Practice

To create the above-mentioned trapping potentials, we use segmented, gold-covered alumina blades [11], as depicted in **Figure 2.1**. The dc electrodes, labeled E1-E5, carry a static potential between -10 and 10 V. The rf electrodes have a structure that mirrors the dc electrodes but the entire electrode carries the same potential. The two sets of electrodes are matched by another set of dc and rf electrodes such that we have access to 10 individual dc electrodes and 2 connected rf electrodes. The four electrodes are positioned to create a $450\mu\text{m}$ by $325\mu\text{m}$ rectangle, as shown in **Figure 2.2**. These sets of electrodes combine to create the quadrupole trapping potential that is described by **Equation 2.11**. The rf potentials are driven by a signal oscillating at $2\pi \times 23.83$ MHz, which cause the ions to experience a secular frequency of $2\pi \times 3.05$ MHz. Based on **Equation 2.9**, we can infer that the peak voltage on the rf drive is ~ 400 V.

The trap is held inside a stainless steel vacuum chamber with high optical access. A helical quarter-wave rf resonator ([44, 45]) and several digital to analog voltage converters are connected to the trap using rf feedthroughs. The resonator is used to deliver a high-voltage rf field to the trap with a narrowly defined frequency. As we will see later, the stability of this field has great implications for our ion trap quantum computer. No substantive changes have been made to the trap or anything

inside the vacuum chamber since Ref. [11] was published.

In an ideal scenario, electrodes would be configured to affect a somewhat flat-bottomed axial potential at the center of the trap where the micromotion null is found. This flat-bottomed potential takes the form of a quartic term in the axial potential ($\alpha_1 \gg \alpha_0$ from **Equation 2.11**). In practice, we found that the micromotion null of the trap was actually over electrodes E2 and E9, likely due to imperfections of the trap assembly. We chose to ground electrodes E4, E5, E6, and E7 and only use electrodes E1, E2, E3, E8, E9, and E10 for trapping. This significantly impeded our ability to create the flat-bottomed potential [46], so it is quadratic instead. Without a quartic potential, we cannot create equally spaced ions that are well-imaged onto the equally spaced optical elements that will be described later on in **Chapter 3**.

2.4 Loading the Ion Trap with Ytterbium Ions

To trap $^{171}\text{Yb}^+$ ions, we use a two-photon process that allows for isotope selectivity [47]. We start with ~ 25 mg of isotopically enriched neutral ^{171}Yb stored in a stainless steel tube pointed towards the ion trap [11]. 95% of the Yb in this sample is ^{171}Yb and 5% is ^{174}Yb . Then we use a dc current to heat the tube, which propels neutral Yb atoms through the ion trap. We then focus 398.8 nm laser light resonant with the $^1S_0 \rightarrow ^1P_1$ transition of neutral ^{171}Yb perpendicular to the atomic beam, which decreases the broadening of the transition due to Doppler shifts. The equivalent transition in ^{174}Yb is more than a GHz detuned, creating isotopic selec-

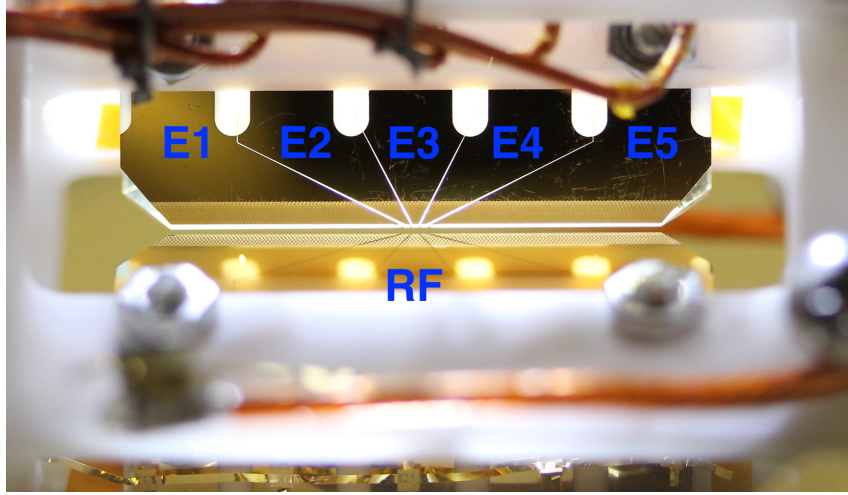


Figure 2.1: Photograph taken of the ion trap. The dc electrodes are in focus and back-lit to emphasize their segmented nature. The white that surrounds the golden electrodes is Macor ceramic. 5 dc electrodes and an rf electrode are labeled.

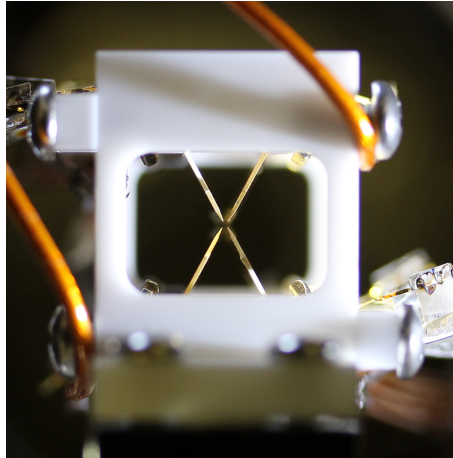


Figure 2.2: A photograph looking down the axis of the trap. From here, it is clear that the edges of the razor blades make a rectangular shape. The sharpness of the blades and the clean deposition of gold onto them are necessary for generating smooth trapping potentials.

tivity of ^{171}Yb [47]. Other isotopes present in the neutral Yb sample are similarly off-resonant, though are less likely to be present. Then we use one of two lasers with a wavelength less than 394.1 nm to further excite the electron from the 1P_1 level into a continuum of states excited beyond the atom, thereby creating $^{171}\text{Yb}^+$ ions. In our experiment, we have excess cooling and Raman light that we can use for this second transition. The atoms are ionized inside the rf trap, where they are repelled from one another and the rotating potential barriers. Without a means to dissipate the significant kinetic energy of the ions, the ions will not be well-confined and will eventually leave the trap. Therefore, we need a method for cooling our ions on command.

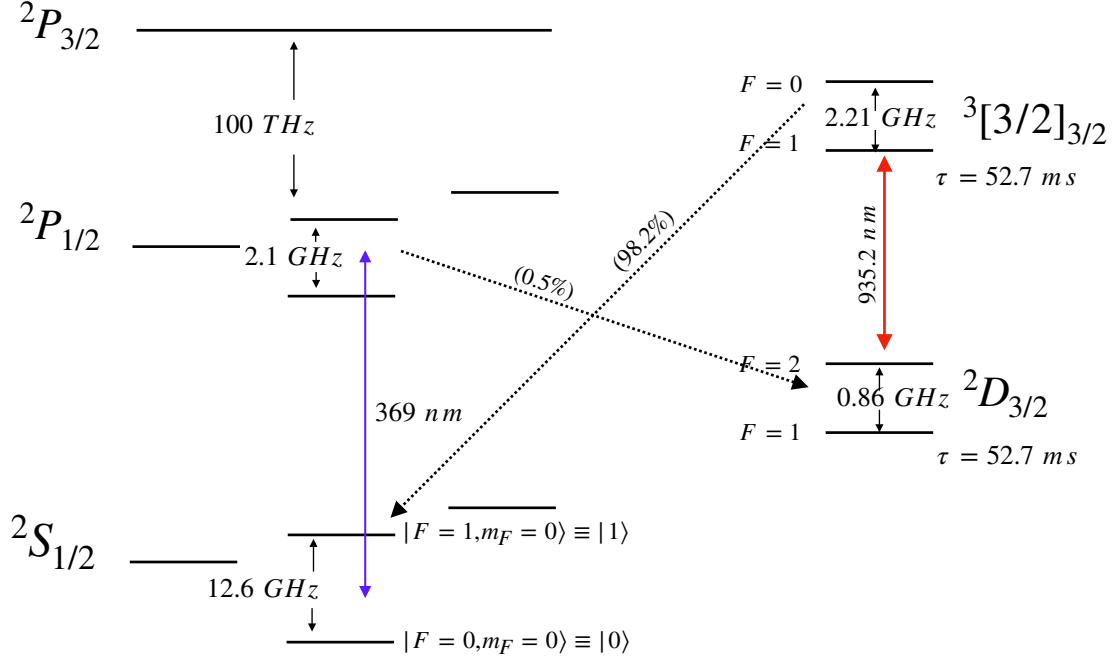


Figure 2.3: Diagram of the most relevant $^{171}\text{Yb}^+$ energy levels for the purposes of this thesis. The qubit is defined in the hyperfine-split $^2S_{1/2}$ manifold. The $^2S_{1/2}$ to $^2P_{1/2}$ transition is used for cooling, initialization, and detection, but the $^2P_{1/2}$ states have a small likelihood of decaying to the $^2D_{3/2}$ manifold. To get the ion back into the $^2S_{1/2}$ or $^2P_{1/2}$ manifolds, another laser is used that transfer the ion to the $^3[3/2]_{3/2}$ manifold, which quickly decays to the $^2S_{1/2}$ manifold.

2.5 Ytterbium Energy Levels

Now we will discuss the energy levels of Ytterbium beyond the qubit levels. Most notably, we couple the qubit to the $^2P_{1/2}$ manifold using a UV transition, see **Figure 2.3**. We will leverage this S-P coupling for several important processes: cooling ions to load them into the trap and between experiments; initializing them into the $|0\rangle$ state; and detecting them using a state-dependent fluorescence technique. The $^2P_{1/2}$ can decay with 0.5% likelihood outside of our qubit states and into the long-lived $^2D_{3/2}$ manifold. The D-state lifetime is 52.7 ms. We can couple the D-manifold levels to the $^3[3/2]_{3/2}$ manifold using a 935.2 nm laser, see **Figure 2.3**. Since both these energy levels have hyperfine structure, we need to couple both the $|F = 1\rangle$ and $|F = 2\rangle$ states of the $^2D_{3/2}$ manifold to the respective $|F = 0\rangle$ and $|F = 1\rangle$ states of the $^3[3/2]_{3/2}$ manifold. We accomplish this by adding a 3.07 GHz sideband onto the light using an electro-optic modulator (EOM). The bracket states finally decay into the ground state manifold. Without this laser, the ion would quickly get stuck in the D states when 369 light is applied to the ions.

2.5.1 Doppler Cooling

The atoms are ionized inside the trapping zone after being propelled from the atomic ovens with very large velocities. We dissipate this unwanted kinetic energy using Doppler cooling laser beams off-resonant from the S to P transition [48, 49], depicted in **Figure 2.4c**. A laser beam's ability to cool atoms is related to the amount of photons it can scatter off the ion, where scattering events remove some

momentum from the ion on average. Scattering rates are given by [29]:

$$\Gamma_{sc} = \frac{\frac{I}{I_{sat}} \frac{\Gamma}{2}}{1 + \frac{I}{I_{sat}} + \left(\frac{2\Delta_L}{\Gamma}\right)^2} \quad (2.12)$$

Where I is the beam intensity and $I_{sat} = \pi\hbar c/3\lambda^3\tau$ is the transition's saturation intensity, $\tau = 2\pi \times 19.6\text{MHz}$ is the natural linewidth of the S to P transition [18]. Γ is the spontaneous emission rate equivalent to $2\pi/\tau$. The laser detuning is Δ_L , therefore a larger detuning will simply lead to less photons being scattered. The fast-moving ions will experience a Doppler shift from resonance as $\Delta_L = \delta - \vec{k} \cdot \vec{v}$. Since we expect atoms to be very hot upon arrival in the trap, we apply two laser beams to cool them. One is a 300 MHz detuned beam that cools some subset of hot ions, and the other is a 9.8 MHz detuned beam for the ions once they are less energetic. The intensity of the 200 MHz detuned beam is far beyond I_{sat} , which power-broadens the transition and scatters considerable numbers of photons off $^{171}\text{Yb}^+$ ions moving at a wide range of velocities. This beam is also used to cool ions once trapped, as it can cool ions after significant collisions with background gases.

The detuning of the 9.8 MHz beam is decided by the the fact that the Lorentzian structure of the atomic transition has the steepest slope at its full-width half-maximum. Therefore, we can cool most efficiently by setting the frequency of our laser at $\delta = -\tau/2$ MHz away from resonance. This beam is below the saturation intensity, which cools the ions to a temperature defined by the recoil limit. We use an additional, attenuated beam before experiments to lower the recoil limit of our cooling beams.

We Doppler cool our ions by coupling every state in the $^2S_{1/2}$ manifold with states in the $^2P_{1/2}$ manifold. This is accomplished using all polarizations, $\hat{\pi}$, $\hat{\sigma}^+$, and $\hat{\sigma}^-$, see **Figure 2.4c**. We couple the $F = 0(1)$ states in the S manifold to the $F = 1(0)$ states in the P manifold using a resonant beam with a 14.7 GHz sideband. This is done by sending in a resonant beam through an EOM driven by a 7.3 GHz signal. By driving the EOM strongly, we can generate a large second-order sideband at the necessary detuning of 14.7 GHz. This way, we can efficiently cool the ion as it stays between the S and P manifolds, a condition met by using the 935.2 nm beam.

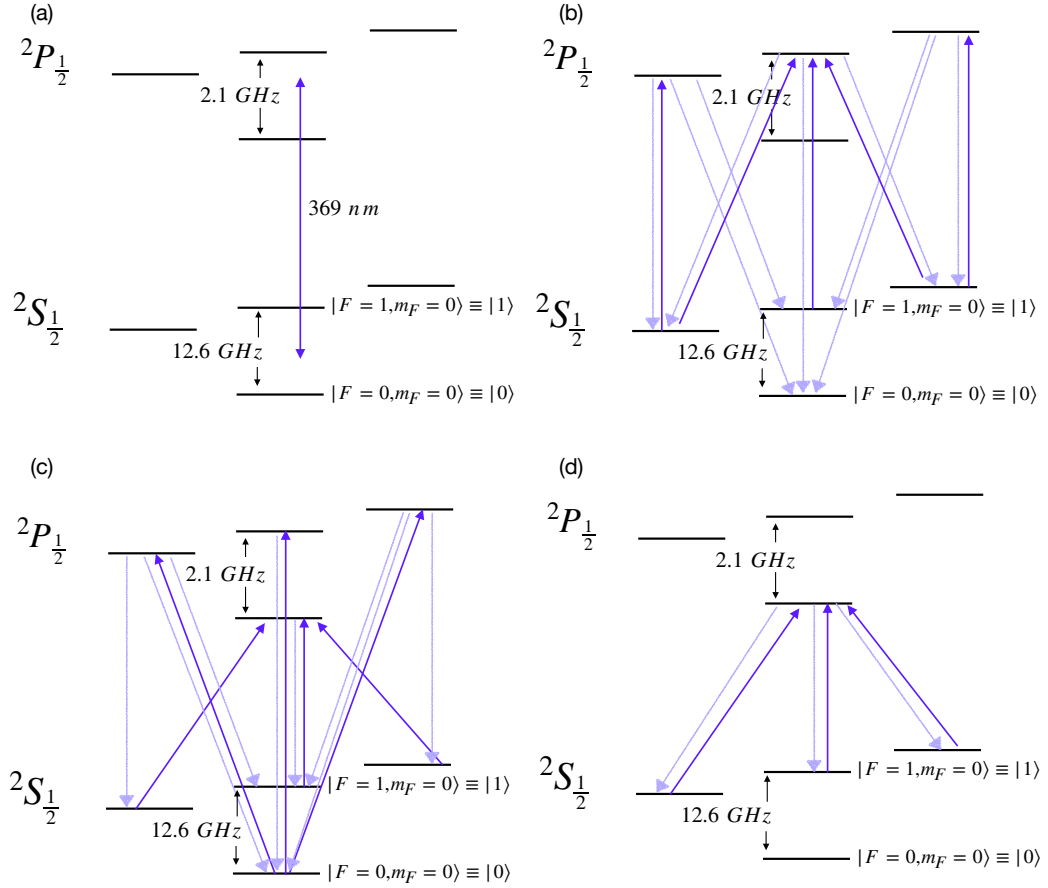


Figure 2.4: The S-P transition is used for initialization (b), cooling (c), and detection (d). For each utility, a different set of sidebands is put onto the beam and different polarizations are required. The only function that is significantly worsened by off-resonant processes is detection, where the beam resonantly drives a cycling transition between the states shown and photons are collected. The beam can off-resonantly excite the ion into the $2P_{1/2}$ $F=1$ manifold, which will decay to the $|0\rangle$ qubit state and no more photons will be scattered. All three individual beams are focused with a slight angle to the axis of the ion chain. By doing so, all polarizations are available. Cooling could be improved by changing its direction to address the radial motion more strongly.

2.5.2 Initialize

Initializing qubits at the beginning of every experiment to a known state is a requirement for quantum computing, as discussed above. Certainly, it would be impossible to compute with a qubit in some unknown state. Therefore, we optically pump our qubits into $|0\rangle$ at the beginning of every experiment. We apply a beam that is resonant with the transition between the $F = 1$ states in the S manifold and the $F = 1$ states in the P manifold with all polarizations, as seen in **Figure 2.4b**. We create this resonance condition using a 2.1 GHz sideband applied to a resonant 369 nm beam using an EOM. The $F = 1$ levels of the P manifold will either decay to $|0\rangle$ or back to the $F = 1$ levels of the S manifold. This process will continue until no population is left in any state besides $|0\rangle$, where they will be 12.6 GHz detuned from resonance with the applied light. In practise, we can transfer $> 99.7\%$ of the population to $|0\rangle$ in only $5 \mu\text{sec}$.

2.5.3 Detection

The detection beam is resonant with the transition between the $F = 1$ states in the S manifold and the $F = 0$ states in the P manifold with all polarizations, as depicted in **Figure 2.4d**. If the qubit is in $|1\rangle$, the beam will resonantly excite it to the P manifold. From there, it will decay down to the $F = 1$ states in the S manifold, while decay to the $F = 0$ state is forbidden. Additionally, any decay to the D manifold will not result in ions ending up in the $F = 0$ state. Therefore, a cycling transition will take place between the $F = 1$ states in the S manifold and

the $F = 0$ states in the P manifold. Since the Zeeman splitting is only 7 MHz, any of the $F = 1$ states are still near-resonant, and many photons will be emitted from the qubit in every direction.

In contrast to the fluorescence emitted from ions in $|1\rangle$, ions in $|0\rangle$ are 14.7 GHz off-resonant from allowed transitions. Therefore, they will scatter very few photons in the presence of the detection beam, as seen in **Figure 2.5**. Therefore, the fluorescence is dependent on the detected state and we can use a discriminator method to determine the qubit state, if we collect two or more photons, we infer that the qubit was in $|1\rangle$ and vice versa.

In practise, we shine this resonant light onto the ions for $150\mu\text{s}$, and we collect 9 photons on average to form a Poisson-like distribution, as seen in **Figure 2.5**. The intensity of the detection beam is locked with a PID loop to preserve this same distribution for all experiments.

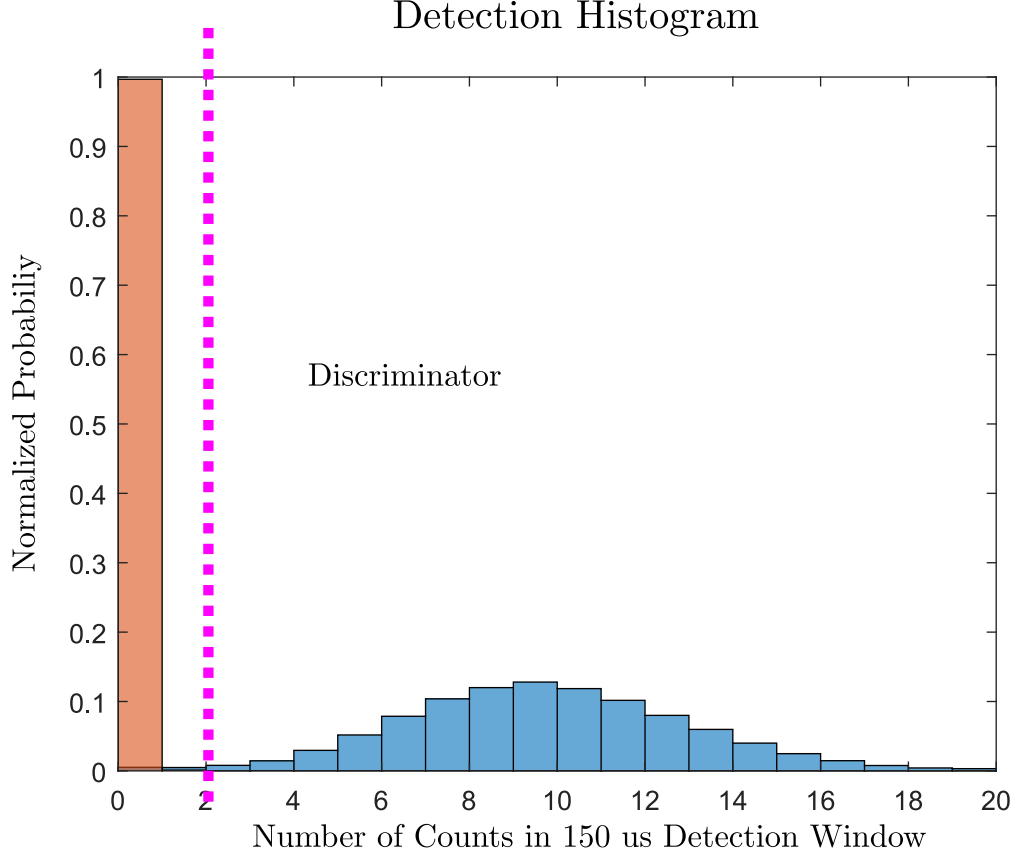


Figure 2.5: Real data from measuring a qubit prepared in $|0\rangle$ by means of optical pumping or in $|1\rangle$ using pumping as well as a high-fidelity microwave transition. The bright state scatters an average of 9 photons every experimental cycle, while the dark state scatters none. Our preferred method of determining which qubit state the ion was in is a discriminator method, where two or more counts are enough to label the ion as bright. The detection fidelity of $|0(1)\rangle$ is 99.66(3)%(99.04(5)), where the uncertainties are statistical.

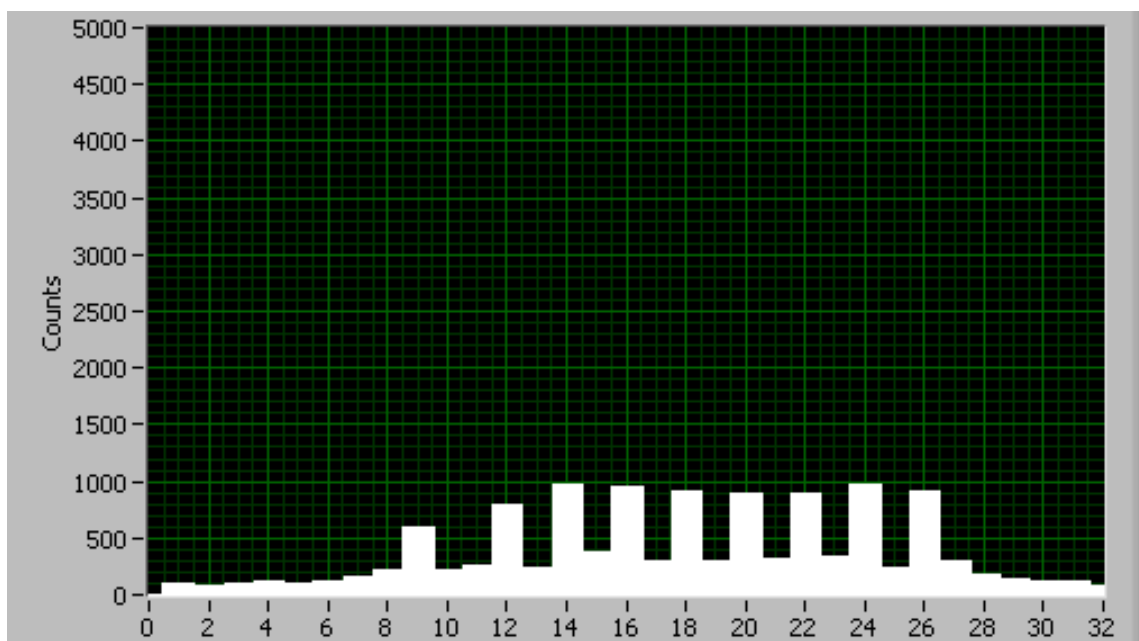


Figure 2.6: All 32 channels of our 32-channel PMT array are slowly read out onto a display like this. This allows for the close monitoring of the qubit fluorescence between experiments.

2.5.4 Experimental Setup for Detection

We ultimately detect our qubits by collecting photons with a 0.37 NA lens and imaging them onto an intermediate imaging plane where spatial filters block out background scatter [11]. Next, we magnify the intermediate image plane using a telescope that focuses the image onto the individual channels of a 32-channel PMT array¹ [11]. The PMT's have a quantum efficiency of $\sim 40\%$ for the 369 photons we expect to scatter. The PMT array outputs small signals of only ~ 10 mV and ~ 1 ns rise time across a 50 Ohm load. These signals are sent into a digitizing FPGA that simply converts them into 40 ns digital pulses, which are sent to a second FPGA that does the actual counting. The main source of error in this PMT array is the electrical crosstalk. $\sim 3\%$ of all counts cause a neighboring channel to register a photon count and $\sim 0.5\%$ is registered on next-to-nearest neighboring channels. In order to reduce the crosstalk, every other channel is used for imaging our ions.

Since Ref. [11] was published, we added an optional time-stamping feature to the FPGA. With the time-stamping, the number of photons are recorded alongside their arrival time to the nearest half microsecond. Since the photons are coming asynchronously with the FPGA clock, we need to stretch them in time at least as long as three times the clock time for them to be counted *and* time-stamped. If they are too short, the positive edge of the FPGA's clock might not coincide with the counter and the time stamping will never register. Another failure mode is if the photon arriving simultaneously with the positive edge, which can put the

¹Hamamatsu H7260-200

FPGA state machine into an unstable state that takes several clock edges to resolve. Therefore, we extend the pulses to be 3x the clock cycle of the FPGA. The time stamping is finally performed by initializing a counter on the FPGA at the beginning of the detection chapter. If a photon is counted, the position of that counter is converted to μs and recorded.

With or without time-stamping, the digitizing FPGA receives information about which channels to bin together and send to the counting FPGA. As of now, only 8 lines of data are capable of being sent to the counting FPGA, but any combination of the 32 channels can be sent over those communication lines. Simultaneously, the digitizing FPGA updates a LabView program of the counts in each of the 32 channels over a USB line about once every second. The LabView program then displays the counts, so the ions can be monitored regularly. A sample display is shown in **Figure 2.6**. By visual inspection of the counts, experimentalists can deduce if lasers are locked or if the PMT's are misaligned.

Within this detection scheme, there are a few unrelated, outstanding issues that can limit our measurement fidelities. Firstly, the $150\ \mu\text{s}$ detection window that we require to collect 9 photons is long enough for non-resonant processes to begin lowering our detection fidelity. In that time, the 2.1 GHz detuning of the detection beam is capable of exciting the ion into the $F = 1$ states in the P manifold. This has a significant probability of decaying into $|0\rangle$, and the ion will no longer scatter photons. We term this dynamics bright-to-dark pumping because the bright state, $|1\rangle$, is off-resonantly pumped into the dark state, $|0\rangle$. If this happens before 2 photons are counted, then we incorrectly infer that the ion was in $|0\rangle$. This is

the main source of error that asymmetrically drives down the detection fidelity. Detecting $|0\rangle$ is done at higher fidelity because the relevant transition is a further 12.6 GHz detuned, though dark-to-bright pumping is also a source of error. Because of these issues, we detect $|0\rangle$ with 99.66(3)% fidelity and $|1\rangle$ with 99.04(5)% fidelity, as can be seen in **Figure 2.7a-b**.

Another asymmetry that effects our detection fidelities is the electrical crosstalk. As seen in **Figure 2.7b**, the counts from a bright ion in channel 2 have spilt over onto channels 1 and 3. These crosstalk counts effect channel 3 more than twice as often as channel 1. While the spillover of counts is 0.5%, the bright-state detection is much lower at 0.008%. This portrays the strength of the discrimination method we employ. While many false counts are being registered, they are completely uncorrelated. Therefore, the likelihood of two of these random crosstalk errors occurring in the same 150 μ s window is very low. If two ions are prepared bright on either side of a dark ion, both ions will spillover onto the dark ion’s channel causing the dark ion to be erroneously read as bright 0.0171(6)%, a marked uptick from when only one neighboring ion is bright. Of course, this is caused by the increased likelihood of two crosstalk errors to occur in the same detection window, see **Figure 2.7c**.

With these errors well-documented, we can understand the data in **Figure 2.7d**, where each of the detection fidelities of each of the $2^5 = 32$ 5-qubit states are presented with an average readout fidelity of 95.6%. The data is taken by moving a single ion to different parts of the trap where its fluorescence will be imaged onto each of the 5 relevant PMT channels. We prepare it in both the dark state with optical pumping or the bright state with high-fidelity microwave Rabi flopping.

Once we have statistics for each PMT channel, we assume that all the detection errors are uncorrelated and we simply add counts together to create the photon statistics of each state. The state $|00000\rangle$, for example, is generated by adding the data from preparing dark ions in each of the 5 PMT channels. This state happens to be the highest fidelity state we can measure because the biggest issues in our detection scheme, bright-to-dark pumping and electrical crosstalk, are minimized. The lowest fidelity states are $|10101\rangle$, where crosstalk is maximized, and $|11011\rangle$, where a combination of crosstalk and bright-to-dark pumping lower the fidelities. The bright-to-dark pumping issues are shown in **Figure 2.7e**, where we show a 3D state-to-state histogram. Clearly, there is significant structure in this plot as each state, n , is likely to be misread as $n \pm 2^m$, where m is 1-5. This accounts for the diagonal structure seen in the figure.

Also, we can see how all $2^7 = 128$ 7-qubit states are measured with 92.6% fidelity in **Figure 2.8**. Again, we see the highest fidelity state is $|0000000\rangle$ and the lowest fidelity states have many bright ions and dark ions with two bright neighbors like $|1010101\rangle$ and $|1101010\rangle$.

We can correct for these errors for averaged data by generating statistics for a state-to-state error matrix that maps the likelihood of incorrectly measuring a particular state, i , if another state, j , is actually prepared. We can measure these errors, and present them as ϵ_j^i into a 2^N square matrix that accounts for all the state preparation and detection (SPAM) errors within the system. Since these errors are naturally convoluted together and they only occur once per experiment, we combine

them. Here is an example for 7 qubits:

$$M = \begin{bmatrix} 1 - \epsilon_{0000000}^{0000000} & \epsilon_{0000001}^{0000000} & \cdots & \epsilon_{1111111}^{0000000} \\ \epsilon_{000000}^{0000001} & 1 - \epsilon_{0000001}^{0000001} & \cdots & \epsilon_{0000001}^{1111111} \\ \vdots & & \ddots & \\ \epsilon_{0000000}^{1111111} \cdots & & & 1 - \epsilon_{1111111}^{1111111} \end{bmatrix} \quad (2.13)$$

This matrix maps a vector detected states onto a vector of SPAM-free states as follows:

$$\vec{P}_{det} = \mathbf{M} \vec{P}_{ideal} \quad (2.14)$$

Therefore, we can correct for SPAM errors using the following protocol. First we repeat any experiment several thousand times like many other quantum physics experiments where single-shot measurements cannot accurately capture the quantum state due to noise or quantum superposition. Next, we record the likelihood of measuring each possible state in the qubit register and represent those statistics in a vector, \vec{P}_{det} . Lastly, we use the SPAM matrices and matrix inversion such that we extract $\vec{P}_{ideal} = \mathbf{M}' \vec{P}_{det}$.

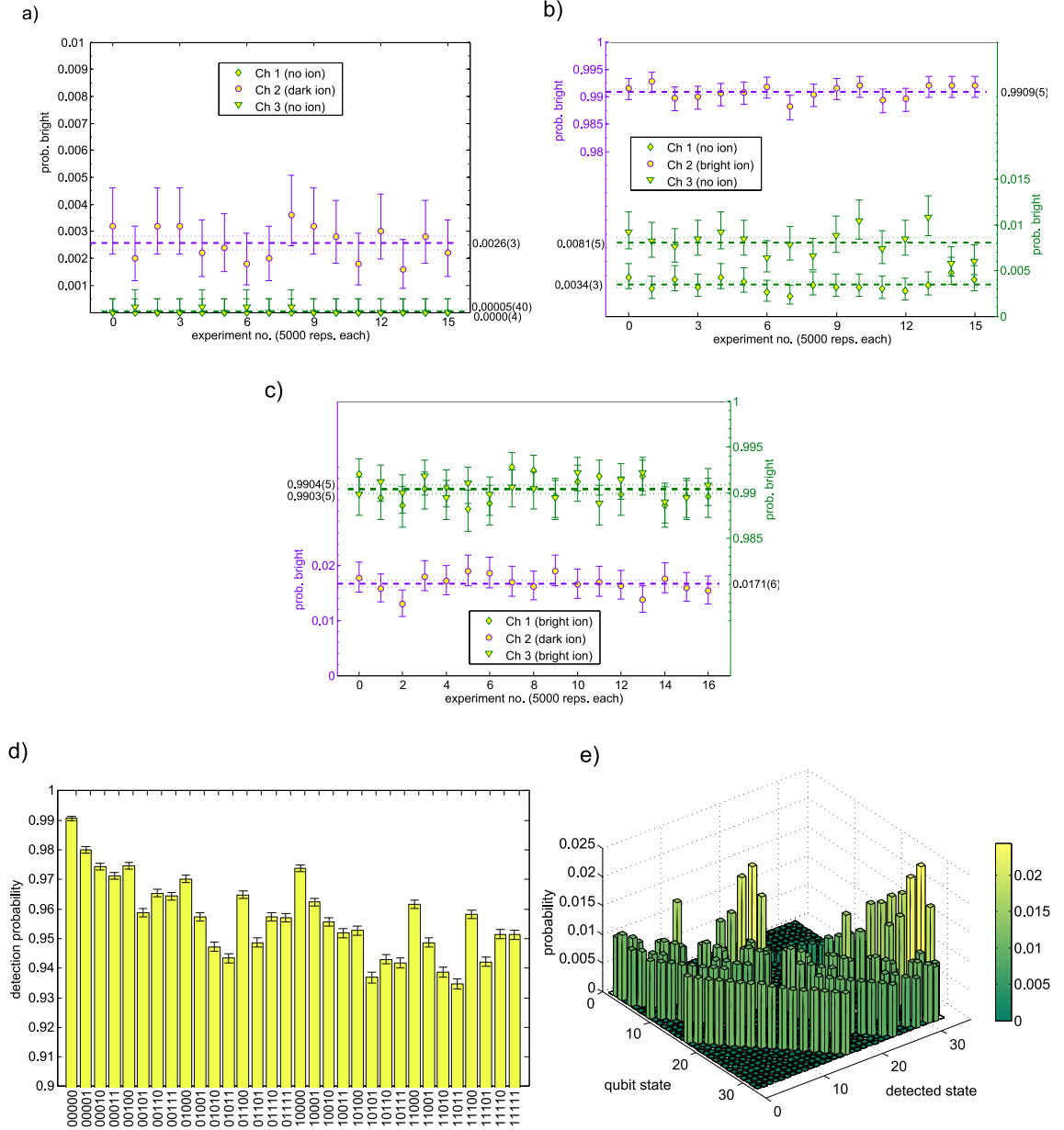


Figure 2.7: Different experiments were performed to learn properties of our measurement apparatus. All error bars are statistical. a) A single ion is prepared dark and imaged onto PMT channel 2. The likelihood of measuring any counts is very low, 0.0026(3)%. b) A single ion is prepared bright and imaged onto channel 2. Channel 3 has double the crosstalk counts as channel 1, which is due to electrical crosstalk in the PMT and not optical spillover. c) Two bright ions are imaged onto channels 1 and 3, and a dark ion is imaged onto channel 2. The detection crosstalk is worse than the sum of its parts because the bright-state detection threshold is 2 photons. d) Fidelity of measuring each three-qubit state. e) The state-to-state error matrix of preparing each state and measuring others.

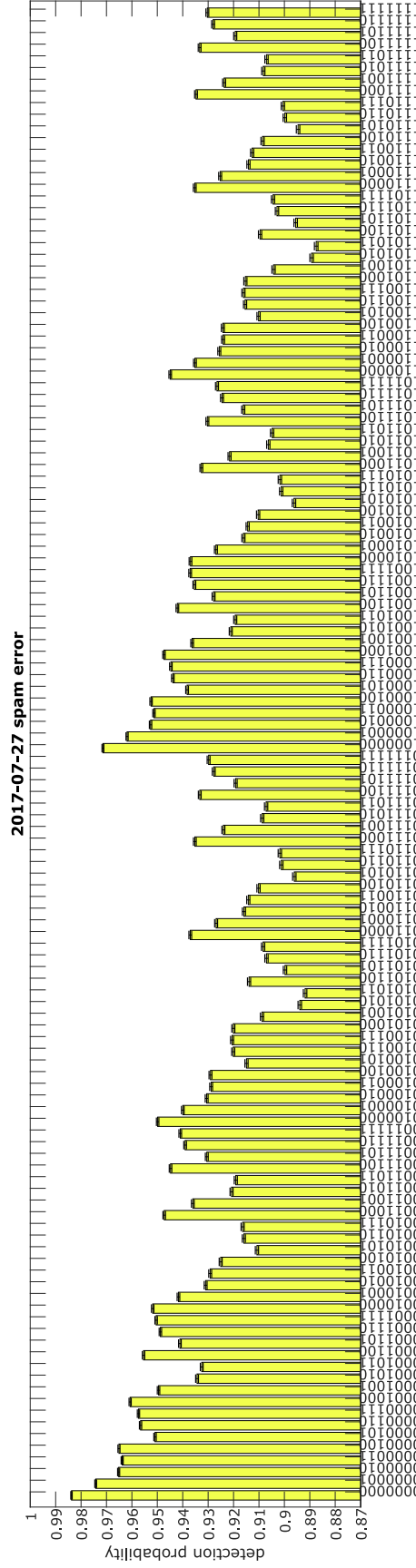


Figure 2.8: The fidelity of all 128 7-qubit states are presented. The worse states have either alternating bright and dark states. For 5-qubit states, the fidelity of measuring each qubit is nearly identical. For 7-qubit states, the fidelity of measuring qubit 1 is worse than the other 6. This is due to imperfect alignment of that ion onto the PMT array.

2.5.5 Other Methods for State Classification

As presented in Ref. [50], we explored other methods for classifying many-qubit states beyond a simple discriminator based on neural networks. A neural network can be considered a collection of neurons organized in layers. The input layer is comprised of photon counts from the PMT array and their arrival times, while the output layer is the many-qubit state classification. Both of these layers have a defined number of neurons pending on the number of PMT channels and the number of qubits. Between these layers are so-called hidden layers, whose neuron count can be larger than that of the input and output layers.

The input vector to each layer, \mathbf{x}^i , is defined by the output of the previous layer, \mathbf{z}^{i-1} . Each layer has its own weights and biases, represented as vectors \mathbf{b}^i and matrices \mathbf{M}^i respectively. Each neuron then performs the algebra $\mathbf{z}^i = \mathbf{M}^i \mathbf{x}^i - \mathbf{b}^i$ to create a convoluted mapping between the input layer and the output layer. By training the NN on large numbers of real data, the optimal values of \mathbf{M}^i and \mathbf{b}^i can be learned and a direct mapping between photon counts and arrival times to qubit state can be generated.

In our implementation of this NN, we found that two hidden layers worked the best, while the optimal number of neurons in these layers varied between 8 and 40 pending on the complexity of the input data. As mentioned above, ions are imaged onto every other channel of the PMT array. Therefore, NN's were tested with and without the data from these intermediate PMT channel. Similarly, NN's were tested with and without the photon arrival time data. Pending on what data was used,

the optimal number of neurons changed. More details about the training formalism are included in the manuscript [50].

To train the NN for a given configuration of ions or PMT channels, we used 60% of the collected data. Then 20% of the data was used to validate the NN and another 20% was used for testing. After training and validation, a NN can take the photon counts from a single experiment and report the qubit state.

A NN trained with both time-stamping information and photon counts from intermediate channels demonstrated an improvement over the simple discriminator method we had been using until then. To increase the competitiveness of the non-learned method, we implemented an adaptive discriminator method to classify qubit states [21]. This method works by discriminating PMT counts as before, but repeats the process with an adapted threshold based on the state of neighboring qubits. For example, if three PMT channels measured $\{12, 2, 0\}$ counts, then the initial thresholding would deduce the qubits were in state $|110\rangle$ by assuming that any detector with more than one count images a bright ion. Since all of the qubits have neighboring ions that are considered to be, the threshold for a bright event increase to two counts on detectors 1, 2, and 3 and the deduced state changes to $|100\rangle$. This method, called adaptive thresholding, reduces the errors due to measurement crosstalk. Without time-stamped data, the NN was able to match the fidelity of the adaptive threshold classification technique and improve it by 0.1%, as seen in **Figure 2.9**.

More sophisticated methods of thresholding can be developed for classifying qubit states that account for photon arrival times, though this avenue of research

was not implemented for the manuscript [50]. For example, photons that arrived early in the detection window are more likely to be from ions that are prepared in the bright state than to be emitted from ions that were pumped bright. Therefore these early photons can be weighted more heavily than the later photons. The NN was able to leverage this useful information to slightly improve its ability to classify states by 0.1%, as presented in **Figure 2.9** as 'TNN'.

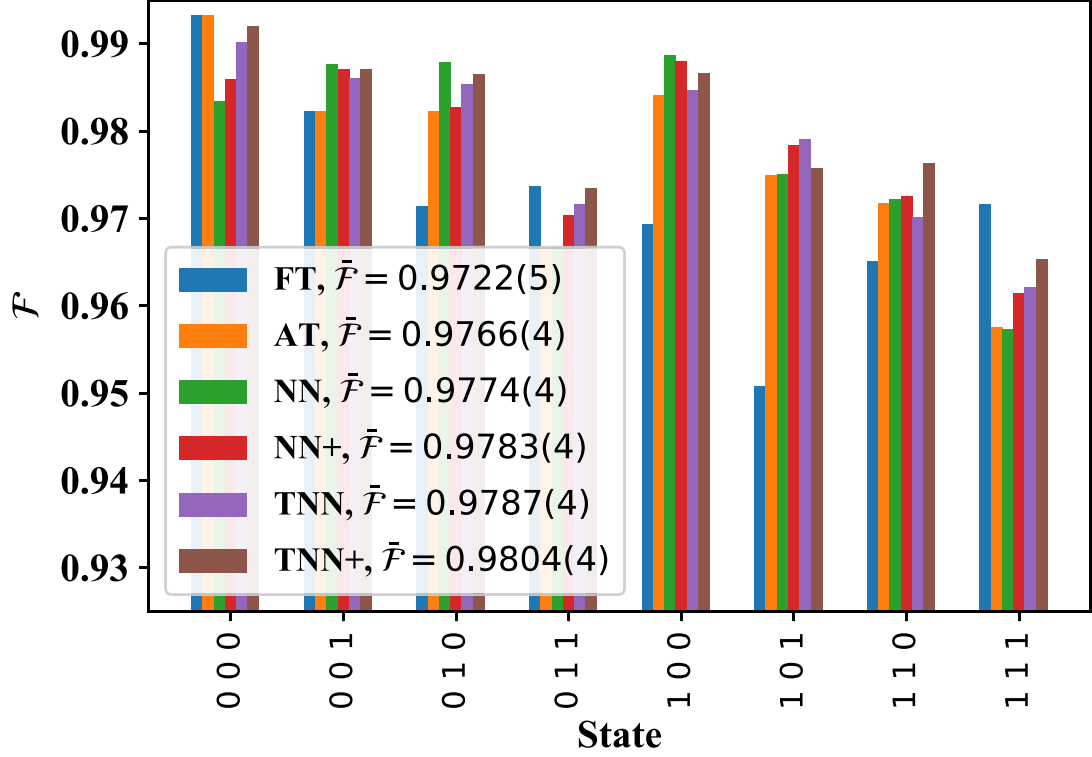


Figure 2.9: Comparing different techniques at classifying 3-qubit states. The fixed threshold (FT) method determines if a qubit is in the bright state if > 1 photon is counted. The adaptive threshold (AT) technique is a recursive method that changes the bright-state threshold of photon counts if neighboring ions are also bright. These approaches are compared with neural networks (NN), which use data from the intermediate PMT channels that do not have ions imaged on them (NN+) or ignore such data (NN). We added time-stamping to the data used for the neural network (TNN/+).

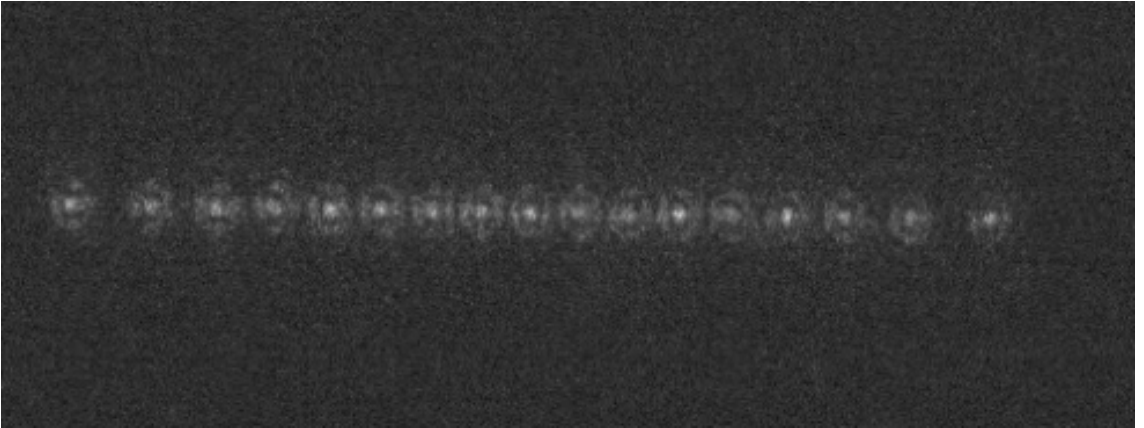


Figure 2.10: Photograph of a 17-ion chain taken on a camera. The spacing between the middle 9 ions is $\sim 2.5\mu\text{m}$.

2.6 Coulomb Crystals

The ions align themselves along the direction of the weaker axial confinement, creating a linear chain. A 17-ion chain is depicted in **Figure 2.10** and 3, 5, 7, and 9-ion crystals were also created for the work in this thesis. Though 2D crystals are possible with both Paul and Penning ion traps [35, 51], the technical requirements for individual detection and individual addressing (see **Chapter 3**) become more daunting. Therefore, proof-of-principle experiments are more amenable to 1D chains. Furthermore, several architectural approaches to ion-trap quantum computers have been proposed using 1D chains [23, 24]. Furthermore, the state-of-the-art ion trap computers currently use a single atomic species [52, 53], which simplifies the physical requirements for the experiment and the ion crystal’s motional spectra. With different species co-trapped, multiple atomic ovens need to be present in the vacuum chamber, additional sets of laser frequencies need to be generated and delivered onto the ion chain, and greater control over the trap voltages may need to be available to affect desired ordering of the ions. If the whole chain is of a single species, reordering due to a collision with a background gas molecule will be detrimental because ions are identical. On the other hand, different species or isotopes can create an ordering condition that will require non-trivial swapping of ions in a chain. Still, the benefits of dual-species experiments are notable and machines are being built to move in that direction. Sympathetic laser cooling can be performed on spectator ions with a laser frequency that the qubit ion species is transparent to.

2.6.1 Ion Positions

Here, we discuss how ion positions are calculated from their axial confinement and the inter-ion Coulomb interaction. When confined to a 1D chain with a purely quadratic potential, the potential energy of an N-ion Coulomb crystal is the following [39]:

$$V = \sum_{i=1}^N \frac{1}{2} M \omega^2 x_i(t)^2 + \sum_{\substack{i,j=1 \\ i \neq j}}^N \frac{Z^2 e^2}{8\pi\epsilon_0} \frac{1}{|x_i(t) - x_j(t)|} \quad (2.15)$$

Here, i indicates ion j in the N ion chain. M is the atomic mass of the ion, ω is the trap frequency as defined in **Equation 2.9**, e is the electron charge, Z is the integral amount of charge on the ions, and ϵ_0 is the permittivity of free space. So far, this equation is purely classical. Assuming the ions are well-localized via laser cooling, we can separate the classical positions of the ions from small, quantized displacements from this positions:

$$x_i(t) \sim x_i^{(0)} + \hat{q}_i(t) \quad (2.16)$$

$x_i^{(0)}$ is the equilibrium location of ion i , which we will use to solve for the nominal ion positions. $q_i(t)$ is a time-dependent position operator which we will ignore for now. The equilibrium positions can be found by solving the following equation and can be made dimensionless as $u_i = x_i/\ell$:

$$\left[\frac{\partial V}{\partial x_i} \right]_{x_i=x_i^{(0)}} = 0 \quad (2.17)$$

$$\ell^3 = \left[\frac{Z^2 e^2}{4\pi\epsilon_0 M \omega^2} \right] \quad (2.18)$$

With this, we can write out a set of coupled equations for the values of u_i :

$$\sum_i^N \left(u_i - \sum_{i=1}^{j-1} \frac{1}{(u_i - u_j)^2} + \sum_{i=j+1}^N \frac{2}{(u_i - u_j)^2} \right) = 0 \quad (2.19)$$

The axial confinement in our experiment is a quadratic potential. For more than 3 ions, these sets of equations cannot be solved analytically and require numerical methods to find ion positions, as is done in Ref. [39]. There, positions are calculated for ion numbers 1-10 in a purely quadratic potential, similar to our experimental realization. The spacing between the ions for chains of 5, 7, and 9 ions are depicted in **Table 2.6.1**. There, the distances are normalized by the spacing between the middle three ions.

N		Relative spacing						
5			1.1201	1.00	1.00	1.1201		
7	1.2251	1.0568	1.00	1.00	1.00	1.0568	1.2251	
9	1.3186	1.1178	1.0341	1.00	1.00	1.0339	1.1178	1.3186

Turning our attention to the spacing between the 5 inner ions for each of the 3 configurations, we see that the ratio between the ion distances in red decreases from 12% in 5-ion chains to 3.4% in 9-ion chains. By ignoring the outer ions, the middle 5 ions becomes more equally-spaced by trapping longer chains with a quadratic potential. We take advantage of this fact to improve our alignment of our equally-spaced addressing optics onto the ion chains. Better methods to achieve equal spacing exist, most notably are ion traps with smaller and better-assembled electrodes that can create quartic potentials. Next, we discuss how the Coulomb

interaction generates modes of motion that all the ions participate in.

2.6.2 Phonon Modes

As done in Ref. [39], one can setup a Lagrangian to derive the axial equations of motion of the ion chain:

$$L = \frac{M}{2} \sum_{i=1}^N (\dot{q}_i)^2 - \frac{1}{2} \sum_{i,j=1}^N q_i q_j \left[\frac{\partial^2 V}{\partial x_i \partial x_j} \right]_{q_i=q_j=0} \quad (2.20)$$

the partial derivatives can be solved numerically and we can write a matrix

$$A_{j,j} = 1 + 2 \sum_{\substack{a=1 \\ a \neq j}}^N \frac{1}{|u_j - u_a|^3} \rightarrow j = j \quad (2.21)$$

$$A_{i,j} = \frac{-2}{|u_i - u_j|^3} \rightarrow i \neq j \quad (2.22)$$

such that the Lagrangian can be re-written as:

$$L = \frac{M}{2} \left[\sum_{i=1}^N (\dot{q}_i)^2 - \nu^2 \sum_{i,j=1}^N A_{i,j} q_i q_j \right] \quad (2.23)$$

And finally, we can solve for the eigenstates and eigenvalues of $A_{i,j}$ as:

$$\sum_{i,j=1}^N A_{i,j} b_j = \omega_j b_j \quad (2.24)$$

Where ω_j are the eigenvalues or mode frequencies and b_j are eigenvectors that describe how each ion participates in each mode of motion. Deriving the radial

modes is more complicated, but one still ends up with eigenstates and eigenvalues of a coupled set of equations [39, 54]. Two of these modes of motion are depicted in **Figure 2.12**, and more discussion of their nature is given further down. We can write down an unperturbed Hamiltonian for these modes as:

$$\mathcal{H}_{U,m} = \sum_{m=1}^N \hbar \omega_m \hat{a}_m^\dagger \hat{a}_m \quad (2.25)$$

where ω_m are the N different motional modes of the N -ion long ion chain in any particular axis. Since the ions are confined as harmonic oscillators, \hat{a}^\dagger and \hat{a} are raising and lowering operators, respectively. We can define a time-dependent position operator of the form:

$$\vec{q}(t) = \sum_{i=1}^N b_{i,m} x_{0,m} (\hat{a}_m^\dagger e^{i\omega_m t} + \hat{a}_m e^{-i\omega_m t}) = \sum_{i=1}^N \eta_{i,m} (\hat{a}_m^\dagger e^{i\omega_m t} + \hat{a}_m e^{-i\omega_m t}) \quad (2.26)$$

$b_{i,m}$ is the eigenvector describing the coupling between each ion and mode, $x_{0,m} = \sqrt{\hbar/2M\omega_m}$ is the spread of the zero-point wavefunction, where M is the ion mass. $\eta_{i,m}$ is the Lamb-Dicke parameter and the product of $b_{i,m} \times x_{0,m}$.

The coupling of phonons throughout the ionic chain can be considered in two different time scales. At very short time scales, we can consider exciting phonons on specific ions in a local manner [55–58]. These phonons are not yet coupled to the entire chain, but they will quickly propagate from ion to ion via a hopping term in the Hamiltonian. This can be seen in **Figure 2.11**, where a local phonon was excited on the middle ion of a three-ion chain. The amount of time allowed

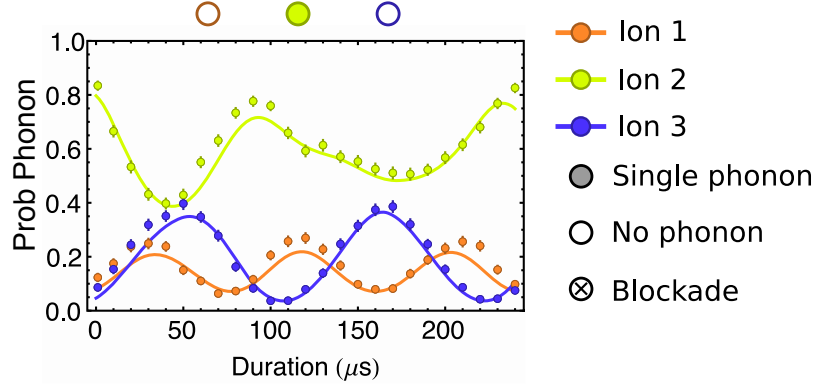


Figure 2.11: Plot of a single phonon moving between ion sites. Initially prepared as a local phonon on ion 2, the phonon hops to ions 1 and 3 with frequencies dependent on the trap parameters.

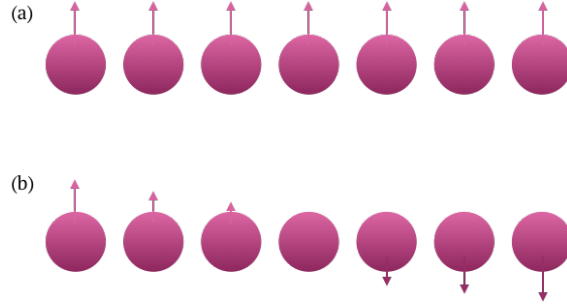


Figure 2.12: Cartoon depiction of the common (a) and tilt (b) modes of motion on a 7 ion chain.

for free-phonon hopping was scanned and the probability of measuring a phonon on each ion was measured [55]. Though unexplored in that manuscript, the Fourier transform of each ion's phonon occupancy results in the eigenvalues and eigenvectors of **Equation 2.24** in the long timescale formalism of the phonon coupling [58]. At these long times, phonons are no longer local to each ion, rather they are global parameters experienced by the entire ion chain. In ideal traps of N ions, there are N normal modes and highest energy mode describes all the ions moving together in phase, **Figure 2.12a**. The second highest energy mode occurs when the ions' motion tilts around the center ion, **Figure 2.12b**.

We can leverage these motional modes to generate entanglement in many different ways [59]. The so-called Cirac-Zoller gate was the first to do so and uses a sequence of quantum gates that excite either spin and motion or just spin to generate entanglement [60, 61]. They begin by performing a $\pi/2$ pulse on the carrier transition, whose Rabi frequency, Ω_c is first-order sensitive to motional Fock state for counter-propagating Raman beams (see following chapter). Next, a 2π pulse is performed on the common-mode, blue sideband transition. The Rabi frequency of this transition on ion i , $\Omega_{i,BSB}$, is proportional to the square root of the phonon occupancy, n_{BSB} :

$$\Omega_{i,BSB} = \eta_{i,BSB} \Omega_c \sqrt{n+1} \quad (2.27)$$

where $\eta_{i,BSB}$ is defined above in **Equation 2.26** and n is the motional occupancy . Therefore, the gate can only be performed with high fidelity if the motional state is well-known. Soon after, another method of generating entanglement was discovered that made use of phonons with relaxed constraints on the knowledge of the phonon occupancy [62–64]. This gate will be discussed in the next chapter where we will look at performing multiple types of single- and two-qubit gates coherently.

Chapter 3: Coherent Ion-Laser Interactions

3.1 Coherent Qubit Operations

A perfect qubit is useless unless you can put it to work. Aside from the probabilistic processes we leverage to perform high-fidelity qubit operations described in the last chapter, we also need coherent operations to perform actual computations on our qubits. Put another way, in the last chapter we discussed a physical realization of a qubit using the ground-states of $^{171}\text{Yb}^+$ atoms and how to cool, initialize, and detect that qubit. In this chapter, we will discuss how we manipulate those qubits as well as entangle them together. For convenience, \hbar will be set to 1 for the equations in this chapter.

Different qubits are driven by different mechanisms. Superconducting qubits are resonant with microwave fields that are delivered directly to the qubits with waveguides. Some ion qubits, like $^{40}\text{Ca}^+$, are resonant with an optical transition. Therefore, researchers can drive the qubit with a single laser beam. $^{171}\text{Yb}^+$ is like a combination of both: it has a microwave transition resonant at 12.642 GHz, and

can be driven directly with microwave photons or by using two laser beams that have the appropriate frequency shift between them. Having both available sources of qubit drive is very worthwhile. Microwaves are emitted by a microwave horn that applies a global rotation gate onto the ions with very high fidelity. The laser transition, known as a Raman transition, can be made ion-specific with greater ease, and we use it to implement individual addressing. The somewhat unique individual addressing ability allows us to perform arbitrary quantum computations with our qubits, as the system has a universal gate set. Furthermore, the laser-based drive can more easily transfer momentum into the ion chain compared to microwave fields, which is necessary from generating entanglement.

3.2 Raman Transitions

The Raman transitions work by coupling two electronic states of an atomic system together using two laser beams that are far far-detuned from a third state. Since the detuning from the third state, Δ , is large in comparison to the overall Rabi frequency, we can make the approximation that the ion will never spend anytime in that third states, and the two states will be coupled together. In our case, we want to be able to coherently transfer population between the qubit levels by coupling them to two highly-detuned excited states, as shown in **Figure 3.1**.

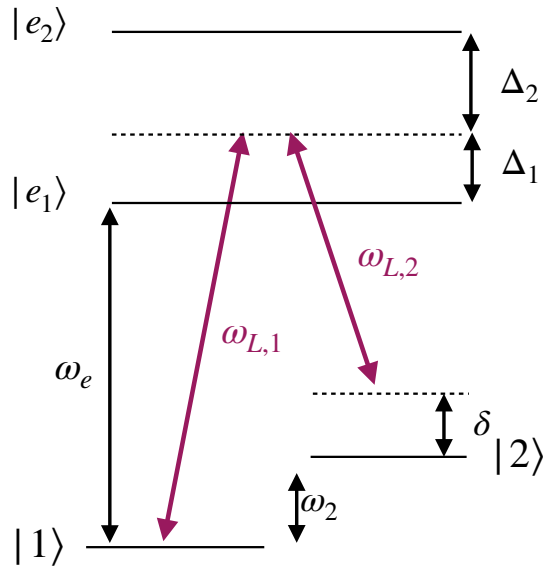


Figure 3.1: Energy-level diagram for a generic Raman process with two excited levels ($|e_1\rangle$ and $|e_2\rangle$). The purple lines indicate laser frequencies. For our experimental purposes, δ can be changed arbitrarily over time.

We can begin our discussion of our Raman system by looking at the unperturbed Hamiltonian of a three-level system:

$$\mathcal{H}_0 = \sum_{i=1,2,e} \hbar\omega_i |i\rangle\langle i| \quad (3.1)$$

Where i is an index of states 1, 2, and e. $|1\rangle$ is the ground state with zero-point energy ($\omega_1 = 0$). $|2\rangle$ and $|e\rangle$ are excited states with respective energies $\hbar\omega_2$ and $\hbar\omega_e$ with respect to the zero-point energy. We can define a time-varying wavefunction for this system as:

$$|\psi\rangle = \sum_{i=1,2,e} c_i(t) |i\rangle \quad (3.2)$$

Where each $c_i(t)$ is a complex probability amplitude whose wavefunction is oscillating with respect to the ground-state energy as: $c_i(t) = c_i(0)e^{i\omega_i t}$. For $^{171}\text{Yb}^+$ ions, $|1\rangle$ and $|2\rangle$ are the qubit levels, and the laser frequency we use for Raman transitions is detuned from two excited states: the $^2SP_{1/2}$ or $^2P_{3/2}$ manifolds with a 33 THz or 66 THz detuning, respectively. Therefore, our derivation will include the second excited state eventually. For now, only one excited state will be considered.

As mentioned, the energy levels are coupled using two laser fields. One couples states $|1\rangle \leftrightarrow |e\rangle$ with a laser frequency $\omega_{L,1} = \omega_e + \Delta$, where Δ is a large detuning. The other laser couples $|2\rangle \leftrightarrow |e\rangle$ with frequency $\omega_{L,2} = \omega_{L,1} - \omega_2 - \delta$ with a detuning, δ , see **Figure 3.1**. These transitions are electric dipole transitions, so we will can couple the qubit states with oscillating electric fields. Since there are two involved,

we'll write them as a sum over $j = \{1, 2\}$:

$$\mathbf{E} = \sum_{j=1}^2 \mathbf{E}_j = \frac{1}{2} \sum_{j=1}^2 A_j \vec{\epsilon}_j e^{-i(\omega_{L,j}t - \phi_j(x))} + h.c. \quad (3.3)$$

Where the polarization of each beam is described by $\vec{\epsilon}_j$ and the complex amplitude of each beam is depicted as A_j . The phase of each laser beam with respect to the ion position is absorbed in $\phi_j(x)$. At this point in the thesis, we will assume that the ions are completely stationary to derive the Raman coupling, but later in the thesis we will allow the ions to move, which will expand our toolbox of laser operations into motional excitation. Next, we can define an electric dipole operator that describes the coupling between states via an electric dipole transition as:

$$\vec{\mu} = \sum_{j=1}^2 \mu_{2,e_j} |2\rangle\langle e_j| + h.c + \mu_{1,e_j} |1\rangle\langle e_j| + h.c \quad (3.4)$$

where $\mu_{i,j}$ is the reduced dipole matrix element for states $|i\rangle$ and $|j\rangle$, and $\mu_{i,j}^* = \mu_{j,i}$.

Next, we can define an interaction Hamiltonian:

$$\begin{aligned} \mathcal{H}_{\mathcal{I}} = -\vec{\mu} \cdot \mathbf{E} = \\ -\frac{1}{2} (\mu_{2,e_1} \mathbf{E}_1 |2\rangle\langle e| + \mu_{2,e_2} \mathbf{E}_2 |2\rangle\langle e| + \mu_{1,e_1} \mathbf{E}_1 |1\rangle\langle e| + \mu_{1,e_2} \mathbf{E}_2 |1\rangle\langle e| + h.c) \end{aligned} \quad (3.5)$$

The wavefunction defined in **Equation 3.2**, the unperturbed Hamiltonian from **Equation 3.1**, and the interaction Hamiltonian can be combined into a time-dependent Schrödinger equation, which produces a coupled set of three differential

equations.

$$\begin{aligned}
i|\dot{\psi}\rangle &= (H_0 + H_I) |\psi\rangle \\
i\dot{C}_1 &= -\frac{1}{2}C_e \sum_{j=1}^2 \mathbf{E}_j \mu_{e_j,1} \\
i\dot{C}_2 &= -\frac{1}{2}(C_e \sum_{j=1}^2 \mathbf{E}_j \mu_{e_j,2} + C_2 \omega_2) \\
i\dot{C}_e &= -\frac{1}{2}(C_1 \sum_{j=1}^2 \mathbf{E}_j \mu_{1,e_j} + C_2 \sum_{j=1}^2 \mathbf{E}_j \mu_{2,e_j} + C_e \omega_e)
\end{aligned} \tag{3.6}$$

To simplify the notation, the electric field amplitudes, reduced dipole matrix element, and phase are absorbed into the following shorthand notation: $g_{i,e_j} = -\mu_{i,e_j} A_j e^{i\phi_j(x)}$. Where i is a sum over energy levels and j is still a sum over laser beams. By redefining the wavefunction as one that oscillates at the level splittings, we can move into the rotating frame of the energy levels:

$$|\widetilde{\psi}\rangle = \sum_{i=1,2,e} \widetilde{c}_i e^{i\omega_i} |i\rangle = \widetilde{C}_1 |1\rangle + \widetilde{C}_2 e^{i\omega_2} |2\rangle + \widetilde{C}_e e^{i\omega_e} |e\rangle \tag{3.7}$$

Now, **Equation 3.6** can be re-written as:

$$\begin{aligned}
i\widetilde{C}_1 &= -\frac{1}{2}\widetilde{C}_e \sum_{j=1}^2 g_{1,e_j} e^{i(\omega_e + \omega_{L,j})t} + g_{1,e_j}^* e^{i(\omega_e - \omega_{L,j})t} \\
i\widetilde{C}_2 &= -\frac{1}{2}\widetilde{C}_e \sum_{j=1}^2 g_{2,e_j} e^{i(\omega_e + \omega_{L,j} - \omega_2)t} + g_{2,e_j}^* e^{i(\omega_e - \omega_{L,j} - \omega_2)t} \\
i\widetilde{C}_e &= -\frac{1}{2} \sum_{j=1}^2 [\widetilde{C}_1 (g_{1,e_j}^* e^{i(\omega_e + \omega_{L,j})t} + g_{1,e_j} e^{i(\omega_e - \omega_{L,j})t}) + \\
&\quad \widetilde{C}_2 (g_{2,e_j}^* e^{i(\omega_e + \omega_{L,j} + \omega_2)t} + g_{2,e_j} e^{i(\omega_e - \omega_{L,j} + \omega_2)t})]
\end{aligned} \tag{3.8}$$

Notably, there are several terms that are oscillating with much larger frequencies

than other terms. Using the rotating wave approximation, we can make the argument that terms that oscillate with a frequency greater than $\omega_L + \omega_e$ will be averaged out by performing "slow" experiments. These terms can be approximated to 0 and can be ignored. Secondly, we will require that $\omega_2 \ll \omega_L$, terms with a frequency of ω_2 can remain. With these approximations:

$$i\widetilde{\dot{C}}_1 = -\frac{1}{2}\widetilde{C}_e \sum_{j=1}^2 g_{1,e_j}^* e^{i\Delta_j t} \quad (3.9)$$

$$i\widetilde{\dot{C}}_2 = -\frac{1}{2}\widetilde{C}_e \sum_{j=1}^2 g_{2,e_j}^* e^{i(\Delta_j + \omega_2)t} \quad (3.10)$$

$$i\widetilde{\dot{C}}_e = -\frac{1}{2} \sum_{j=1}^2 [\widetilde{C}_1 g_{1,e_j} e^{-i(\Delta_j)t} + \widetilde{C}_2 g_{2,e_j} e^{-i(\Delta_j - \omega_2)t}] \quad (3.11)$$

where $\Delta_1 = \omega_e - \omega_{L,1} = \Delta$ and $\Delta_2 = \omega_e - \omega_{L,2} = \Delta + \delta + \omega_2$. Since the laser detunings Δ_j from the excited state are very large, we can adiabatically eliminate any coupling to this state and claim that $\widetilde{\dot{C}}_e = 0$. Therefore, **Equation 3.11** can be integrated with respect to time to determine its steady-state value and pull \widetilde{C}_1 and \widetilde{C}_2 outside the integrand by the same adiabatic arguments as above. Then:

$$i\widetilde{C}_e(t) = -\frac{1}{2} \int \sum_{j=1}^2 [\widetilde{C}_1 g_{1,e_j} e^{-i(\Delta_j)t} + \widetilde{C}_2 g_{2,e_j} e^{-i(\Delta_j - \omega_2)t}] dt \quad (3.12)$$

$$\widetilde{C}_e(t) = -\frac{1}{2} \sum_{j=1}^2 \left[\frac{\widetilde{C}_1 g_{1,e_j} e^{-i(\Delta_j)t}}{-i\Delta_j} + \frac{\widetilde{C}_2 g_{2,e_j} e^{-i(\Delta_j - \omega_2)t}}{-i(\Delta_j - \omega_2)} \right] \quad (3.13)$$

which can be plugged into **equations 3.9** and **3.10** to uncover the coupling between the qubit levels. We will also make the approximation that $\Delta_j - \omega_2 \sim \Delta_j$ and drop

the tildes from the probabilities.

$$\dot{C}_1 = - \sum_{j=1}^2 \frac{1}{4\Delta_j} [C_1 |g_{1,e_j}|^2 + C_2 g_{1,e_j} g_{2,e_j}^* e^{i\omega_2 t}] \quad (3.14)$$

$$\dot{C}_2 = - \sum_{j=1}^2 \frac{1}{4\Delta_j} [C_1 g_{1,e_j}^* g_{2,e_j} e^{-i\omega_2 t} + C_2 (|g_{2,e_j}|^2)] \quad (3.15)$$

$$\mathcal{H}'_{\mathcal{I}} = \begin{pmatrix} \delta_1 & \Omega_R/2e^{i\omega_2 t} \\ \Omega_R^*/2e^{-i\omega_2 t} & \delta_2 \end{pmatrix} \quad (3.16)$$

where

$$\delta_i = - \sum_{j=1}^2 \frac{1}{4\Delta_j} |g_{i,e_j}|^2, \quad \Omega_R = - \sum_{j=1}^2 \frac{1}{2\Delta_j} g_{1,e_j} g_{2,e_j}^* \quad (3.17)$$

These equations describe Raman coupling for a system with a CW laser and a single excited state. In our experiment, we use a 355 nm, pulsed laser that couples the qubit levels in $^{171}\text{Yb}^+$ with two separate excited states. Luckily, re-deriving the work above produces very similar results, and we only need to change a few terms in the interaction Hamiltonian to include these features. The electric field that describes our laser changes to:

$$\mathbf{E} = \sum_{j=1}^2 \mathbf{E}_j = \frac{1}{2} \sum_{j=1}^2 f(t - nT) \vec{\epsilon}_j e^{-i(\omega_{c_L,j} t - \phi_j(x))} + h.c. \quad (3.18)$$

where $f(t - nT)$ is a function that describes pulses of length T and $\omega_{c_L} = \omega_L$ is the carrier frequency of the laser field that is equivalent to the CW frequency. Assuming that the interactions will last much longer than T , f can be approximated as having

infinite pulses and take a Fourier transform:

$$\mathbf{E} = \sum_{j=1}^2 \mathbf{E}_j = \frac{1}{2} \sum_{j=1}^2 f(\omega_{rep}) \vec{\epsilon}_j e^{-i((\omega_{cL,j} + \omega_{rep})t - \phi_j(x))} + h.c. \quad (3.19)$$

where $f(\omega_{rep})$ describes a frequency comb with comb-teeth separated by the repetition rate of the laser ω_{rep} . With these, the sums in **Equation 3.17** can be re-defined such that the index j is expanded to include the frequencies of each comb-tooth in each Raman beam. To account for a second excited state with a second detuning, an additional summation must be added to **Equation 3.17**:

$$\delta_i = - \sum_{k=2}^2 \sum_{j=1}^2 \frac{1}{4\Delta_j} |g_{i,e_j^k}|^2, \quad \Omega_R = - \sum_{k=2}^2 \sum_{j=1}^2 \frac{1}{2\Delta_j^i} g_{1,e_j^k} g_{2,e_j^k}^* \quad (3.20)$$

where the coupling variables g_{i,e_j^k} are now indexed by excited state k , and Ω_R is the Rabi frequency between the qubit levels. The qubit levels are now coherently coupled by the beatnotes generated by the interference of the two Raman beams over the ions. The coherence of this atom-laser interaction is essential for controlling our qubits. In the laboratory frame, if the beatnote decoheres or dephases from qubit splitting, no information can be encoded in the two-level system. Therefore, it is important to think deeply about the approximations made in this derivation and compare them to real experimental values:

Approximation	Realization
$\omega_2 \ll \omega_L$	12.642 GHz \ll 33 (66) THz
$T \ll 1/\Omega_R$	3 ns \ll 10 μ s

Clearly, we are deep within the approximations in both cases by many orders

of magnitude.

Next, we will perform one more rotating wave approximation onto the interaction Hamiltonian in **Equation 3.16** to get rid of the oscillatory terms.

$$|\psi'\rangle = C'_1 e^{-i\delta_1 t} |1\rangle\langle 1| + C'_2 e^{-i(\omega_2 - \delta - \delta_2)t} |2\rangle\langle 2| \quad (3.21)$$

To remind the reader, δ is the difference between the laser beatnote and the qubit resonance, and ω_2 is the qubit splitting, see **Figure 3.1**. In this rotating frame, the time-evolved wavefunction is:

$$i\dot{C}'_1 = C'_2 \Omega_R e^{i\omega_2 t} e^{-i(\omega_2 - \delta - \delta_2 + \delta_1)t} = C'_2 \Omega_R e^{-i\mu t} \quad (3.22)$$

$$i\dot{C}'_2 = C'_1 \Omega_R^* e^{-i\omega_2 t} e^{i(\omega_2 - \delta - \delta_2 - \delta_1)t} = C'_1 \Omega_R^* e^{i\mu t} \quad (3.23)$$

Where $\mu = \delta + \delta_1 + \delta_2$ denotes resonantly driving the qubit when $\mu = 0$. In this way, we can consider δ_1 and δ_2 as simply light shifts that change the qubit splitting and δ is the frequency of the beatnote defined by the Raman lasers. We can now re-write our interaction Hamiltonian in terms of spin operators of the form:

$$\mathcal{H}_I^{QC} = \begin{pmatrix} 0 & \Omega_R/2 e^{i(\mu t + \phi(x))} \\ \Omega_R^*/2 e^{-i(\mu t + \phi(x))} & 0 \end{pmatrix} = \frac{\Omega_R}{2} (\hat{\sigma}_+ e^{-i(\mu t + \phi)} + \hat{\sigma}_- e^{i(\mu t + \phi(x))}) \quad (3.24)$$

Returning the laser phase back into the Hamiltonian, as it will be used very soon. This Hamiltonian represents the ability to perform rotational gates in the x-y plane of the Bloch sphere; essential when creating a universal quantum computer capable

of performing any quantum computation. By the end of the next chapter, we will expand our toolkit with entangling gates via motional excitations.

3.3 Exciting Motion Raman Transitions

The Raman beams interfere over the ion chain while the ions oscillate at the secular frequency. Up until now, the details of this time-varying interference was shelved into the phase of the Raman beams, $\phi(x)$, in **Equation 3.18**. Now we need to unpack this term.

This phase can be written as $\phi(x) = \Delta\phi + (\vec{k}_1 - \vec{k}_2) \cdot \vec{x}_i$. Where $\Delta\phi = \phi_1 - \phi_2$ is the phase difference between the Raman beams; as well as a non-trivial spatial term that couples the ion location (\vec{x}_i) with the difference between wave vectors of the beams ($\Delta\vec{k} = \vec{k}_1 - \vec{k}_2$). As mentioned in **Equation 2.26**, \vec{x}_i can be written as a sum of the nominal position the ion (x_i^0) and a quantized displacement operator from that position (\vec{q}_i). The phase due to the nominal position is absorbed into $\Delta\phi$, and the overall phase is:

$$\phi(x) = \Delta\phi + \Delta\vec{k} \cdot \vec{q}_i = \Delta\phi + \sum_{i,m=1}^N \eta_{i,m} [\hat{a}_m^\dagger e^{i\omega_m t} + \hat{a}_m e^{-i\omega_m t}] \quad (3.25)$$

where $\eta_{i,m} = \Delta k b_{i,m} \sqrt{\hbar/2m\omega_m}$, is the Lamb-Dicke parameter. Though it contains the normalized spin-phonon coupling term, it is most crucially a comparison of the zero-point wavefunction of each phononic mode with the wavelength of the laser beatnote. If the Raman beams are in counter-propagating configuration, then $\Delta k = \vec{k}_1 - \vec{k}_2 = k - (-k) = 2k = 4\pi/(355\text{nm})$. The zero-point wavefunction of each

phonon mode as $x_{0,m} = \sqrt{\hbar/2M\omega_m}$, which can be thought of as the wavefunction spread due to the excitation of phonon m . The zero-point wavefunction of the common mode of motion when trapping $^{171}\text{Yb}^+$ with a trap depth of 3.05 MHz is 3.1 nm. As such, we can claim that:

$$\eta_{i,1} \sim 3 \times 4\pi/355 \sim 1/120 = 0.01 \ll 1 \quad (3.26)$$

The smallness of the Lamb-Dicke parameter ($\eta \ll 1$) is called the Lamb-Dicke regime and is crucial for coherently exiting motion, as will be clear later on. Clearly, using $^{171}\text{Yb}^+$ ions and 355 nm light, we can easily operate deep in the Lamb-Dicke regime.

Now, the interaction Hamiltonian in **Equation 3.24** can be rewritten using this expanded phase and its Lamb-Dicke parameter:

$$\begin{aligned} \mathcal{H}_I^{QC} &= \frac{\Omega_R}{2} (\hat{\sigma}_+ e^{-i(\mu t + \Delta\phi + \vec{\Delta}\vec{k})} + \hat{\sigma}_- e^{i(\mu t + \phi(x))}) \\ \mathcal{H}_I^{QC} &= \frac{\Omega_R}{2} \sum_{i,m=1}^N (\hat{\sigma}_+ e^{i(\mu t + \Delta\phi)} e^{i[\eta_{i,m}(\hat{a}_m^\dagger e^{i\omega_m t} + \hat{a}_m e^{-i\omega_m t})]} + h.c.) \end{aligned} \quad (3.27)$$

In the Lamb-Dicke regime, $\eta \ll 1$, and a power series expansion around it can be performed as:

$$\begin{aligned} \mathcal{H}_I^{QC} &= \frac{\Omega_R}{2} \sum_{i,m=1}^N (\hat{\sigma}_+ e^{i(\mu t + \Delta\phi)} [1 - i\eta_{i,m}(\hat{a}_m^\dagger e^{i\omega_m t} + \hat{a}_m e^{-i\omega_m t}) + O(\eta_{i,m}^2)] + h.c.) \\ &\approx \frac{\Omega_R}{2} \sum_{i,m=1}^N \hat{\sigma}_+ [e^{i(\mu t + \Delta\phi)} - i\eta_{i,m}(\hat{a}_m^\dagger e^{i[(\mu + \omega_m)t + \Delta\phi]} + \hat{a}_m e^{-i[(\omega_m - \mu)t - \Delta\phi]}) + h.c.] \end{aligned} \quad (3.28)$$

Equation 3.28 is the major result of this derivation up till now. In it, the ability to coherently Rabi flop and drive qubit rotations is attained by setting $\mu = 0$. Since the derivation is now including motional states, we must re-define the wavefunction to include the motion:

$$|\psi\rangle = C_1 |1, n\rangle + C_2 |2, n\rangle \quad (3.29)$$

where n describes the phononic Fock state. As seen in **Equation 3.28** highly off-resonant motional transitions are present while Rabi flopping. With another rotating-wave approximation [65], the Rabi rate can be written as:

$$\Omega_R^n = \frac{\Omega_R}{2} \langle n' | e^{i\eta(\hat{a}^\dagger + \hat{a})} | n \rangle \quad (3.30)$$

In this way, the phonon number is sampled during Rabi oscillations. If the state of the trapped ion includes a distribution of Fock states, then several Rabi frequencies will be driven simultaneously [66]. This will cause a decay and an eventual revival as the different frequencies destructively and then constructively interfere. Clearly, this decay translates to gate infidelity that should be minimized. The ultimate way to do so is to use co-propagating Raman beams. In this case, $\Delta\vec{k} = 0$, and no motional excitation would occur during Rabi flopping. An approach to merely limit this effect is to cool an ion chain to near its motional ground state before beginning experiments. The Rabi flopping will still decay as there will always be some residual motional excitation.

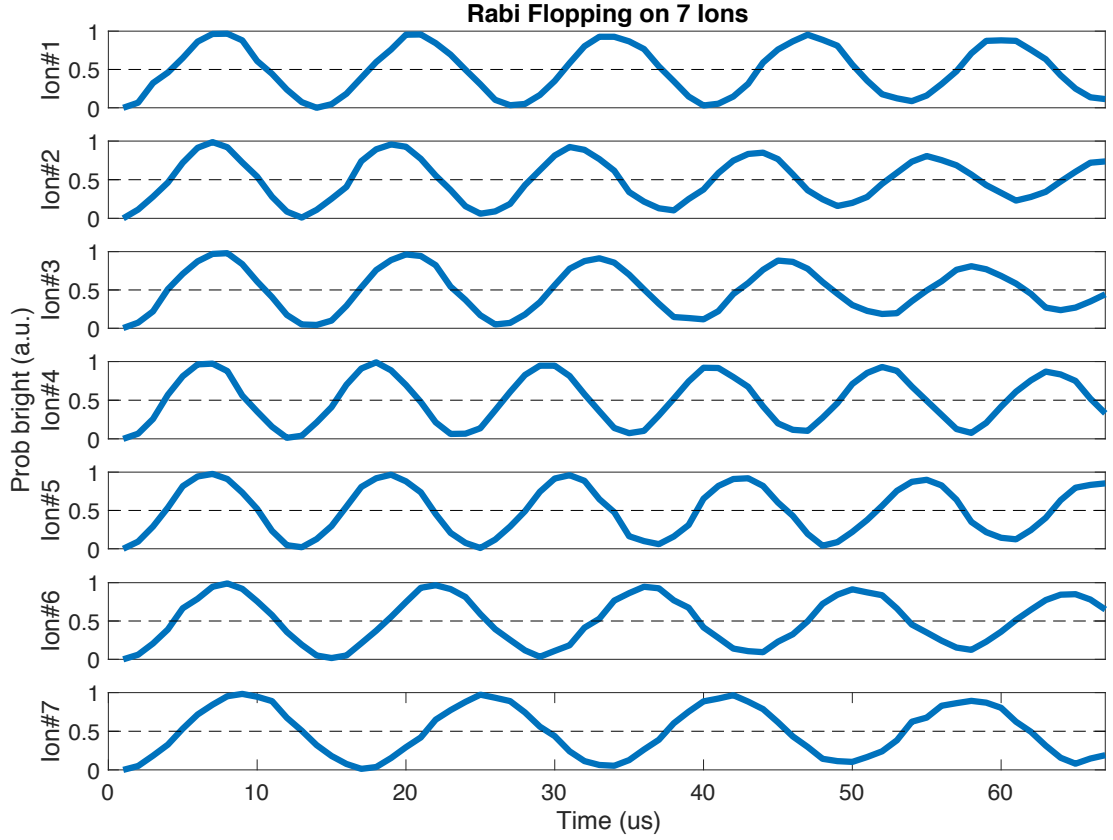


Figure 3.2: Raman beams are used to sideband cool a Doppler-cooled ion chain and then perform Rabi flopping on 7 ions. Though hard to see, the flops are beginning to decay after the third oscillation to a peak of only $\sim 95\%$. This is due to beam pointing noise as well as a Debye-Waller decay. The average phonon occupancy for these experiments is $\bar{n} \approx 0.01$. Each ion and beam have a unique Rabi frequency, so measuring each Rabi frequency is part of the calibration procedure.

3.4 Exciting Motion

3.5 Generating Entanglement

As mentioned already, the common method for generating entanglement is to leverage the inherent all-to-all connectivity of the Coulomb interaction. Most state-of-the-art ion trap systems use this interaction to generation pair-wise entanglement of the form [35, 52, 53, 67–72]:

$$\mathcal{H}_{Is} = \Omega_{Is} \hat{\sigma}_x^i \hat{\sigma}_x^j \quad (3.31)$$

where the unitary transformation is a two-qubit rotation that can create entanglement between pairs. It can be applied globally in such a way that Ω_{Is} is much larger for nearby ions than further ions. This approach to generating entanglement is often used in quantum simulation experiments where a known, entangling Hamiltonian and the largest numbers of qubits are among the most useful metrics for such systems. Ω_{Is} can also be applied in an ion-specific manor if individual addressing is available. In this regime, only the pairs of ions that see Raman beams will get entangled. This method has is common for digital quantum computations, where it can be transformed into two-qubit gates like controlled-nots. We’ll delve more into that later.

To generate this interaction, the researcher must apply two beatnotes over the ions simultaneously. They both need the same detuning from sideband resonance and the same Rabi frequency. Doing so, the interaction Hamiltonian can be

manipulated with some algebra to be:

$$\begin{aligned}
\mathcal{H}_{IS} &= \frac{\Omega_R}{2} \sum_{i,m=1}^N \hat{\sigma}_+ \left[e^{i(\mu t + \Delta\phi_{blue})} - i\eta_{i,m} (\hat{a}_m^\dagger e^{i[(\mu+\omega_m)t + \Delta\phi]} + \hat{a}_m e^{-i[(\omega_m-\mu)t - \Delta\phi]} \right. \\
&\quad \left. + h.c.) + e^{i(-\mu t + \Delta\phi_{red})} - i\eta_{i,m} (\hat{a}_m^\dagger e^{i[(\mu+\omega_m)t + \Delta\phi]} + \hat{a}_m e^{-i[(\omega_m-\mu)t - \Delta\phi]} + h.c.) \right] \\
&= \sum_{i=1}^N \Omega_R \cos(\mu t + \phi_i^M) (\cos \Delta\phi_i^S \hat{\sigma}_y^i + \sin \Delta\phi_i^S \hat{\sigma}_x^i) + \\
&\quad \sum_{i,m=1}^N \Omega_R \cos(\mu t + \phi_i^M) (\hat{a}_m^\dagger e^{i[(\mu+\omega_m)t]} + \hat{a}_m e^{-i[(\omega_m-\mu)t - \Delta\phi]}) (\cos \Delta\phi_i^S \hat{\sigma}_x^i + \sin \Delta\phi_i^S \hat{\sigma}_y^i)
\end{aligned} \tag{3.32}$$

where $\phi^{M(S)} = (\Delta\phi_{blue} - (+)\Delta\phi_{red})/2$. The first term in this equation drives single-qubit rotations along the $\Delta\phi^S$ axis and can be ignored because it is so off-resonant. In the regime where this single-qubit rotation term cannot be ignored due to high laser intensities, it could be undone by simply applying a single-qubit rotation after the Ising gate. The second term creates spin-motion excitation along the axis perpendicular to $\Delta\phi^S$ within the x-y plane, we term this rotation operator as $\hat{\sigma}_\phi^i$:

$$\mathcal{H}_{Is} = \sum_{i,m=1}^N \Omega_R \cos(\mu t + \phi_i^M) (\hat{a}_m^\dagger e^{i[(\mu+\omega_m)t]} + \hat{a}_m e^{-i[(\omega_m-\mu)t - \Delta\phi]}) \hat{\sigma}_\phi^i \tag{3.33}$$

Lastly, taking a Magnus expansion of this Ising Hamiltonian gives the unitary evo-

lution operator as:

$$U_{Is}(\tau) = \exp\left[-i \int_0^\tau dt \mathcal{H}_{Is}(t) - \frac{-i}{2} \int_0^\tau dt_2 \int_0^{t_2} dt_1 [\mathcal{H}_{Is}(t_2), \mathcal{H}_{Is}(t_1)] + \dots\right] \quad (3.34)$$

Crucially, the commutation relation in the second-order term will appear as $[\hat{a}, \hat{a}^\dagger] =$

1. All higher-order terms will evaluate a commutation relation with unity (e.g. $[[\hat{a}, \hat{a}^\dagger], \hat{a}] = [1, \hat{a}] = 0$), so we can truncate the expansion at two terms without any approximations. The resultant unitary evolution that drives entangling operations is:

$$U_{Is}(\tau) = \exp\left[i \sum_{i,m=1}^N \mathcal{D}_{i,m}(\alpha, \tau) \hat{\sigma}_\phi^i + i \sum_{i,j=1}^N \chi_{i,j}(\tau) \hat{\sigma}_\phi^i \hat{\sigma}_\phi^j\right] \quad (3.35)$$

with the definitions:

$$\mathcal{D}_{i,m}(\alpha, \tau) = \alpha_{i,m}(t) \hat{a}_m + \alpha_{i,m}^*(\tau) \hat{a}_m^\dagger \quad (3.36)$$

$$\alpha(\tau) = -\eta_{i,m} \int_0^\tau \Omega_R(t) \sin(\mu(t)t - \phi^M) e^{i\omega_m t} dt \quad (3.37)$$

$$\begin{aligned} \chi_{i,j} = \sum_{m=1}^N \eta_{i,m} \eta_{j,m} \int_0^\tau \int_0^{t_2} dt_2 dt_1 [\Omega_R(t_2) \Omega_R(t_1) \\ \sin(\omega_m(t_2 - t_1)) \sin(\mu(t_2)t_2 + \phi^M) \sin(\mu(t_1)t_1 + \phi^M)] \end{aligned} \quad (3.38)$$

The two terms of **Equation 3.35** are two distinct types of interactions. The first term is a spin-dependent force that moves phonons through the complex plane and the second term is two-qubit rotation whose “Rabi frequency” (χ) is a geometric phase that is related to the area of the phonons’ trajectories through the complex plane. The two-qubit rotation can entangle two qubits if $\chi = \pi/4$. If $\chi = \pi/2$, the

gate is equivalent to two bit-flips along the ϕ -axis. In this way, the entangling gate is a two-qubit rotation where the ions rotate simultaneously and entanglement is excited and then de-excited.

Since the qubits are solely defined by their spin states, residual spin-motional excitation is equivalent to leaving information about the system in the motional degrees of freedom. While this is technically a coherent source of error that can be undone by running the interaction in reverse, it is extremely inconvenient to do so. Therefore, we treat the imperfect closure of phase-space as decoherence and make significant efforts to prevent it. Further on in **Chapter 3.9**, we will discuss different approaches to minimizing errors due to phase-space closure. The Rabi frequencies and the laser drive frequency in **Equation 3.35** will be modulated in time to ensure the phase-space closure and sufficient entanglement generation. Next, we will discuss leveraging the native interactions described above to affect digital quantum computations.

3.6 Digital Quantum Gates

In the previous section, we derived how shining Raman beams of different frequencies can cause Rabi flopping interactions and entangling interactions on chains

of trapped-ion qubits. We can write them as unitary operators:

$$\hat{R}_i(\theta, \varphi) = \exp[i \hat{\sigma}_\varphi^i \theta/2] = \begin{bmatrix} \cos(\theta) & -ie^{-i\varphi}\sin(\theta) \\ -ie^{i\varphi}\sin(\theta) & \cos(\theta) \end{bmatrix} \quad (3.39)$$

$$\hat{\phi}_{i,j}(\chi, \phi) = \exp[i \hat{\sigma}_\phi^i \hat{\sigma}_\phi^j \chi] = \begin{bmatrix} \cos \chi & 0 & 0 & ie^{i\phi} \sin \chi \\ 0 & \cos \chi & i \sin \chi & 0 \\ 0 & i \sin \chi & \cos \chi & 0 \\ ie^{i\phi} \sin \chi & 0 & 0 & \cos \chi \end{bmatrix} \quad (3.40)$$

These two matrices were the original set of digital gates performed in Refs. [11, 52].

Since then, an additional native gate has been added to the toolkit that advances the phase of the Raman beatnote (details in section 3.7). This gate takes the form:

$$\hat{R}_z^i(\vartheta) = \exp[i \hat{\sigma}_z^i \vartheta/2] = \begin{bmatrix} 1 & 0 \\ 0 & e^{i\vartheta} \end{bmatrix} \quad (3.41)$$

Equation 3.39 performs an arbitrary single-qubit rotation on ion i with any phase φ or angle θ . Resonant Rabi flopping is the coherent excitation of the qubit between eigenstates of $\hat{\sigma}_z$ and along some axis in the x-y plane defined by φ . φ is chosen by controlling the phase of the rf signal that determines the phase of the Raman beatnote. More details on the generation of this rf signal are in the following section. θ is controlled by properly measuring the Rabi frequency and determining the duration necessary to perform a rotation of $\pi/2$ on the ions. With this calibration, any arbitrary angle is converted into a duration. Since the Debye-Waller decay parameter is present during single-qubit rotations, rotation gates are optimized to have the lowest duration. For example, if θ is within the interval $[\pi, 2\pi]$, an identical unitary can be performed by flipping the sign of φ and setting

$\theta' = \theta - \pi$. Additionally, if θ is within the interval $[2\pi, 4\pi]$, setting $\theta' = \text{mod}(\theta, 2\pi)$ performs an equivalent unitary.

Equation 3.40 performs a two-qubit entangling gate between ions i and j . ϕ can be set to any arbitrary axis by choosing the phase of the Raman beatnote. In our experimental realization, ϕ is set to 0, and can be changed pragmatically using a basis transformation as: $\hat{\phi}\phi_1 = \hat{U}_T^\dagger \hat{\phi}\phi_0 \hat{U}_T$, where $U_T = R_z^{i,j}(\vartheta)$. When $\phi = 0$, the gate is termed an $\hat{X}\hat{X}$ interaction due to the $\sigma_x \hat{\sigma}_x$ term in the Hamiltonian. This nomenclature will be used throughout this thesis and reminds the reader that the phase of the interaction is set to 0. Many different approaches were explored to generate the unitary in **Equation 3.40**, and they are discussed in **Chapter 3.9**. Physical errors during these gate are discussed in the following section.

Since χ depends on the product of the Rabi frequencies for both ions involved, it is significantly more sensitive to Rabi frequency drift and requires more frequent calibration than the rotational gates. The same exact argument can be made for detuning errors. Therefore, we make efforts to minimize the use of the $\hat{X}\hat{X}$ gates possible and to use them with the lowest equivalent value of χ . In this case, it is useful to note that $\hat{X}\hat{X}_{i,j}(\pi/2) = \hat{R}_x^{i,j}(\pi)$. Since the rotational gates have much higher fidelity, this trade-off is very favorable. Therefore, we can use the following identity to minimize χ :

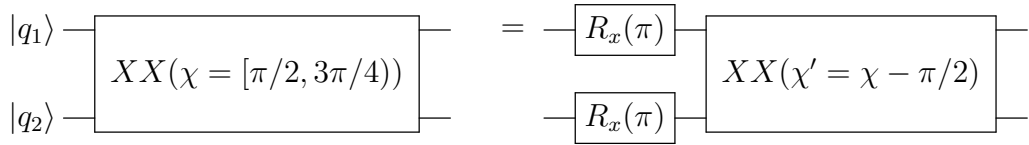


Figure 3.3: A useful identity for converting $\hat{X}\hat{X}$ gates with a large entanglement parameter (χ) into gates with a smaller parameter and two single-qubit gates.

In a similar vein, we can take advantage of negative χ values, which are implemented by rotating the qubit basis by π and the following identity:

$$\begin{array}{c} |q_1\rangle \\ |q_2\rangle \end{array} \begin{array}{c} \text{---} \\ \text{---} \end{array} \boxed{XX(\chi = [3\pi/4, \pi])} \begin{array}{c} \text{---} \\ \text{---} \end{array} = \begin{array}{c} \text{---} \\ \text{---} \end{array} \boxed{XX(\chi' = \pi - \chi)} \begin{array}{c} \text{---} \\ \text{---} \end{array}$$

Figure 3.4: A scheme for reducing the entangling parameter (χ) used during an experiment by flipping the sign of the XX interaction.

There are more intricate methods for reducing errors that use sets of digital quantum gates to minimize experimental error [73–75]. One such method is employed to reduce calibration errors on our experimental system. We use the so-called SK1 composite pulse which has the form:

$$|q_1\rangle \text{---} \boxed{R(\theta, \phi)} \rightarrow \text{---} \boxed{R(\theta, \phi)} \text{---} \boxed{R(2\pi, \phi - \beta)} \text{---} \boxed{R(2\pi, \phi + \beta)}$$

Figure 3.5: Combining several rotation gates to perform a single rotation with a higher fidelity than the gates combined. These composite pulses work by canceling out errors that are common to all three rotational gates. If the noise causing the errors is faster than a single gate, this technique will be less useful.

where $\beta = \cos^{-1}(\theta/(4\pi))$. This composite pulse is useful for improving rotational gate fidelity in the presence of Rabi frequency fluctuations that are much slower than the Rabi frequencies. A comparison of the SK1 composite pulse with the regular rotation is plotted in **Figure 3.6** for both π and $\pi/2$ gates. In the plot, the horizontal axis is the error on the Rabi frequency calibration normalized by the Rabi frequency. Both curves depicting SK1 pulses have a flat region around the desired rotation angle. In the example of performing a $\pi/2$ gate, the regular rotation is very steep and maximally susceptible to Rabi frequency errors. In contrast, the SK1 gate has a shelf at $\pi/2$ and calibration errors as large as $\sim 4\%$ of the Rabi frequency still result in high-fidelity $\pi/2$ rotations.

Composite pulses designed for $\hat{X}X$ gates exist, but would not necessarily cause an improvement. If the biggest error is residual motional excitation, then any information left entangled with a phonon at the end of the $\hat{X}X$ gate would still be lost. This is likely the error model of our system. If things improve and the largest errors in the gate are calibration errors on χ , then the composite pulses could work.

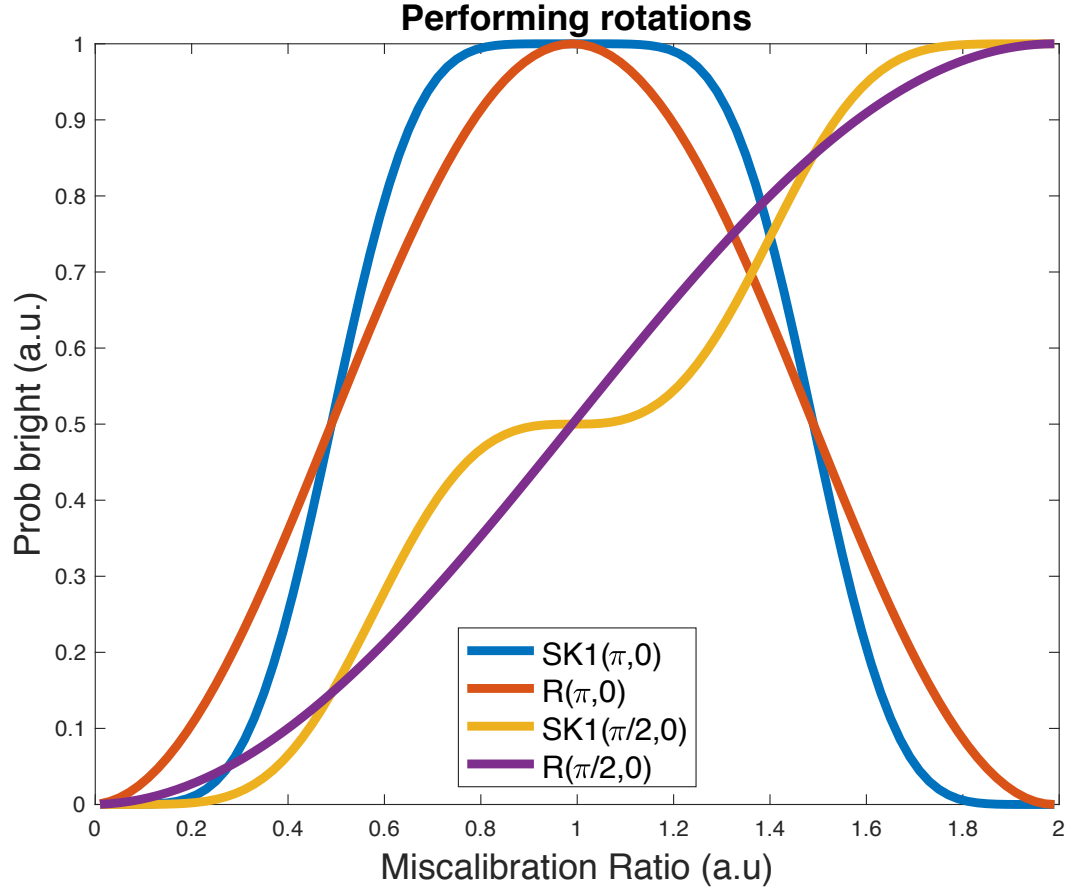


Figure 3.6: Comparison of rotation gates with SK1 composite gate. The horizontal axis is a miscalibration parameter that is multiplied with the ideal pulse angle. The vertical axis is the probability of the gate transforming $|0\rangle$ to $|1\rangle$. Though the SK1 pulse rotation is 4π longer than the rotation gate, the errors are greatly reduced when the miscalibration is within some limit of $\sim 5\%$.

3.7 Experimental Apparatus

The major distinguishing factor between the experimental apparatus used for the work in this thesis and other $^{171}\text{Yb}^+$ ion-trap experiments is the approach to individual addressing that was pioneered. Since then, other research groups and companies have implemented similar experimental architectures [76–78]. In our system, individual Raman beams are focused over individual ions with $5\text{ }\mu\text{m}$ spacing, and a much larger, counter-propagating Raman beam is focused over the beam from the other side. The combination of each individual beam and the global beam create the Raman process described in detail in the beginning of this chapter. Complete description of the optical design is discussed in Ref. [11].

The main tool used for individual addressing is a 32-channel AOM built by the Harris Corporation¹. This device resembles a normal AOM in that it contains a single crystal that laser light is focused through. Unique to this AOM is 32 transducers that create up to 32 spatially separate sound waves that propagate through the crystal. The sound waves perform their typical task of periodically modulating the index of refraction in the crystal which creates a diffraction grating that shifts the frequency, phase, and direction of some fraction of the incoming light [79]. Amazingly, though each AOM channel is only $\sim 400\mu\text{m}$ apart, the crosstalk is quite small. The total addressing crosstalk is due to an rf signal spilling over to a neighboring channel as well as a portion of the Gaussian laser beam spilling over onto neighboring ions. Put another way, the optical crosstalk is simply the amount

¹Model H-601 Series 32-Channel UV Acousto-Optic Modulator

of laser light intended for ion a that falls onto ion b and drives coherent rotations. The total addressing crosstalk is $2 - 3\%$ of the Rabi frequency of the target ion onto neighboring ions and $< 1\%$ onto non-neighboring channels, shown in **Figure 3.7**.

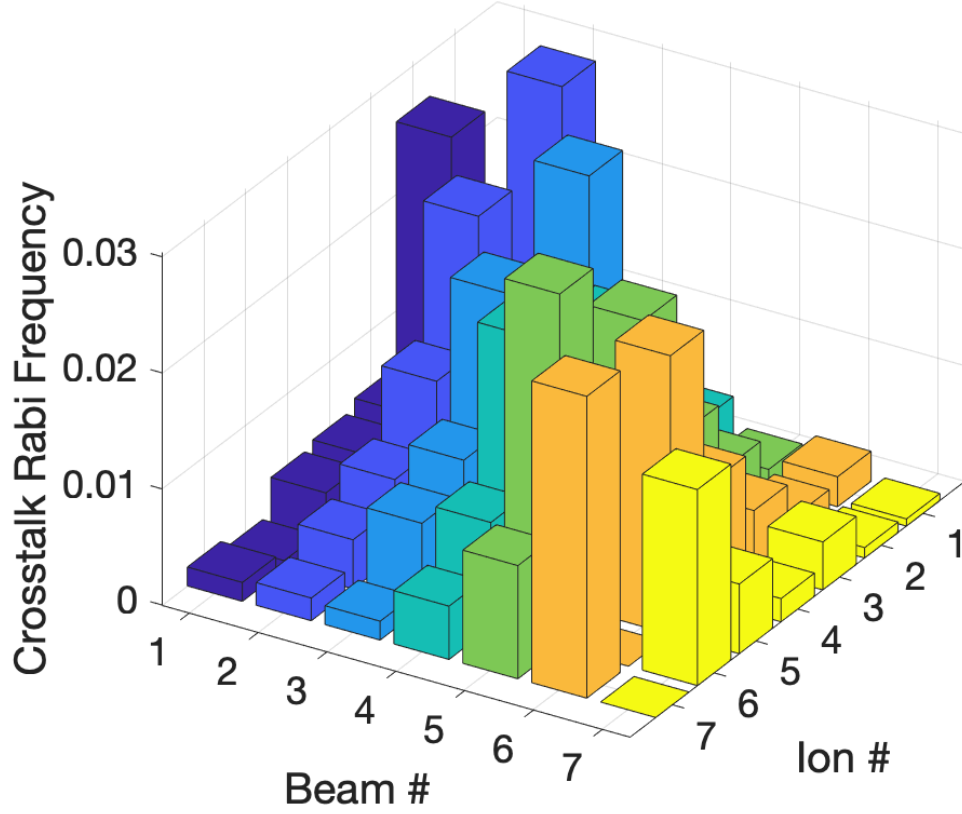


Figure 3.7: Raman beam crosstalk is measured by looking at the Rabi frequencies due to beams spilling over onto neighboring ions in the chain. Since Rabi frequencies are related to $\sqrt{I_{ind}}$, the intensity of these crosstalk beams are $1e - 3$ lower than on the target ions. As expected, neighboring ions have the most crosstalk of 2 – 3% of the Rabi frequencies of the target ions, while the Rabi frequencies on non-neighboring ions are $< 1\%$ of the target ions.

3.7.1 Raman Frequency Comb

The laser light that shines through the AOM's and over the ions originates from a picosecond mode-locked Coherent Paladin that boasts 4 W of optical power². Soon after it leaves the Paladin housing, a small amount of light is picked off the beam and sent into an ultrafast photodiode. We use this tiny amount of light to lock the drifting laser repetition-rate, as explained below. Next, the light is split into two beams: one that we use for individual addressing, and another beam we apply globally. The individual beam is sent through a diffractive optical element that splits it into 10 small beams. Each beam is focused into a $< 100 \mu\text{m}$ spot inside the 32 channel AOM, followed by a telescope expansion of the beams into a final objective with NA of 0.15-0.2. The beams finally are focused by said objective to a $2 \mu\text{m}$ waist over the ions. The collimated global beam is sent through its AOM and a delay state before it is shaped with cylindrical lenses for its objective. Once focused over the ions, the beam is $\sim 75 \mu\text{m}$ wide with respect to the ion chain axis and $\sim 10 \mu\text{m}$ perpendicular to that direction.

As mentioned above, the Fourier transform of the pulsed laser we use is a frequency comb centered at some carrier frequency $\sim 355 \text{ nm}$. The spacing between combteeth is the repetition rate of the laser, 118.314 MHz, so the broad spectrum of the laser already contains components necessary to bridge the qubit splitting of 12.642 GHz. By simple math: $118.315 \text{ MHz} \times 107 = 12.669 \text{ GHz}$. Therefore, interfering the n^{th} combtooth of the global beam with the appropriately-shifted

²Paladin Compact 355-4000

$(n+107)^{\text{th}}$ combtooth of the individual beam can drive the qubit on resonance or any of the other transitions within ~ 50 MHz bandwidth of the AOM's in use. Of course, the polarizations of the beams will also limit what transitions are possible. The main sources of error in this scheme is the drifting repetition rate of the laser, ω_{rep} , and the unwanted interference of combteeth that can cause large, second-order light shifts via a four-photon process.

This four-photon light shift and the typically smaller, two-photon light shift are both dominated by the high-intensity individual beams that are focused over the ion chain. They are derived by considering the beating of many different combteeth in the Raman beams. At the repetition rate of our laser, the four-photon shift is small compared to similar lasers with repetition rates only a few hundred KHz away. Nevertheless, it can be made as large as a few hundred KHz by changing the polarizations [80].

The two-photon light shift is of the order $\Delta E_2 \sim \frac{\Omega_0}{\Delta}$, where Δ is the 33 THz detuning of the Raman beams from the P levels. This term appears in the derivation of the Raman beams in **Equation 3.20** and was as large as 100's of Hz when Ref. [52] was published and when the individual beams were often driving the ions at their full power to maximize the Rabi frequency. Since then, we have lowered the intensity of the individual beams. In this low-intensity regime, the same relatively high Rabi frequencies required to drive the entangling operations could still be achieved. The two-photon light shifts were subsequently minimized below measurable levels.

On the other hand, the four-photon shifts were still measurable. These shifts are primarily caused by two types of polarization imperfection. The ideal polar-

izations of these Raman beams are designed to be in "lin-perp-lin" configuration where both Raman beams have purely linear polarizations that are perpendicular to one another as well as the quantization axis of the qubits. The obvious choice for counter-propagating beams with these polarizations is to align the quantization axis parallel with the Raman beams using magnetic fields. Generating linear polarization is done with an equal superposition of $\hat{\sigma}^+$ and $\hat{\sigma}^-$ light on the ions. Imperfect balancing of these two polarizations couples the qubit levels and the Zeeman states of the $^2S_{1/2}$ manifold by way of the $^2P_{1/2}$ manifold in a four-photon process. This is caused by unintended beatnotes between Raman combteeth [80]. This coupling causes a shift with a quadratic dependence on the imbalanced portion of the individual beam electric field, while the Rabi frequencies have a linear dependence on the electric field. Furthermore, any light that still has some component that points perpendicular to the quantization axis is π -polarized and can also cause a large, four-photon with a similar dependence on individual beam intensity. By lowering the intensity of the individual beams, these shifts dropped significantly ~ 200 Hz to < 5 Hz. Alongside the lowered intensities, the beam alignment was improved with the addition of spectator ions in the trap (see **Chapter 2**). Together, the average fidelities of controlled-not gates on a five-qubit chain went from $\sim 95\% \rightarrow \sim 98\%$.

Another important source of light shift is imbalance of the amplitudes of the red and blue beams during an $X\hat{X}$ gate. The excess light on either side of the carrier is too detuned and weak to cause excitations, but it will couple the qubit states via carrier and sideband transitions and cause a light shift. In the next paragraphs, we

will discuss how this source of error was minimized.

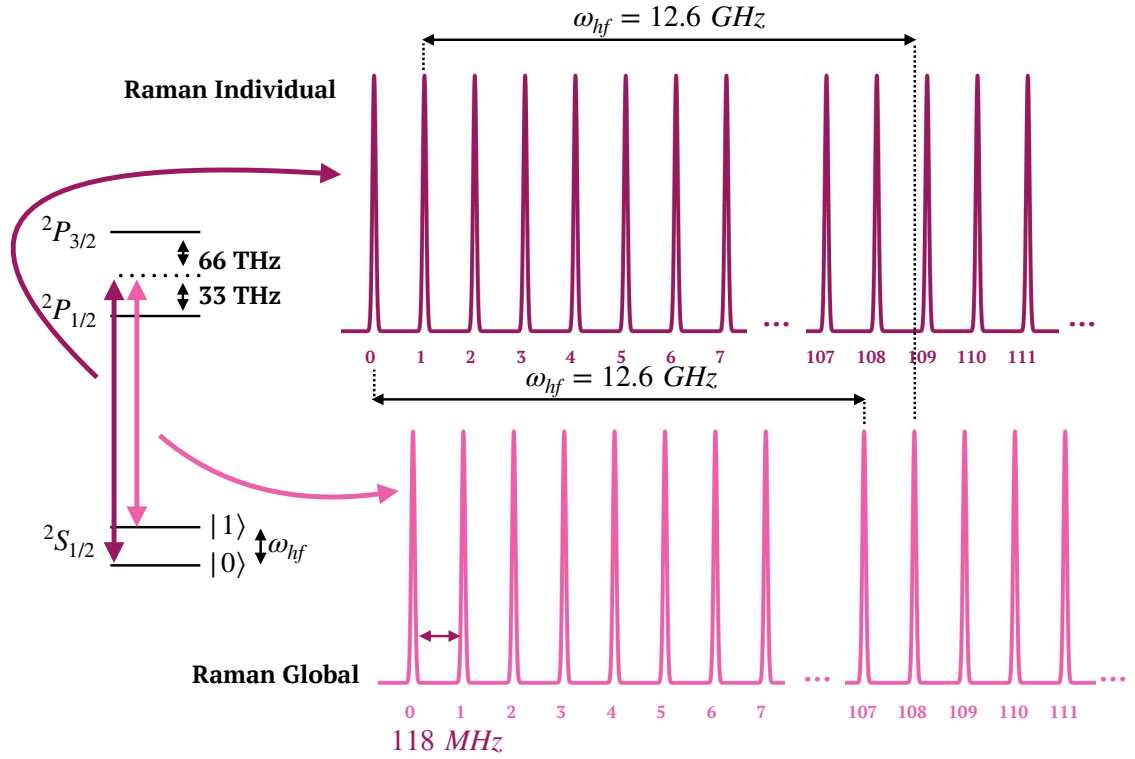


Figure 3.8: The two Raman beams and their respective frequency combs. The wide spectrum contained by each frequency combs allow a relatively high-frequency beatnote to be generated by shifting one beam a modest amount using an AOM.

3.7.2 Coherent RF Control

Once experimental errors due to light shifts are minimized to the greatest extent, the next step to coherently control the ions is to properly engineer rf signals that implement the rotating and $\hat{X}X$ interactions. Here, it is helpful to distinguish between decoherent and coherent processes. Doppler cooling, for example, is a probabilistic, dissipative process where one waits to scatter a certain number of photons off an atom. The time between the scattering events and the phase of the laser are immaterial: the only important metric is the total amount of time given a scattering rate and the initial ion temperature.

In contrast to this, the rotation and $\hat{X}X$ gates happen along some well-defined axis defined by the laser and the ion and the interaction conserves energy. We label the initial axis defined by the beatnote phase and the ion phase as the x-axis, which simplifies things considerably. From here, it is useful to consider both the ions and the Raman beatnote as clocks that need to be synchronized throughout the coherent portion of the experiment. Since the x-axis is defined at the beginning of every experiment, both clocks start at the same position in the beginning of the experiment. The ion clock processes at the qubit splitting when no laser light is shined onto it, but is potentially accelerated or decelerated by light shifts when light is present. The Raman beatnote clock is defined by the phase between the global and individual beams. It needs to match the ion clock in order to perform coherent operations. As the two clocks fail to synchronize, the ions dephase from the lasers and subsequent qubit operations are performed with the wrong phase. If the

qubit is driven by non-resonant light during an entangling gate, the phase accrued will still be determined by the resonant frequency. In this sense, the coherence of the system extends beyond the quantum states and into the driving mechanism.

In the first several publications produced on this experimental apparatus [11, 52, 67, 81, 82], this phase was defined by sending a single-tone synthesized waveform to the individual beams and a shaped set of rf pulses to the global beam. The individual beam rf signal was sent into a five-way splitter and then into five separate rf switches. These five switches controlled the individual addressing and the amplitude of the individual rf was set to its maximum to attain the highest possible Rabi frequencies, though also generating large light shifts. The global beam contained the bichromatic signal that implemented the $\hat{X}\hat{X}$ interaction as well as phase advances used to perform rotations along any axis. At this time, the ions were also unequally spaced due to the largely quadratic axial potential. The fix described in **Chapter 2** had not been implemented yet. Beyond the alignment problems, this approach had some flaws that were subsequently fixed. The main issue with this setup were the aforementioned large light shifts, the global phase, and the imbalance of the red and blue beams in the global beam during the entangling gates. The issue surrounding the phase of the global beam can be considered as follows: if one ion experiences a light shift while another ion does not, its phase will be different. Put another way, the clocks that represent each ion will show different times. If the algorithm in question requires an entangling gate between these two ions, it will be impossible to choose a laser phase that is phase-synchronous with both ions. This highlights how each ion is its own oscillator and fully controlling them all clearly requires an

individual oscillator per ion unless light shifts are completely eliminated. In the setup described here, there are only two oscillators, but 5 ions.

The imbalance between the red and blue beams during an $\hat{X}\hat{X}$ gate occurs because the global beam is collimated through its AOM. Therefore, the global AOM is not imaged onto the ions and the red and blue beams are not guaranteed to overlap perfectly at the ion-plane. The resulting light shift is unavoidable as the overlap changes throughout the ion chain. On the other hand, the individual beams are focused through their AOM and a bichromatic rf pulse would be well-imaged at the ion-plane. This is ultimately the solution to the problem.

After data-collection for Refs. [67] and [82] was completed, a four-channel AWG³ was incorporated into the experimental apparatus. See Ref. [12] for complete details. With a total of 5 AWG's, each one could be directed onto an individual ion and the synthesized waveform was directed onto the global beam. In this way, the phases, frequencies, and amplitudes of each of the Raman beatnotes are now fully controlled. During this transition, we experimented with running the global beams at full power and reducing the power used in the individual beams, which had the expected effect of significantly lowering the light shifts present in the system during rotation gates as well as entangling gates. The remaining light shifts stemmed from the known efficiency mismatch in the 32-channel AOM at the frequencies relevant for the entangling gates. Despite the two beams being well-overlapped on the ions, the AOM efficiency caused a discrepancy between the intensity of the red and blue beams, causing light shifts during the two-qubit gates. To correct for this error, the

³Tabor Electronics Model: WX1284c; 1.25GS/s, four-channel Arbitrary Waveform Generator

phase of the entangling gate was extracted from the ions using analysis pulses. The experiment took the form of **Figure 3.7.2**.

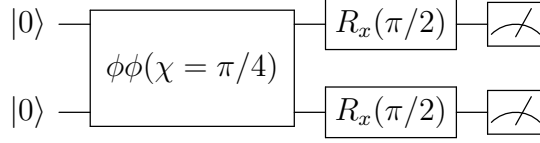


Figure 3.9: When performing an $\hat{X}\hat{X}$ interaction, the phase between the equally populated even parity states needs to be well-defined. This circuit writes that phase onto the parity of the output state.

The parity P of this measurement is the sum of the population in $|00\rangle$ and $|11\rangle$ minus the population in $|10\rangle$ and $|01\rangle$. The parity is related to the phase of the entangling interaction, ϕ , as $P = \sin(\phi)$. Different ratios of the amplitudes of the red and blue beams are tested until the parity is measured 0, indicating an $\hat{X}\hat{X}$ interaction. This method proved useful for daily calibration of the gates because it minimized the overall light shift accrued during the gate, including any residual shifts still present in the system. It would be better to minimize each light shift individually, but this was cumbersome if not impossible on our apparatus where the shifts are difficult to properly isolate. Better measurement and control of the light shifts would significantly improve our system. In the absence of a large light-shifts in the system, a similar experiment could be explored where the axis of the entangling gate is moved to the x-axis using phase advances. This is equivalent to **Figure 3.10**.

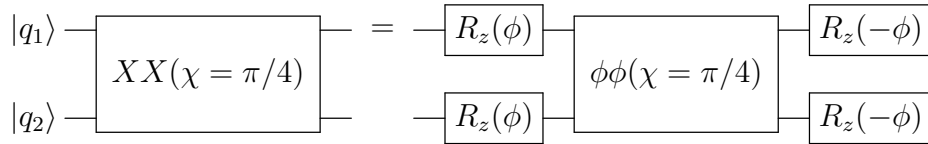


Figure 3.10: A simple technique for transforming the axis of any Ising interaction into an $\hat{X}\hat{X}$ gate.

Z-rotations at the beginning of experiments have no measurable effect since the ions are prepared in $|0\rangle$, a basis state of $\hat{\sigma}_z$. Therefore, one could effectively ignore the first two z-rotations in **Figure 3.10** if an experiment started with that circuit. One might incorrectly assume that they are not generally required. Instead, they are essential for correctly changing the qubit basis when employed in the middle of an arbitrary quantum algorithm where the qubits are unlikely to be in a z-basis state.

If each ion has its own oscillator, advancing or retarding the phase of an oscillator is akin to retarding or advancing the phase of the qubit. When the phase of the oscillator changes, so too does the phase of every subsequent operation. This is only available if the Rabi flopping interaction plane (x-y) is orthogonal to the measurement axis (z), which is true in the case of trapped ion qubits and likely most other quantum technologies. In this way, z-rotations can be performed by manipulating the phases of the rf signal with extremely high fidelity without manipulating the ions in any way. Any single-qubit gates can be decomposed into a combination of z-rotations and Rabi oscillations that minimizes the duration of the Rabi interaction.

3.8 Coherence

As mentioned above, the full picture of a QC's coherence time goes beyond the stability of its qubit's energy splitting and the lifetime of excited states. Creating amazing qubits certainly also requires the ability to control and manipulate the

qubits, as well. For ion trap qubits, this extends to the stability of the laser systems that affect Rabi flopping and the permanence of the trap parameters that are used for generating entanglement. In both cases, minimizing experimental noise using a feedback loop was required [83, 84].

A good way to test the coherence of a hyperfine-split qubit transition is to use microwave radiation. In our case, a microwave horn is placed many centimeters away from the ion trap outside the vacuum chamber. It can cause very high-fidelity Rabi oscillations across the whole chain of ions. There is no Debye-Waller decay term for the microwave fields since their wavelength is far too long to be in the Lamb-Dicke regime. There is also no beam pointing errors since the field is very stable in the far-field. In **Figure 3.11**, several Ramsey experiments are plotted including one performed with microwave radiation in blue. The Ramsey experiment here is simply a $\pi/2$ pulse, dead time, and then another $\pi/2$ pulse. It tests the coherence between the driver (microwave or laser) and the qubit splitting. The context of a Ramsey experiment is important, in this case we want to compare the Ramsey decay time with the time scales of typical experiments, which is ~ 3 ms. Clearly, no appreciable decay has occurred when driven with resonant microwave fields. This suggests a lower bound on the $1/e^2$ coherence time of ~ 40 ms. Next, the laser coherence will be considered.

3.8.1 Laser Coherence

The repetition rate (ω_{rep}) of the pulsed laser used for Raman transitions is primarily affected by its cavity. Like all laser systems, mode locked lasers begin with a cavity that defines a resonant condition that controls the phase and frequency of the out-coupled light. There is also some form of gain medium, in this case neodymium-doped vanadate crystals. What sets these lasers apart is the presence of a nonlinear saturable absorber, whose lossy qualities depend on the intensity of the incident light. Like a continuous wave laser, the gain medium in the cavity is being continuously pumped and the creation of the ultra-short pulses is solely due to the stability of the cavity and the saturable absorber. The noise on the repetition rate of our laser is specifically controlled by the cavity length, which is hermetically sealed and not generally accessible⁴. Any noise on the repetition rate translates to phase noise on the Raman beatnote that drives the qubits, so eliminating such noise is paramount for long, coherent experiments.

When the Raman beam leaves the laser housing, a small portion is immediately picked off and directed to an ultrafast photodiode⁵. The photodiode signal is sent through a band-pass filter to isolate the frequencies ± 250 MHz around the qubit splitting, which include the 108th combtooth of the frequency comb. Monitoring the drift of this combtooth is equivalent to monitoring $108 \times \omega_{rep}(t)$. The goal is to eventually write that drift onto an analog frequency modulation port of an rf

⁴Projects are underway to implement a high-frequency lock of the repetition rate on a Coherent Paladin with great initial success.

⁵ALPHALAS Ultrafast GaAs Schottky Photodetector Model: UPD-30-VSG-P

synthesizer, which will be sent to an AOM that controls the frequency of one of the Raman beams. Putting this synthesizer signal onto the global beam, we can write the equality:

$$2\pi \times 12.642 \text{ GHz} = \omega_{hf} = 108 \times \omega_{rep}(t) + \omega_{global}(t) - \omega_{individual} \quad (3.42)$$

Where $\omega_{global}(t)$ and $\omega_{individual}$ are the nominal frequencies we send to the respective AOM's. $\omega_{global}(t)$ oscillates around $2\pi \times 75$ MHz, which means $\omega_{individual}$ must be ~ 210 MHz. We implement the above equality by first mixing $108 \times \omega_{rep}(t)$ with an signal from an HP8672 synthesizer oscillating at the frequency $\omega_{hf} + \omega_{individual}$. The mixer produces a signal with the frequency $\omega_{hf} + \omega_{individual} - 108 \times \omega_{rep}(t) = 2\pi \times 75 + \epsilon(t)$ MHz $= \omega_{global}(t)$. Where $\epsilon(t)$ contains the noise from the repetition rate. Separately, we divide a 75 MHz signal from an HP8640 into two paths. One goes to the global AOM and the other is again sent to a mixer alongside ω_{global} such that $\epsilon(t)$ is extracted as a near-dc signal containing the necessary modulation of a 75 MHz signal to track the repetition rate drift. This signal is fed into the frequency modulation port of the HP8640 and the noise is thereby fed forward onto an AOM [83].

This approach was tested with a resonant Ramsey experiment, like the microwave experiment discussed above. In this case, the Raman beams are using the carrier transition to drive the necessary pulses. These data are shown in red in **Figure 3.11**.

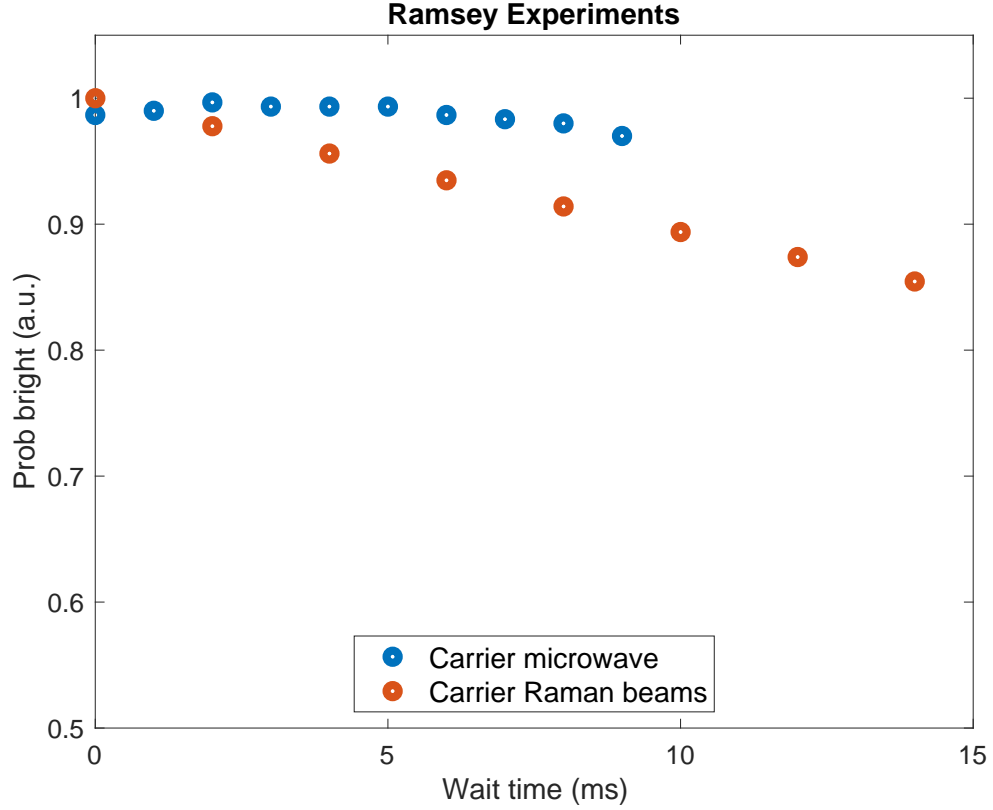


Figure 3.11: The coherence time of a $^{171}\text{Yb}^+$ qubit is presented in blue markers by performing a Ramsey experiment using stable microwave fields. The red markers indicate a similar experiment using Raman beams. The data taken with Raman beams samples the coherence time of the laser with respect to the qubit splitting. Clearly, there is some phase noise that is beginning to wash out the Raman coherence after ~ 10 ms. The $1/e^2$ coherence time is extrapolated to be ~ 40 ms. Parts of Raman coherence data were not properly saved, but records exist of the final points of the Ramsey scan at time 16 ms as well as strong evidence that there were no oscillations prior to this point. Therefore, we assume a $e^{-\beta t}$ decay and solve for artificial data points to fill in the gaps.

3.8.2 Phononic Coherence

The last type of coherence that will be mentioned is the coherence between the Raman beam and the phonon frequencies. The source of noise on the phonon frequencies stems from the fact that the rf voltage that drives the trap has a linear affect on the secular frequency of the ions, as seen in **Equation 2.9**. We require the secular frequencies of to be constant because we use them to generate entanglement, as explained above. Therefore, locking the rf voltage is a crucial task, which we perform using a rectifier circuit [84]. This circuit, depicted in **Figure 3.12**, converts the amplitude of the rf signal into a dc voltage, which we can use to make an error signal. The error signal is fed into a servo controller⁶, which controls a variable voltage attenuator that the rf signal goes through. Therefore, we have a nice feedback loop to lock the rf voltage. A photograph of the small, fabricated circuit is shown in **Figure 3.13**. Aside from using low temperature coefficient circuit components to build this rectifier circuit, we also added an additional diode to account for temperature shifts that effect the resistivity of the rectifying diode, highlighted in **Figure 3.13**. Both diodes sit in the same 1 mm² package, so any temperature fluctuations on the board will be very common between both diodes. We additionally covered the circuit with a thick layer of thermally conductive epoxy to help dissipate heat around the circuit to remove sudden temperature gradients.

The results of this locking mechanism are shown in **Figure 3.14**. The secular frequencies were measured nearly once a second for 80 minutes with and without the

⁶Newport LB1005-S, 10 MHz Bandwidth

lock. Clearly the locked rf voltage produces much more stable secular frequencies. The inset provides a more detailed look of the data, and significant noise is present on a ~ 1 Hz timescale. To give a sense of what happens at this timescale, it would cause the secular frequency to change between the calibration of an $\hat{X}\hat{X}$ gate and the subsequent experiment.

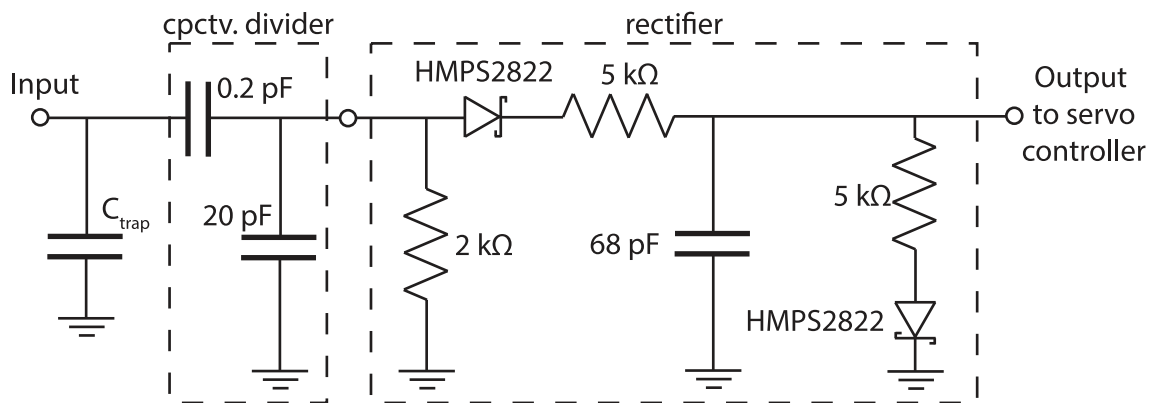


Figure 3.12: Circuit schematic for locking the rf voltage. The capacitive pickoff in the left dashed box is built onto the helical resonator.

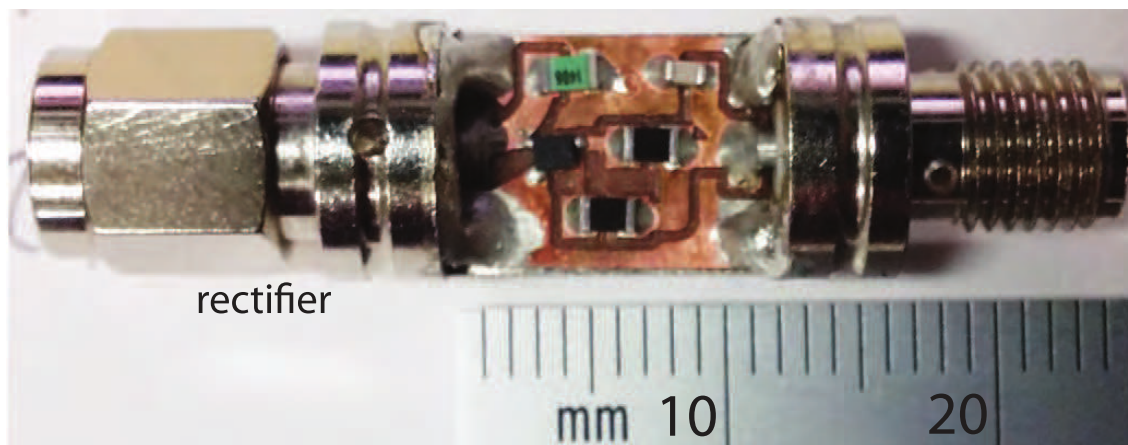


Figure 3.13: Photograph of the fabricated circuit board used for locking the rf voltage that creates the Paul trap. The small rectifying diode package is overlaid with a yellow rectangle.

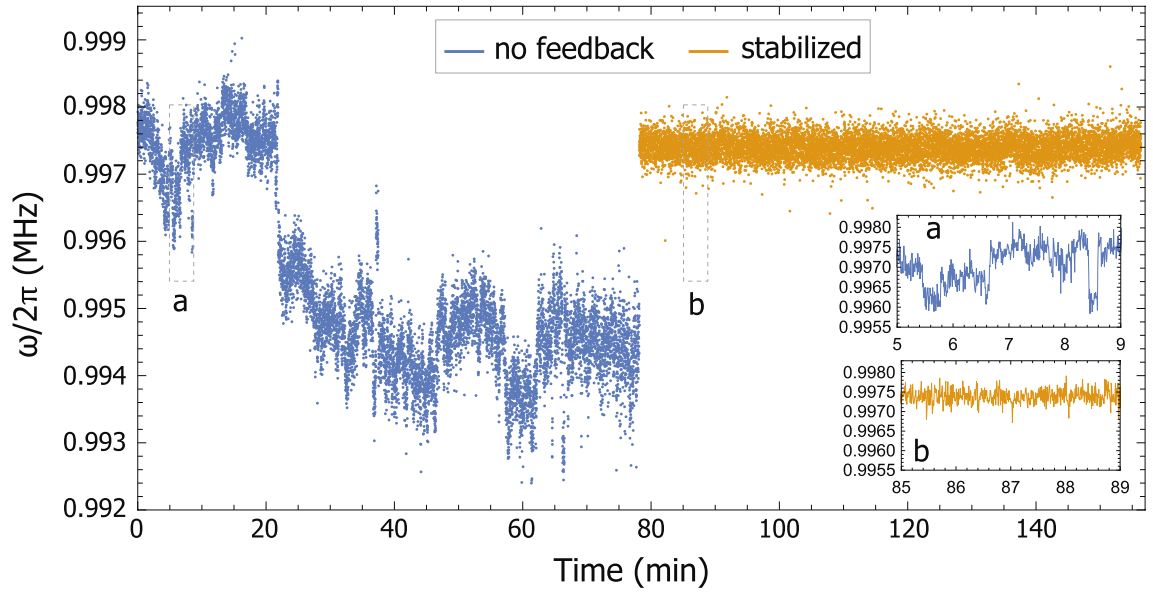


Figure 3.14: Measured values of the harmonic oscillator frequency as a function of time when the rf voltage source is either locked or unlocked. Clearly, the feedback loop significantly lowered the effect of slow noise. The inset shows time-magnified sections of the data during 4 minutes of data collection.

3.9 Experimental Entangling Gates

In order to perform entangling gates, the phonon spectrum must be measured by scanning the frequency of Raman lasers through resonance with the phonons, while keeping the amplitude and duration constant. The sensitivity of the scan depends on how power-broadened the transitions are, so the Raman light is often attenuated. Such a scan was performed with one ion by moving it into the focus of each Raman beam to sample the secular frequency at different points in the trap. In this way, the trap linearity is measured. An ideal, linear trap has the same secular frequency anywhere along its axis. On our experimental apparatus, the secular frequency has a dependency on position that appears to be linear within the limited range that it was tested, as plotted in **Figure 3.15**. In the plot, both radial modes are reported since both can be excited by the Raman beams. Due to this non-linearity, the confining term in the Lagrangian in **Equation 2.20** will be more complicated and each ion's participation in the modes of motion will deviate from the ideal case. The absolute values of the spectra can be measured experimentally using sideband spectroscopy as plotted in **Figure 3.16**. With 9 ions in the trap, this scan was performed on the middle 7 ions. In a linear trap, each ion will participate equally in the highest-energy mode, but ions 5, 6, and 7 show no excitation where ions 1, 2, and 3 have peaks around 3.053 MHz. This occurs because ions 5, 6, and 7 are more confined than the ions on the other end of the chain. In a similar fashion, none of the motional modes resemble their idealized forms.

For the purposes of building an ion-trap quantum computer, this non-linearity

is best considered a feature of this ion trap rather than a defect. The frequencies of Raman beams during an entangling gate are typically chosen to have a small detuning away from phonon modes that the relevant ions strongly participate in. Since many ions participate in most of the modes and our main use of the phonons is to generate entanglement, this spectrum is completely adequate for generating entanglement. Next, we will discuss how laser pulses are calculated for implementing those entangling gates using several different methods.

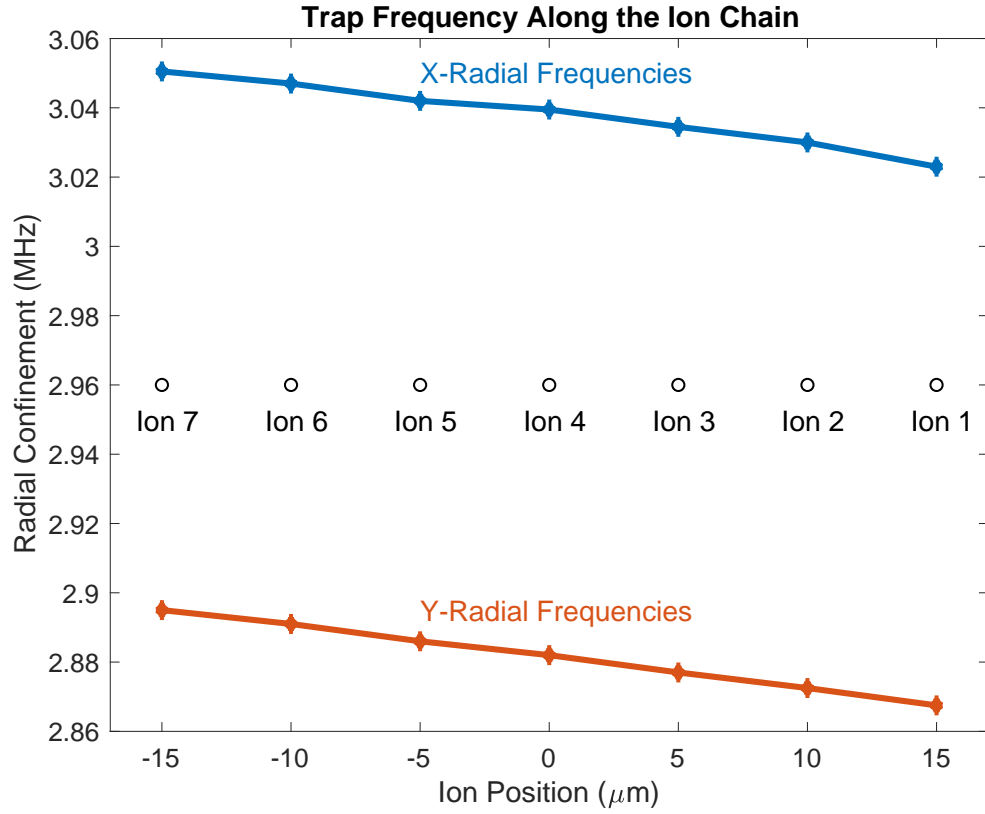


Figure 3.15: The secular frequency is measured at several points along the trap axis. Clearly, the trap has a linear dependence with position over this limited range. The experiment was performed by moving a single ion into the focus of the Raman beams and performing sideband spectroscopy. The ion positions are labeled. This non-linearity in the trap distorts the motional modes.

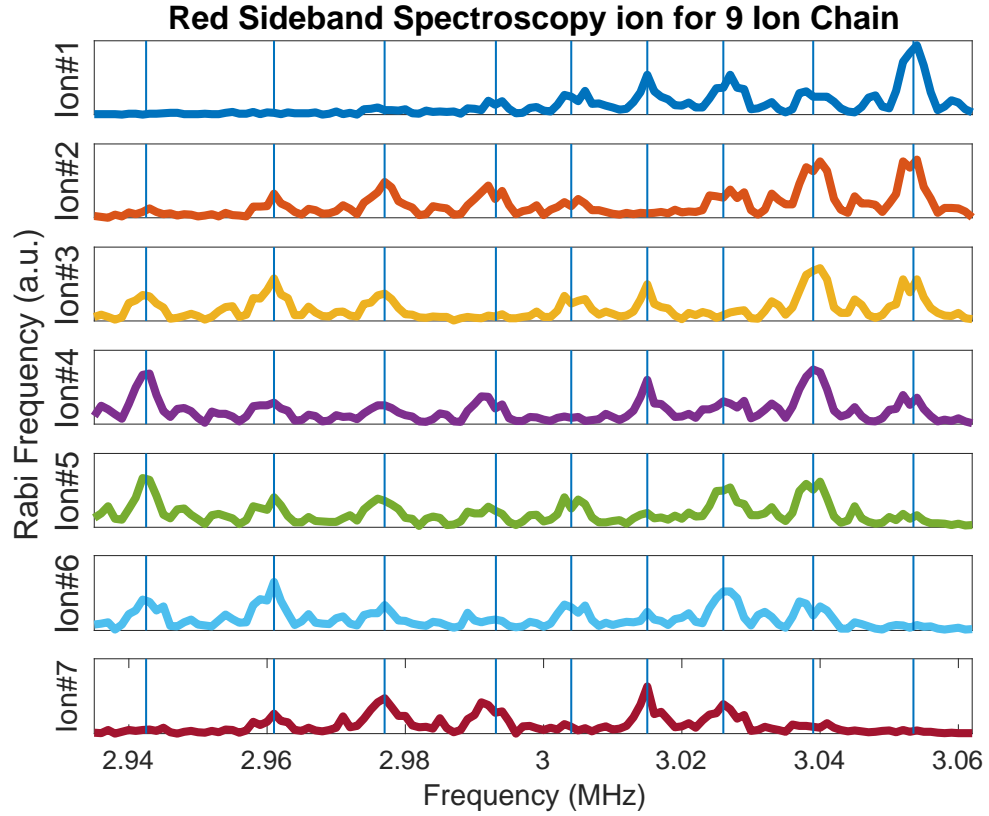


Figure 3.16: A constant amplitude and duration Raman beam focused over 7 ions within a 9-ion chain while its frequency is scanned. Every ion should participate in the highest frequency phonon mode, though half do not. This is caused by a non-linearity in the ion trap.

3.9.1 Two-Qubit Entanglement

The requirements for generating entanglement via the Ising interaction described in **Equation 3.35** are two-fold, though related. Both are described in greater detail where they are derived. First, any motional excitation that is leveraged to generate entanglement must be de-excited by the end of the operation. Any residual motional excitation directly translates to infidelity. Secondly, there must be enough motional excitation to enlarge a geometric phase that determines the amount of entanglement generated. The major goal when developing laser pulses is to accomplish these tasks with the highest fidelity, lowest required Rabi frequencies, and shortest times. Solving these sets of constraints is done in one of two regimes. The first regime is typically used on quantum simulators where global interactions are valued over local, pair-wise interactions. In this case, the detuning of the bichromatic excitation is large compared to both the phonon-mode splitting and the Rabi frequency. The motional excitations feature very tiny amplitudes before becoming de-excited. These small phononic excursions happen many times to generate significant entanglement. This approach is featured in Refs. [69, 72, 85]. These interactions are not calculated to de-excite motion, they rely on approximations that most modes are simply not excited. In contrast to this, many approaches have been developed that require individual addressing and create entanglement faster, with higher fidelity, and on a controlled subset of ions using some type of modulation [70, 86–88]. This modulation satisfies the constraints described in the beginning of this chapter. In the rest of the chapter, different approaches to generating entangling gates and their

implementation will be described.

Entangling gate fidelities will be measured using two observables. Firstly, a two-qubit gate applied to the state $|00\rangle$ should only transfer population into the $|11\rangle$ state. We can test this population transfer by creating a maximally entangled state with equal population in $|00\rangle$ and $|11\rangle$ and measure the likelihood of measuring an even parity state, P_{00+11} . This measures the diagonal components of the density matrix of the qubit state.

This leaves the off-diagonal components unmeasured, which contain half the information of the density matrix. To measure them, we transform the density matrix by rotational gates in such a way that the off-diagonal components can be measured via the oscillation amplitude of a parity scan [12, 54]. The average of the even parity population from the bare gate and this parity amplitude define the gate fidelity. We will rely on this definition for fidelity for the remainder of this discussion. The implementation of this fidelity measurement is lowered by the errors on the single-qubit operations during the parity scan, and no method is employed to correct for these errors. The ideal scheme would be to phase-synchronize the Raman beams with the synthesizer that generates the microwave signal, where the rotational gates would be minimal. Another scheme to improve this method is to take SPAM data using Raman pulses to prepare an ion in the bright state. After subtracting SPAM data taken with microwave pulses, the residual error could be considered to originate from the Raman pulses.

3.9.2 Amplitude Modulation (AM) Gates

The original approach for entangling ions in our laboratory is described in Refs. [54,70,89,90]. The Rabi frequency of the light is segmented in time, and we can write this set of Rabi frequencies as a vector, $\mathbf{\Omega}$. Next, the terms in **Equation 3.35** that depend on $\mathbf{\Omega}$ are written out as matrices. Since the spin-motion displacement term has a linear dependence on the Rabi frequencies in **Equation 3.37**:

$$\alpha_{i,k}(t) = \mathbf{C}_{i,k}\mathbf{\Omega} \quad (3.43)$$

while the spin-spin entangling term has a quadratic dependence in **Equation 3.38**:

$$\chi_{i,j}(t) = \mathbf{\Omega}^T \mathbf{D} \mathbf{\Omega} \quad (3.44)$$

Ultimately, a perfect gate will feature $\alpha \rightarrow 0$ and $\chi \rightarrow \pi/4$. To simplify the calculations, we want to express both conditions as having a similarly quadratic dependence. This is possible by considering the fidelity of the entangling gate \mathcal{F} as approximated as:

$$1 - \mathcal{F} \sim \frac{4}{5} \sum_{i,j,k} (|\alpha_{i,k}|^2 + |\alpha_{j,k}|^2) \beta_k = \mathbf{\Omega}^T \mathbf{B} \mathbf{\Omega} \quad (3.45)$$

where $\beta_k = \coth[\ln(1 + 1/\bar{n}_k)/2]$ is the inverse temperature of the k^{th} mode and \bar{n}_k is the average phonon number. With these two equations, a Lagrange multiplier

equation can be written to satisfy the constraints:

$$\Lambda(\Omega, \lambda) = \mathbf{\Omega}^T \mathbf{B} \mathbf{\Omega} - \lambda(\mathbf{\Omega}^T \mathbf{D} \mathbf{\Omega} - \pi/4) \quad (3.46)$$

Lastly, we note that all these matrices are Hermitian and symmetric, which allows us to write the following coupled set of equations:

$$\frac{\partial \Lambda}{\partial \Omega} = (\mathbf{B} + \mathbf{B}^T) \mathbf{\Omega} - \lambda(\mathbf{D} + \mathbf{D}^T) \mathbf{\Omega} = 0 \quad (3.47)$$

$$\frac{\partial \Lambda}{\partial \lambda} = \mathbf{\Omega}^T \mathbf{D} \mathbf{\Omega} - \frac{\pi}{4} = 0 \quad (3.48)$$

Where **Equation 3.47** is merely a generalized eigenvalue problem and its solutions will hold true when scaled together by a multiplicative constant. Therefore, **Equation 3.48** can be satisfied by scaling the pulse solution together. This eigenvalue problem can be solved efficiently in many programming environments. Typical solutions will be symmetric, as seen in **Figure 3.17**. A major benefit of this approach is the large number of solutions that it produces and can be tested on the experimental apparatus. Some solutions require more laser power than others and some do not properly de-excite motion at the gate's conclusions, so having a large swatch of solutions is experimentally very beneficial. It is not clear why many of the entangling gates fail, though we conjecture that it has to do with the inherent sensitivity of each gate to secular frequency noise and beam pointing noise. Since these dependencies are not optimized when the gate solutions are created, it is very plausible that the solutions have a wide range of sensitivities.

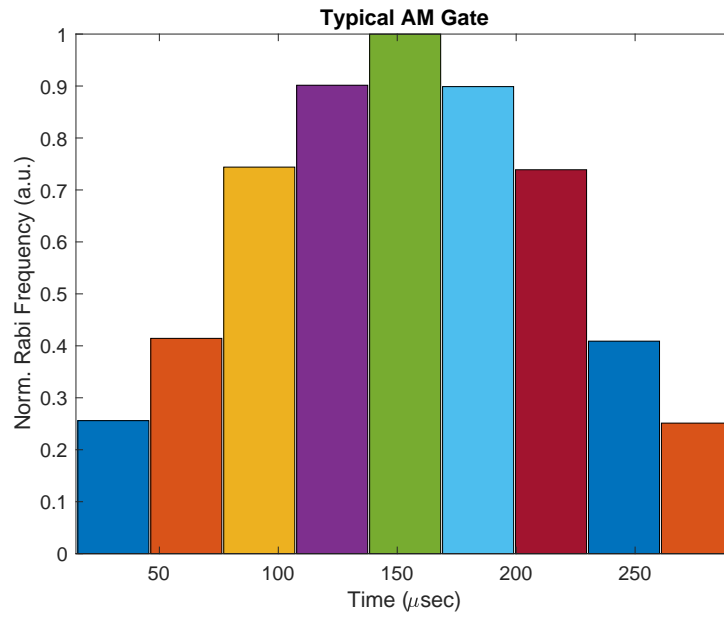


Figure 3.17: Amplitude is modulated over time to fulfill the conditions for performing an $\hat{X}\hat{X}$ gate between two ions. Here is an example of an amplitude profile that is used to entangle two ions. The detuning is fixed throughout the gate at 3.03 MHz from the carrier. The gate time is 257 μs .

This method is used to generate entangling gates for the algorithms described in Refs. [52, 67, 68, 71, 81, 82, 91, 92]. It is preferred over other methods because the Rabi frequencies required for generating maximal entanglement are lower than other methods explored.

The average fidelities of these gates were originally $\sim 98\%$ when Ref. [52] was published. By surrounding the entangling gate with single-qubit rotations a CNOT gate with a fidelity of $\sim 95\%$ could be generated. The CNOT fidelity encapsulates the two biggest issues surrounding the gates: entanglement fidelity and simultaneous dephasing due to light shifts.

As mentioned, the light shifts in the gate were improved by switching the phase-coherent, pulse-shaped rf onto the individual beams and by balancing the intensities of the red and blue beams during the $\hat{X}\hat{X}$ interaction. The beam alignment was also dramatically improved by adding two ions into the trap. In the end, the entangling gate fidelities and the CNOT fidelities both improved to $\sim 99\%$ on average. Along with single qubit rotation fidelities of $\sim 99.5\%$, these results are very promising for the future of ion-trap quantum computing.

3.9.3 Frequency Modulation (FM) Gates

By dithering the symmetric detuning of the Raman beams from the carrier frequency, the conditions for entangling ions can also be met. Compared to AM gates, the benefits and drawbacks of this approach are theoretically quite similar, though the AM gates have performed better on our apparatus. Unlike the AM

gate derivation described above, the FM approach begins with an initial guess and then uses an optimization protocol to perfect the gate by minimizing a set of cost functions. These cost functions are described below. Both methods have enough degrees of freedom to efficiently fulfill the requirements of the interaction and both could have a time-dependent light shift that depends on how the laser parameters are modulated. An argument can be made against unwanted Fourier components from the sharp amplitude changes in AM gates, though these frequencies will be significantly attenuated in an AOM due to its limited bandwidth and their effect is negligible. The FM approach requires a good initial guess to find a high-fidelity gate that does not require significant laser power, while the AM gates require no optimization. Therefore, comparing the two approaches depends heavily on the quality of the initial guess input into the FM gate solver. In the end, one could apply both methods where the output of an AM gate is used as the initial guess for the FM gates. Certainly, each approach has its merits and there is no reason why every degree of freedom should not be explored.

The cost functions are derived by first re-defining **Equation 3.37**, such that the time-dependent phase of the laser is $\theta'(t) = \int_0^t \delta(t')dt'$:

$$\alpha_{i,m} = \Omega_R/2 \int_0^\tau \exp[i\theta'_m(t')]dt' \quad (3.49)$$

with this new definition, we can explore suppressing this term to first order by

separating $\theta'(t)$ into a nominal detuning δ_1 and a detuning modulated in time $\theta(t)$:

$$\alpha_{i,m}(t) \sim \int_0^t \exp[i\theta_m(t') + i\delta_1 t'] dt' \quad (3.50)$$

Now, we can perform a power series expansion over $e^{i\delta_1 t}$ and ignore terms greater than $\mathcal{O}(\delta_1^2)$:

$$\alpha_{i,m}(t) \sim \int_0^t (1 + i\delta_1 t') \exp[i\theta_m(t')] dt' \quad (3.51)$$

Next, integration by parts results in the following:

$$\alpha_{i,m}(t) \sim i\delta_1 \int_0^t t' \exp[i\theta_m(t')] dt' \quad (3.52)$$

$$= i\delta_1 \left(\left[t \int_0^t \exp[i\theta_m(t')] dt' \right]_{t'=0}^{t'=t} - \int_0^t \int_0^{t'} \exp[i\theta_m(t'')] dt'' dt' \right) \quad (3.53)$$

$$= i\delta_1 (0 - t\alpha_{m,ave}) \quad (3.54)$$

where

$$\alpha_{m,ave} \sim \int_0^\tau \int_0^t e^{i\theta_k(t')} dt' dt = 0 \quad (3.55)$$

Using this derivation, the cost functions to be minimized are simply the real and imaginary elements of **Equation 3.49** as well as the optional cost function of **Equation 3.55**, which is considered an additional robustness condition. The solutions that consider this robustness condition should be insensitive to errors in the sideband frequencies. In the end, solutions were optimized with and without the robustness condition for comparison. See the supplemental material in Ref. [87] for more

details.

Robust and non-robust optimized gate solutions are presented in **Figure 3.18** alongside horizontal lines that denote sideband frequencies. The gates detuning is modulated through resonance with the phonon modes, which will strongly excite motion in the system. This was a surprising result of the optimization scheme that many of the physicists were skeptical of. Nevertheless, the results presented in **Figure 3.19** portray a 98.3(4)% fidelity gate, where the data is SPAM corrected and the uncertainties are statistical. This gate is among the best we can perform. The laser power required to maximally entangle two ions was $4\times$ larger than was predicted, which is an open question within this line of research.

The comparison between robust and non-robust gates is included in **Figure 3.20**. The horizontal axis denotes an error introduced in the measured sideband frequencies and the vertical axis portrays half the information of the fidelity measurements: the even parity population after running a single gate. Generally, the amount of entanglement generated was near maximal entanglement ($\sum_{i,j} \chi_{i,j} = \pi/4$). Generating small amounts of entanglement often has a higher fidelity than large amounts of entanglement because the phononic excitations are smaller, which could have skewed the results had we not ensured similar levels of entanglement. Clearly, the data from the robust gate has both a higher average fidelity and a broader range of high fidelities. On the other hand, the non-robust gate seemingly cannot withstand the noise present in the system to reach a comparable fidelity without introduced errors.

This project began after our lab had been implementing AM gates for several

years. Therefore, a comparison between the two approaches is somewhat difficult. Nevertheless, the major result of this project was the amazing robustness achieved. Compared to the AM gates, the fidelities were not significantly improved and the Rabi frequencies required were much larger, but the robustness is very impressive. Future work might be to combine the two approaches by using the AM gate as the initial guess for the FM gate.

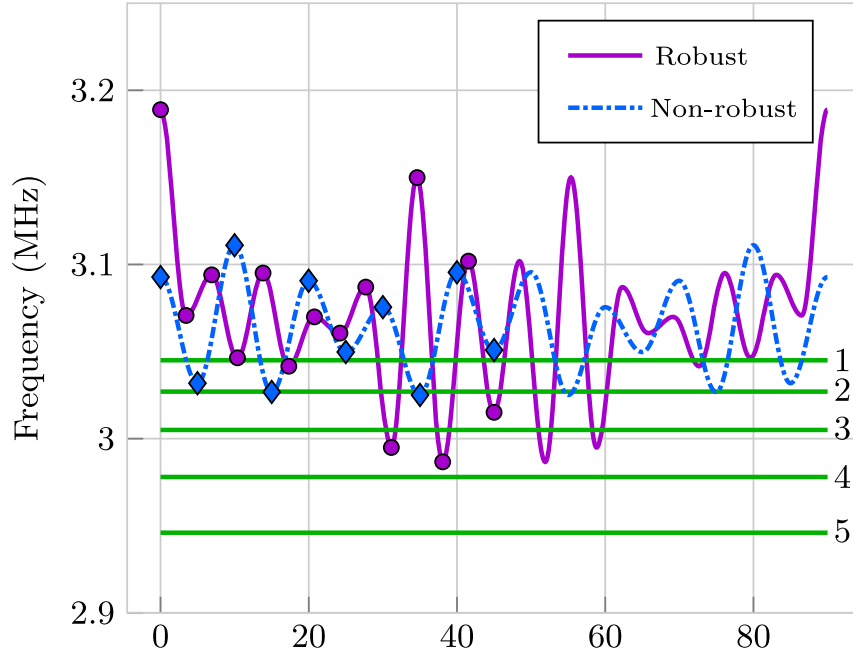


Figure 3.18: The shape of the frequency modulation used to perform an entangling gate between two ions. Two gates are super-imposed onto this graph: one denoting the shape of a robust gate and one for a non-robust gate. This distinction is explained in greater detail in the text. The horizontal lines denote sideband frequencies.

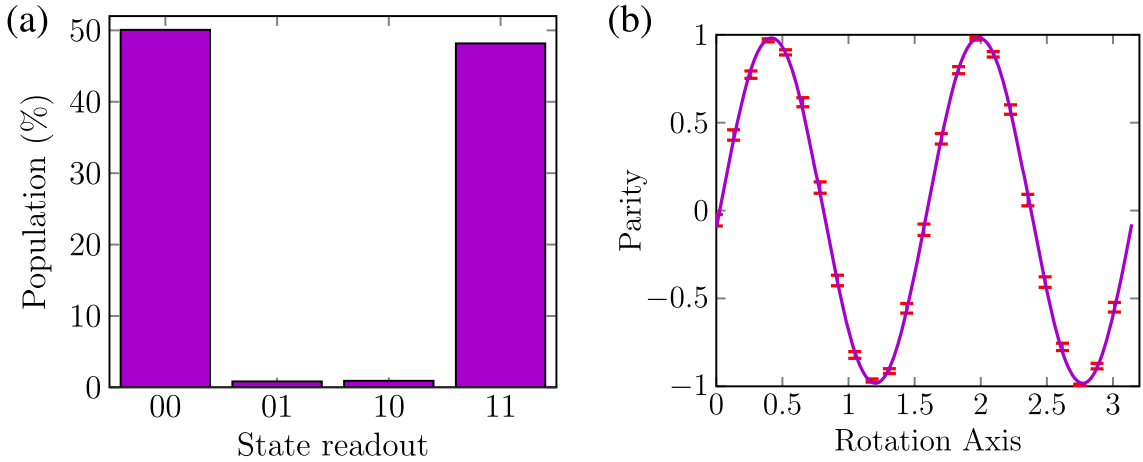


Figure 3.19: The gate described in **Figure 3.18** was performed on two ions and the fidelity measurements of the gate is presented here. a) Shows the population data during a maximally entangling gate. b) Presents a parity scan performed on the gate. The error bars, though small at places, are statistical and all the data is SPAM corrected.

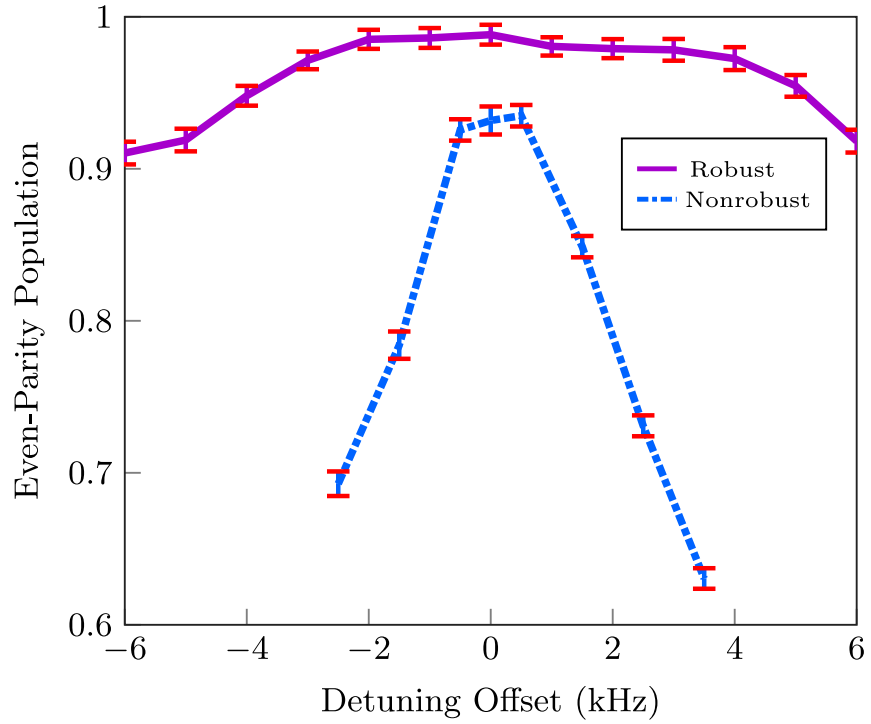


Figure 3.20: The robustness of the FM gates was tested by introducing an error to the nominal symmetric detuning of the gate. Clearly, the "robust" gate performs well over the large range of the detuning error. The vertical axis in this plot is not fidelity, rather even-parity population after running the gate. In some sense, it is half of the parity information. The error bars are statistical and all the data is SPAM corrected.

3.10 Gates on Longer Chains

Lastly, a gate was performed on a chain of 17 ions using a method similar to the frequency modulation described above [88]. The 17-ion chain is the longest chain used in an experiment on our apparatus. With 17 ions in the trap, the motional spectra is far more complicated and we wanted to see how entanglement might work with this many ions. Complete individual addressing and detection were sacrificed to perform these experiments: only 5 ions were well-aligned on Raman beams and PMT channels. In some sense, this setup was still a 5-qubit experiment despite the presence of 17 ions in the trap. Therefore, the goals of this setup were simply to perform entangling gates and witness the scalability of our system for generating entanglement on 17-ion chains.

dc voltages were found to ensure that the middle 9 ions had a $\sim 2.5\mu\text{m}$ spacing. Therefore, every other ion within this middle portion of the crystal was well-imaged onto our AOM and PMT arrays. The alignment was very tricky at this ion-spacing because it exacerbated both imaging and addressing crosstalk. Therefore, we used the positions of the middle 5 ions of a 7-ion chain as seen on a camera to mark where the Raman beams were tightly focused. Next, voltage solutions were found that placed ion numbers $\{5, 7, 9, 11, 13\}$ at those same locations. Though addressing crosstalk was worsened with such close ion-spacing, we never intended on addressing the other ions on the trap, so much of that additional crosstalk is a higher order effect that can be ignored. A similar argument could be made for imaging crosstalk. Therefore, this 17-ion system would not make a great 5-qubit quantum computer

due to poor crosstalk parameters, but is very suitable for the focused experimental purposes of just performing entangling gates.

An effort was made to attempt running the entangling gates without full knowledge of the motional spectra. So only the frequencies of the six most energetic phonon modes were measured by sideband spectroscopy, as depicted in **Figure 3.21**. Most of the ions participate quite equally in the highest-energy phonon mode, suggesting a more idealized phonon spectra. Similarly, the second highest-energy mode seems to “tilt” around the middle ion. Seemingly, the effects of the trap non-linearity are minimized in the middle of this long chain. these tightly-spaced ions, the Coulomb interaction dominates the axial potential more than the dc confinement.

The motivation for measuring only some of the phonon frequencies comes from imagining a future quantum computer with a very large number of ions and an incredibly dense motional spectra. Measuring all of the phonons would be cumbersome, but looking at a limited set of phonons over a small range within the spectra could provide enough information for the entangling operations. With this intuition, we calculated the pulses depicted in **Figure 3.22a** and corresponding representations of α_m in the complex plane **3.22b**. The phonon excitation is depicted in order of energy, and clearly those with the large detunings from the nominal gate frequency have very little excitation. Certainly, the unmeasured phonons with even larger detunings will also not be excited.

The gates were performed on ion pairs $\{5, 13\}$ and $\{9, 7\}$ with respective fidelities of 97(1)% and 95(1)%, as seen in **Figure 3.24**. These reported numbers are

SPAM corrected and the uncertainties are statistical. With the caveat that alignment was slightly worse in this setup, these relatively high fidelities suggest that the entangling operation is not worsened by the large number of ions in the trap.

Many entangling gate solutions were calculated and experimentally performed with a variety of nominal detunings from the modes. The initial attempts all had a small detuning from the phonon modes before a final gate was developed with a larger detuning. Here, data is included from a gate with a nominal detuning of 5 KHz in **Figure 3.23** and a detuning of 11 KHz in **Figure 3.24**. The gate with the small detuning had a fidelity of 90(1)%, while the gate with the large detuning had an average fidelity of 96(1)%. This discrepancy likely stems from the instability of the phonon frequencies and the robustness of the gate design.

The transverse mode frequencies slowly change by ± 0.5 KHz on time scales of many seconds. Since the gates are robust, this detuning noise will *not* cause residual phonon excitation at the end of the gate. On the other hand, this drift is causing the detuning to change by $\sim 20\%$ for the small-detuning gates as often as every few hundred experimental repetitions. As the detuning changes, so too does the amount of entanglement generated because $\sum \chi_{i,j}$ has a quadratic dependence on the detuning as [59]:

$$\sum_{i,j}^N \chi_{i,j} = \frac{\pi |\Omega(t) x_0|^2}{2(\hbar\delta)^2} \quad (3.56)$$

Therefore, this noise causes an under/over-rotation error on the gate. This error does not appear in the population data because it is averaged out. On the other hand, a high-amplitude parity scan occurs when $\chi_{i,j} = \pi/4$ and any deviation

from that value will lower the amplitude of the oscillation. Therefore, under/over rotations will not be averaged out, so we see the noise of this phonon frequency written directly onto the parity scan. Therefore, by doubling the detuning, the error discrepancy between the population data and the parity scan was minimized by a factor of 4, as expected.

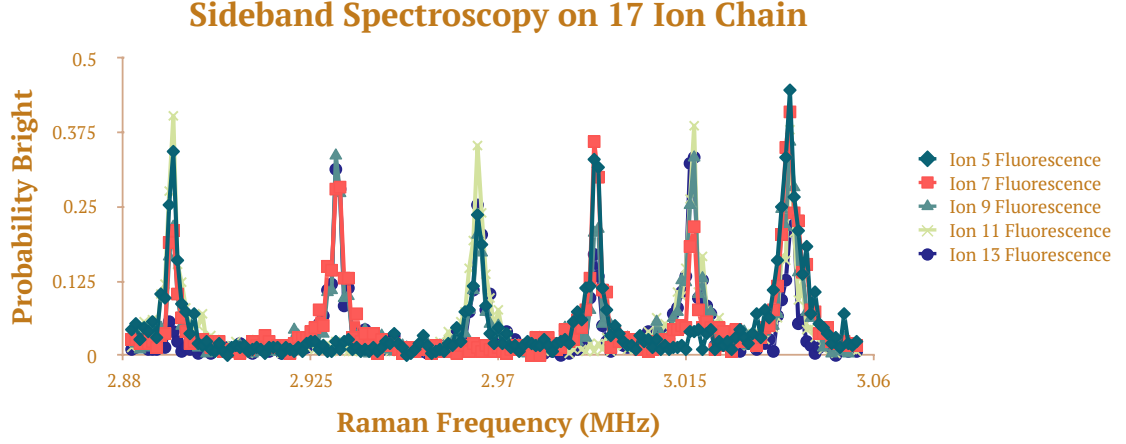


Figure 3.21: Sideband spectroscopy is performed by shining Raman beams of a given duration and intensity onto the ions and then scanning the frequency of the beams through resonance with the motional spectra.

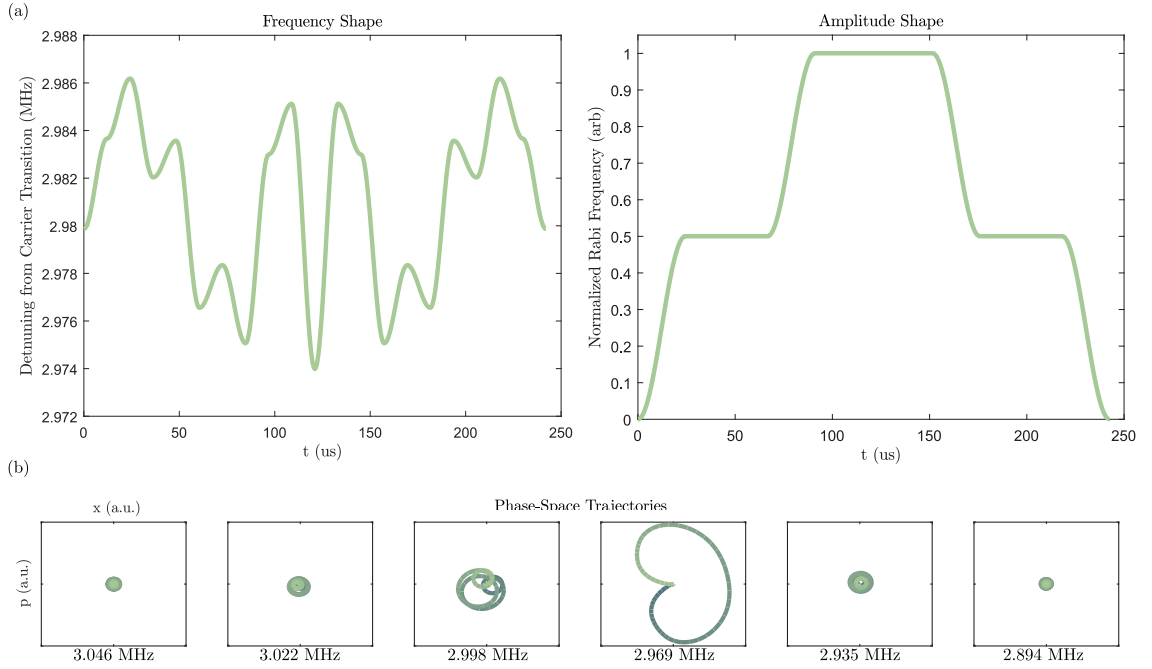


Figure 3.22: The amplitude and frequency modulation for performing a two-qubit gate in the presence of a 17-ion chain is depicted in (a). The modulation that fulfills the constraints of the $\hat{X}\hat{X}$ interaction are performed by dithering the frequency, not the amplitude. b) Graphic depictions of the phononic trajectories through the complex plane during the gate. Infidelity of the gate is related to the phonons closing the loop in the complex plane at the end of the gate. The entanglement generated is related to the area enclosed by this trajectory.

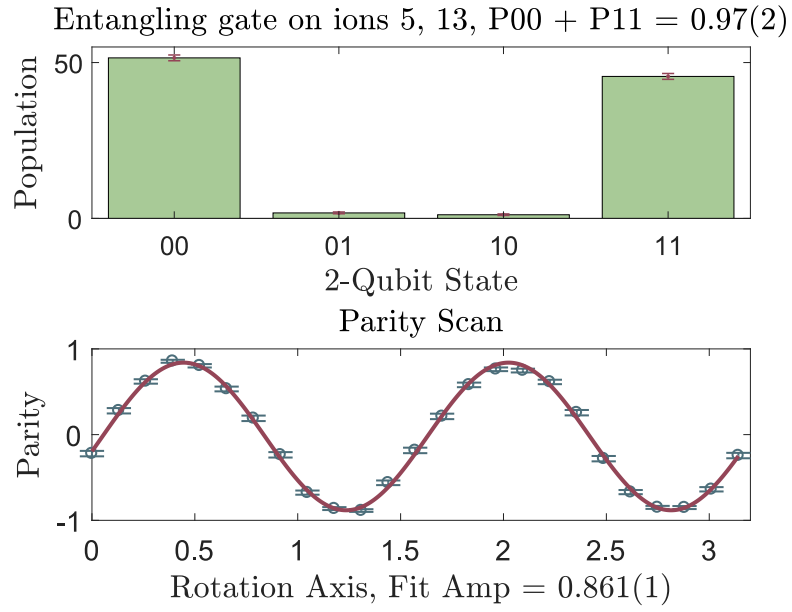


Figure 3.23: An example of a small-detuning, low-fidelity gate performed on a 17 ion chain. Despite one half of the fidelity experiments looking favorable, the second half looks mediocre. The cause of this discrepancy is instability of the phonon frequencies which make different amounts of entanglement during the gate. This noise is averaged out when measuring the bare gate, but not when performing a parity scan.

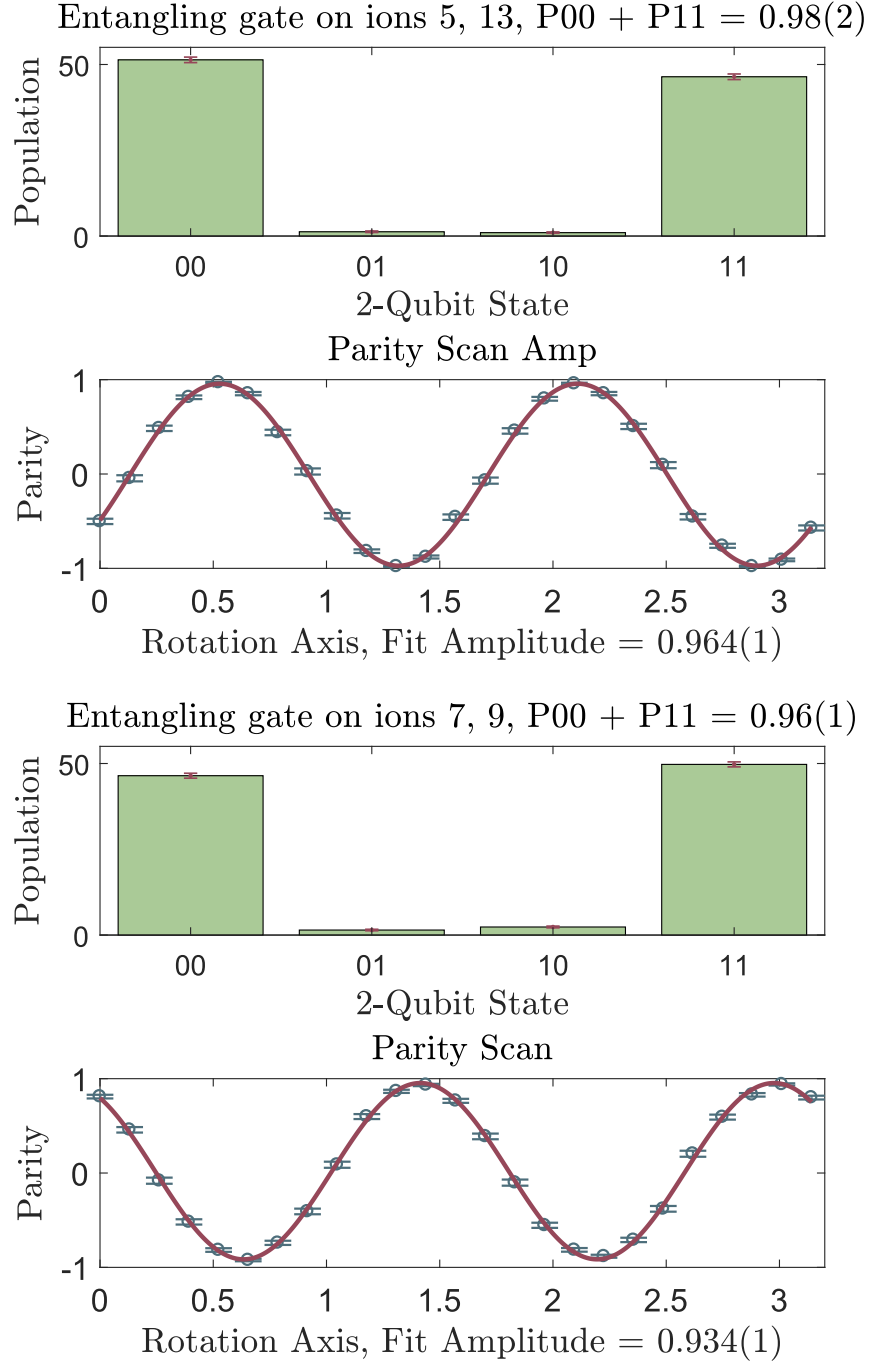


Figure 3.24: A large-detuning, high-fidelity gate performed on a 17 ion chain using two distinct pairs of ions. Both the population test and the parity test report a high fidelity.

Part II

Applications

Chapter 4: Quantum Scrambling

4.1 Background

We should begin our discussion of quantum scrambling by reminding ourselves that information locality is yet another element of classical physics that is obscured by quantum physics. In quantum physics, a piece of information can be described locally, for example a single qubit in a known state or an operator acting on a single qubit. This is similar to classical information that is stored in a known location. In contrast to this phenomenon, quantum information can also be non-local if a qubit is in an entangled state. Here, the information is not stored on either qubit, rather it is stored in the entangled correlations between the qubits.

Scrambling is closely related to entanglement. When a qubit is scrambled its properties are spread throughout a system and the information contained in the state or operator now exists in a delocalized form. What distinguishes scrambling from entanglement is that entanglement happens over a qubit axis while scrambling will happen over all axes. For example, our native entangling gates with trapped ions ultimately perform a $\hat{\sigma}_\phi^i \hat{\sigma}_\phi^j$ interaction on the two qubits. This interaction entangles qubits along the ϕ -axis. Were the qubits prepared along the ϕ -axis prior

to the gate, no entanglement would be generated. With a scrambling unitary, qubits prepared along any axis will become scrambled. Put another way, the eigenstates of an entangling operator are states prepared along the same axis as the entangling gate.

Interestingly, there exists an astonishing hypothesis that argues that none other than black holes are nature's fastest quantum scramblers. Anti-de Sitter/conformal field theory correspondence (AdS/CFT) attempts to answer the famous black hole information paradox by arguing that information thrown in to a black hole will not thermalize, rather it will become entangled, via quantum scrambling, with the entire black hole as well as Hawking radiated photons that may already be far away from the black hole. Accordingly, black holes are essentially processors of quantum information. This theory is still debated by high-energy physicists and I am only attempting to summarize the debate.

This brings us to a thought experiment that begins with the assumption that black holes coherently scramble quantum information. If a qubit tossed into a black hole can be quickly teleported if an observer has a quantum memory entangled with the black hole [93]. In this way, black holes are so-called quantum mirrors that reflect quantum information. This thought experiment is the inspiration behind our experiment, which looks at how quantum scrambling is performed and measured experimentally.

As with entanglement, scrambled information is stored in both diagonal and off-diagonal terms of a density matrix. We can use the Bell basis states as an

illuminating example.

$$\begin{aligned}
|\Psi^+\rangle &= \frac{1}{\sqrt{2}}(|00\rangle + |11\rangle), |\Psi^+\rangle\langle\Psi^+| = 0.5 \begin{bmatrix} 1 & 0 & 0 & 1 \\ 0 & 0 & 0 & 0 \\ 0 & 0 & 0 & 0 \\ 1 & 0 & 0 & 1 \end{bmatrix} \\
|\Psi^-\rangle &= \frac{1}{\sqrt{2}}(|00\rangle - |11\rangle), |\Psi^-\rangle\langle\Psi^-| = 0.5 \begin{bmatrix} 1 & 0 & 0 & -1 \\ 0 & 0 & 0 & 0 \\ 0 & 0 & 0 & 0 \\ -1 & 0 & 0 & 1 \end{bmatrix} \\
|\Phi^+\rangle &= \frac{1}{\sqrt{2}}(|01\rangle + |10\rangle), |\Phi^+\rangle\langle\Phi^+| = 0.5 \begin{bmatrix} 0 & 0 & 0 & 0 \\ 0 & 1 & 1 & 0 \\ 0 & 1 & 1 & 0 \\ 0 & 0 & 0 & 0 \end{bmatrix} \\
|\Phi^-\rangle &= \frac{1}{\sqrt{2}}(|01\rangle - |10\rangle), |\Phi^-\rangle\langle\Phi^-| = 0.5 \begin{bmatrix} 0 & 0 & 0 & 0 \\ 0 & 1 & -1 & 0 \\ 0 & -1 & 1 & 0 \\ 0 & 0 & 0 & 0 \end{bmatrix}
\end{aligned} \tag{4.1}$$

Famously, the Bell basis is a complete orthogonal basis of entangled states. In this basis, we cannot simply measure qubits in any single basis precisely because the information is not local to either qubit. Furthermore, if we simply measure the qubits as they are, we will not be able to distinguish $|\Psi^+\rangle$ from $|\Psi^-\rangle$. Instead, we need to disentangle our qubits and simultaneously map the bit and coherence information onto a single-qubit basis. This is often done with the following circuit and mapping:

$$\begin{array}{c}
|q_1\rangle \text{ --- } \bullet \text{ --- } \boxed{H} \text{ ---} \\
|q_2\rangle \text{ --- } \oplus \text{ ---}
\end{array} \tag{4.2}$$

$$\begin{aligned}
|\Psi^+\rangle &\rightarrow |00\rangle \\
|\Psi^-\rangle &\rightarrow |10\rangle \\
|\Phi^+\rangle &\rightarrow |01\rangle \\
|\Phi^-\rangle &\rightarrow |11\rangle
\end{aligned}
\tag{4.3}$$

The circuit in 4.3 moves the information stored in diagonal and off-diagonal matrix elements of a density matrix to measurable quantities. Thoughtfully designing protocols like this highlights a nuance of working with non-local information which will foreshadow our work with scrambled information. If the qubits are entangled along some unknown axis, then efficiently measuring them can be even more difficult and may require expensive measurement techniques like state tomography. As we begin to think about measuring scrambled many-body states, the prospect of efficient measurement becomes worse. Therefore, we want a method that can measure quantum scrambling without tomography and without *a priori* knowing phases of the scrambled states.

4.2 Measuring Scrambling

Now that we have a better understanding of the distinction between local and non-local quantum information, we can begin a deeper discussion of quantum scrambling by thinking about information stored in operations instead of qubits: the Heisenberg representation of quantum mechanics. Here, local information takes the

form of a single-qubit operator while non-local information is a many-qubit operator.

One can scramble local information as follows:

$$\hat{U}_{scramble}(\hat{A} \otimes \hat{I} \otimes \hat{I} \otimes \dots) \hat{U}_{scramble}^\dagger \xrightarrow{scramble} \hat{B} \otimes \hat{C} \otimes \hat{D} \otimes \dots \quad (4.4)$$

Where \hat{A} , \hat{B} , \hat{C} , and \hat{D} are single-body operators, \hat{I} is the identity operator, and \hat{U} is a scrambling operator.

The common tool for measuring scrambling is the out-of-time-order correlation function (OTOC) of the form:

$$OTOC = \langle \hat{O}_A^\dagger \hat{O}_D^\dagger(t) \hat{O}_A \hat{O}_D(t) \rangle, \quad (4.5)$$

where \hat{O}_A and \hat{O}_D are initially unitary, commuting operators acting on separate subsystems A and D . Of course, all operators acting on separate systems will commute. We evolve \hat{O}_D according to $\hat{O}_D(t) = \hat{U}^\dagger \hat{O}_D \hat{U}$, where \hat{U} is the unitary time-evolution operator of the system, $\hat{U} = e^{-i\hat{H}t/\hbar}$. In an ideal implementation, time-evolution that scrambles will cause $\hat{O}_D(t)$ to increasingly act on the entire N-qubit system, including subsystems A and D . As $\hat{O}_D(t)$ spreads onto subsystem A , $\hat{O}_D(t)$ and \hat{O}_A will commute less, and the OTOC will decay according to $Re[OTOC] = \frac{1}{2}(\langle ||[\hat{O}_A, \hat{O}_D(t)]||^2 \rangle - 1)$ [94]. In circuit form, the quantum circuit for this experiment

would appear as:

Quantum circuit diagram (4.6) showing the evolution of operators O_A and O_D through a sequence of unitaries U and U^\dagger on three qubits $|q_1\rangle$, $|q_2\rangle$, and $|q_3\rangle$. The circuit consists of four stages of U and U^\dagger blocks. O_A is applied to $|q_1\rangle$ at the first stage, and O_D is applied to $|q_3\rangle$ at the second stage. The final operators are O_A^\dagger on $|q_1\rangle$ and O_D^\dagger on $|q_3\rangle$.

$$(4.6)$$

Assuming our scrambling operator specifically scrambles single-body Pauli operators into many-body Pauli operators, we can write the evolution of $\hat{O}_D(t)$ as:

Diagram (4.7) showing the evolution of a single-body operator O_D into many-body operators O_D^1 , O_D^2 , and O_D^3 . The circuit shows a unitary U acting on three qubits, followed by O_D on the third qubit, and then U^\dagger . The result is three separate operators O_D^1 , O_D^2 , and O_D^3 on the three qubits respectively.

$$(4.7)$$

Now, we can rewrite circuit 4.6 as:

Diagram (4.8) showing the rewritten circuit (4.6) as a sequence of operator evolutions. The circuit is equivalent to a sequence of operators O_A , O_D^1 , O_A^\dagger , and $O_D^{1\dagger}$ on $|q_1\rangle$, and O_D^2 and $O_D^{2\dagger}$ on $|q_2\rangle$, and O_D^3 and $O_D^{3\dagger}$ on $|q_3\rangle$.

$$(4.8)$$

At this point, we can see quite clearly that our correlation measurement will decay if \hat{O}_A and \hat{O}_D^1 fail to commute by measuring qubit 1 at a minimum. A error-free OTOC will decay from 1 as scrambling is increased.

This approach to measuring OTOCs has important experimental problems because errors on our scrambling unitaries will propagate onto the correlation measurement, causing the OTOC to undergo a false decay. Therefore, measuring what seems to be a non-trivial OTOC is not enough to measure the presence of scram-

bling. For example, if \hat{U} decoheres the three-qubit system, then all of the \hat{O}_D^i terms in **Figure 4.8** can be considered decohering channels. Certainly, \hat{O}_A and \hat{O}_D^1 will not commute because \hat{O}_D^1 is not a unitary operator. Therefore, the OTOC will decay despite no scrambling being performed, rather because the dynamics are dominated by errors. In a similar way, if the three-qubit operators in **Figure 4.8** are not \hat{U} and \hat{U}^\dagger , then the OTOC will also decay.

These arguments are well understood. The state-of-the-art measurement of quantum scrambling using over one hundred ions is presented in Ref. [35]. In that paper, lengthy and thorough analyses of relevant experimental errors are included and theoretical models were generated to understand and quantify experimental errors. By doing so, the authors significantly strengthen their claims of measuring quantum scrambling using an OTOC. The scrambling was performed using an pairwise Ising interaction, which is notably different from the circuit-based scrambling operator that will be discussed.

In response to the issues that plague OTOC measurements, we performed an experiment that uses two observables to separately measure scrambling and an OTOC, described in Ref. [68], thereby verifying the OTOC measurement without significant error analysis or state tomography. To understand the derivation from **Figure 4.6** to the circuit we will eventually run, it is useful to introduce the following quantum circuit shorthand and identity:

$$\boxed{} = \frac{1}{\sqrt{2}}(|00\rangle + |11\rangle) \quad (4.9)$$

$$\begin{array}{c} \text{---} \\ | \\ \boxed{U} \\ | \\ \text{---} \end{array} = \begin{array}{c} \text{---} \\ | \\ \boxed{U^T} \\ | \\ \text{---} \end{array} \quad (4.10)$$

Using these two circuits and without any loss of generality, we can re-write circuit 4.6 as:

$$\begin{array}{c} \text{---} \\ | \\ \boxed{O_A} \\ | \\ \text{---} \end{array} \begin{array}{c} \text{---} \\ | \\ \boxed{U} \\ | \\ \text{---} \end{array} \begin{array}{c} \text{---} \\ | \\ \boxed{U^\dagger} \\ | \\ \text{---} \end{array} \begin{array}{c} \text{---} \\ | \\ \boxed{O_A^\dagger} \\ | \\ \text{---} \end{array} \\
 \begin{array}{c} \text{---} \\ | \\ \text{---} \end{array} \begin{array}{c} \text{---} \\ | \\ \boxed{O_D} \\ | \\ \text{---} \end{array} \begin{array}{c} \text{---} \\ | \\ \boxed{U^\dagger} \\ | \\ \text{---} \end{array} \\
 \begin{array}{c} \text{---} \\ | \\ \text{---} \end{array} \begin{array}{c} \text{---} \\ | \\ \boxed{O_D^*} \\ | \\ \text{---} \end{array} \begin{array}{c} \text{---} \\ | \\ \boxed{U^T} \\ | \\ \text{---} \end{array} \\
 \begin{array}{c} \text{---} \\ | \\ \text{---} \end{array} \begin{array}{c} \text{---} \\ | \\ \boxed{U^*} \\ | \\ \text{---} \end{array} \begin{array}{c} \text{---} \\ | \\ \text{---} \end{array} \quad (4.11)$$

Already, it is clear that the qubit register has doubled in size. As described in Ref. [95, 96], we can make modifications to this circuit that would significantly simplify the experimental sequence. This new circuit will have the ability to measure scrambling and an OTOC, as promised above, and is depicted in **Figure 4.1**.

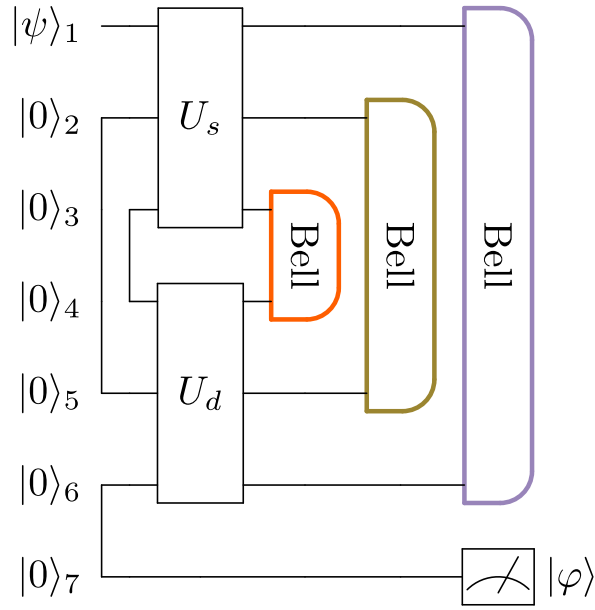


Figure 4.1: A quantum circuit for measuring quantum scrambling using a teleportation protocol. Only one of the Bell measurements are performed for each implementation of the circuit. If \hat{U}_s and \hat{U}_d are both ideal scrambling unitaries, then the Bell measurement can herald the teleportation of $|\psi\rangle$ to qubit 7 and $|\langle\psi|\varphi\rangle|^2 = 1$. More details are included in the text.

4.3 Two Simultaneous Measurements

The quantum circuit we use to measure scrambling and OTOCs can be seen in **Figure 4.1** and the sequence can be summarized as follows:

- I: Begin the sequence by preparing the first qubit in a known state $|\psi\rangle$.
- II: Put qubit pairs $\{3, 4\}$, $\{2, 5\}$, and $\{6, 7\}$ in the Bell state $|\Psi^+\rangle$ (see **Equation 4.1**).
- III: Apply an operator \hat{U}_s on qubits $\{1, 2, 3\}$ and another operator \hat{U}_d on qubits $\{6, 5, 4\}$. Note that the qubit ordering for \hat{U}_d is backwards from what we typically use.
- IV: Perform **only one** of the displayed Bell measurements on qubit pairs $\{3, 4\}$, $\{2, 5\}$, or $\{1, 6\}$.
- V: Measure qubit 7 in whatever basis qubit 1 was prepared in.

Each step in this recipe has important ramifications that we will now consider. Since we need to establish that our scrambling unitary can scramble quantum information in any basis, we use step 1 to prepare eigenstates of all the Pauli operators and step 7 to read them out. Additionally, we will measure two qubits in the Bell basis in step 4 to herald teleportation using the circuit depicted in **Figure 4.3**. where α is the sign of the phase in the Ising interaction. Measuring in the Bell basis is equivalent

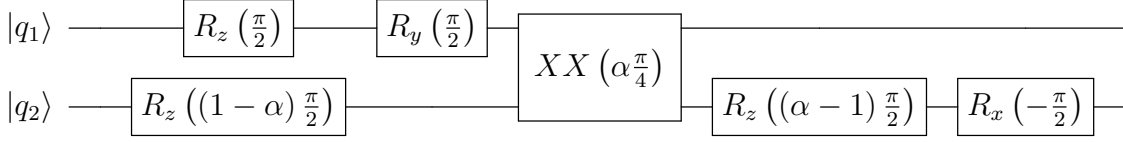


Figure 4.2: Quantum circuit for measuring qubits in the Bell basis.

to averaging over measurement Pauli bases according to:

$$|\Psi^+\rangle\langle\Psi^+| = \frac{1}{4}(\hat{\sigma}_I \otimes \hat{\sigma}_I^* + \hat{\sigma}_X \otimes \hat{\sigma}_X^* + \hat{\sigma}_Y \otimes \hat{\sigma}_Y^* + \hat{\sigma}_Z \otimes \hat{\sigma}_Z^*) \quad (4.12)$$

Therefore, we have two distinct types of averages. One which increases the number of experiments we need to run and one that is implicit in the Bell measurement. Both are necessary because the OTOC that we will be able to measure has both of these features built-in. It takes the form:

$$OTOC_{average} = \sum_{\phi, \hat{O}_p} \left\langle \hat{O}_1^\dagger \hat{O}_p^\dagger(t) \hat{O}_1 \hat{O}_p(t) \right\rangle, \quad (4.13)$$

where $\hat{O}_1 \equiv |\psi\rangle\langle\phi|$ corresponds to averaging over different states for qubit 1 (as done in [sequence 4.3.1](#)). $\phi, \sum_{\phi, \hat{O}_p}$ is related to a averaging over measurement bases, which is done automatically by the Bell projection. It can be shown that this $OTOC_{average}$ is measured by simply recording the likelihood of the measurement qubits being in the state $|\Psi^+\rangle, \langle P_\phi\rangle$. Fortunately, measuring this Bell state heralds teleportation of qubit 1's initial state to qubit 7: $|\langle\phi|\varphi\rangle|^2 = 1$. We call the averaged teleportation fidelity $\langle F_\phi\rangle$. Here, ϕ is one of the 6 eigenstates of all of the Pauli operators. These two observables, $\langle P_\phi\rangle$ and $\langle F_\phi\rangle$, are the essential result we hope to explore with these experiments.

Step 2 in [sequence 4.3](#) discusses preparing qubits in the $|\Psi^+\rangle$ Bell state, which we perform using the following circuit ($\alpha = \pm 1$:

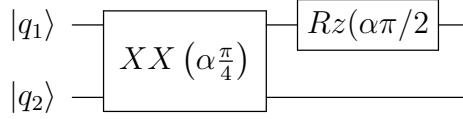


Figure 4.3: Quantum circuit for preparing two qubits in the $|\Psi^+\rangle$ Bell state.

By preparing our qubits this way, the scrambling unitaries can be performed on two different sets of qubits, clearing the path for our unique approach to measuring scrambling.

Step 3 is where all the real scrambling happens, so it is the most fraught with potential experimental errors. The scrambling-induced teleportation happens when both \hat{U}_s is a scrambling unitary and $\hat{U}_d = \hat{U}_s^*$. If \hat{U}_s is not a scrambling unitary or if $\hat{U}_d \neq \hat{U}_s^*$, then teleportation will not occur. In both of these cases, $OTOC_{average}$ will decay, despite the fact that no scrambling has occurred. Therefore, the teleportation fidelity is a significantly more reliable test for scrambling. More details on these topics and detailed derivations are given in Refs. [\[95\]](#) and [\[96\]](#).

Additionally, we can run deeper circuits that use a Grover's search protocol to measure scrambling with a deterministic teleportation instead of heralded teleportation [\[4\]](#). The required circuit is depicted in [Figure 4.4](#) excluding the gates within the purple border, we simply need to apply a special Grover's search gate, \hat{G} , as depicted in [Figure 4.5](#), and then another application of scrambling unitary. Luckily, we can apply \hat{G} with minimal overhead by using single-qubit rotations and qubit reassignment. We lose the ability to measure $OTOC_{average}$ with this circuit, but the scrambling measurement is now more direct. We can also take this effort a step

further using the circuit depicted in **Figure 4.4** with the gates in the purple border. This variant also has deterministic teleportation alongside a unity theoretical likelihood of measuring $|\Psi^+\rangle$ in the Bell measurement.

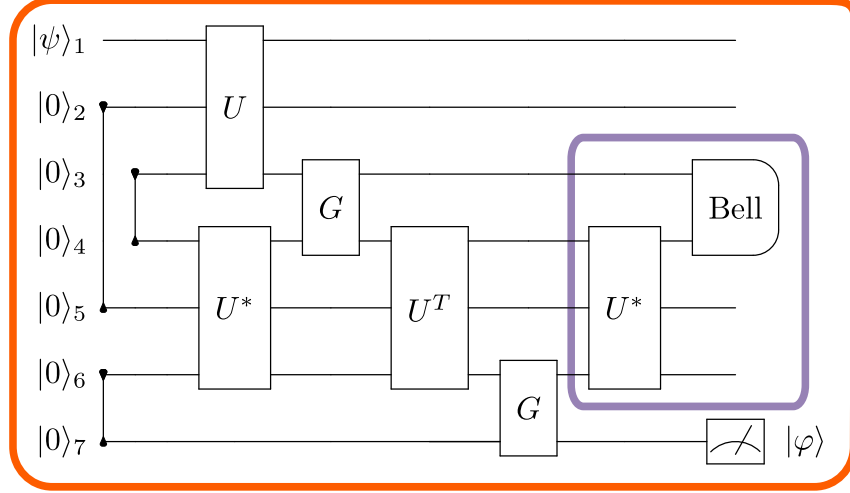


Figure 4.4: Quantum circuit for running a Grover's search variant of the scrambling measurement circuit. This circuit is deterministic, every experimental run should teleport information if \hat{U} is a scrambling unitary. No known OTOC measurement can be extracted from this experiment, though it may have the ability to measure higher moments of OTOC's.

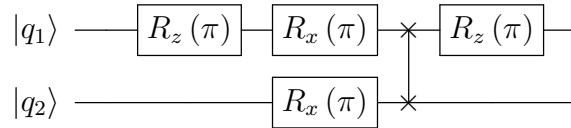


Figure 4.5: Circuit for implementing unitary for Grover's search variant. The swap gate is performed classically by swapping qubit labels during the data processing.

4.4 Experimental Setup

To implement the experiments described above, we needed to extend our 5 qubit quantum computer to 7 qubits. As mentioned in **Chapter 2**, the best way to trap long chains of equally-spaced ions is to trap extra spectator ions which act to alter the axial potential for the middle 7 ions to make them more equally spaced. To implement this, we found several sets of voltages that held 9 ions in seemingly correct positions, and then performed sideband-cooled Rabi flopping on the ions for each voltage set. The voltages that produce the best alignment will sample the Raman beams at their foci. Therefore, beam pointing fluctuations will be minimized; the ion will sample a far narrower spread of intensities in the Gaussian Raman beam; and Rabi flopping will decay significantly less. This proved to be a good method for calibrating alignment. Once we had 7 ions well-aligned onto our optical setup, calculating entangling gates proved straightforward despite using four additional ions than previous experiments [67]. A similar technique was subsequently applied for better alignment of 5 qubits using 7 ions for the results in Ref. [91].

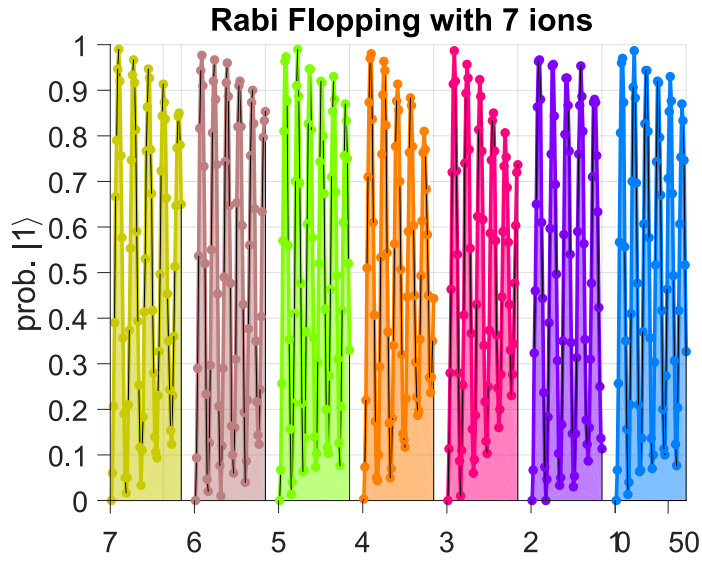


Figure 4.6: Rabi flopping on a sideband-cooled chain of nine ions. The same experiment was performed on many different voltage sets. By measuring decays during Raman beam Rabi flopping, we could deduce which voltage sets featured the best alignment. This figure is actually a 3D plot rotated so that the time axis is almost perpendicular to the page. This way, we can see the decay of the Rabi flops nicely. Each color in this figure corresponds to a different ion flopping for $50\mu\text{s}$.

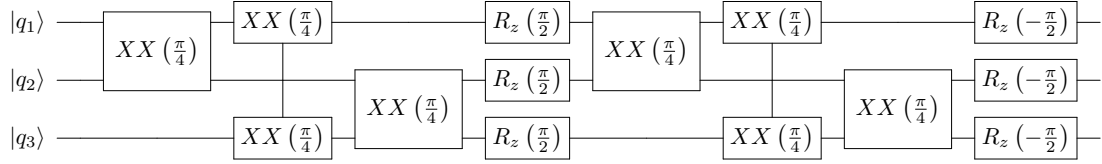


Figure 4.7: Gate sequence that affects a scrambling unitary used in **Figures 4.10** and **4.11**.

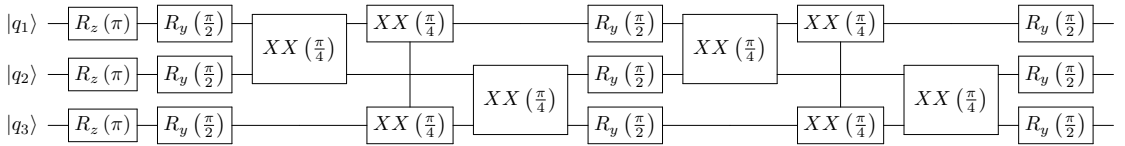


Figure 4.8: Gate sequence that affects a scrambling unitary used in **Figure 4.12**.

As mentioned, quantum scrambling transforms local information into non-local information and we needed to discover unitary operators that affect such a transformation using our native interactions. Generally, finding combinations of native gates that create a defined unitary is very difficult and optimization techniques are employed to find the most efficient combinations [97]. Instead of using such a method, we found scrambling operators by simulating the experimental sequence and testing different unitaries. We found that the circuits depicted in **Figures 4.7** and **4.8** are both maximally scrambling and have a similar structure. **Figure 4.7** has the interesting quality of performing three Ising gates along one basis and then another, which we assumed was likely the most efficient scrambling unitary on three qubits. To test whether **4.7** properly scrambles quantum information, we calculated the following:

$$\begin{aligned}
U^\dagger(X \otimes I \otimes I)U &= X \otimes Z \otimes Z & U^\dagger(I \otimes I \otimes Y)U &= X \otimes X \otimes Y \\
U^\dagger(I \otimes X \otimes I)U &= Z \otimes X \otimes Z & U^\dagger(Z \otimes I \otimes I)U &= Z \otimes Y \otimes Y \\
U^\dagger(I \otimes I \otimes X)U &= Z \otimes Z \otimes X & U^\dagger(I \otimes Z \otimes I)U &= Y \otimes Z \otimes Y \\
U^\dagger(Y \otimes I \otimes I)U &= Y \otimes X \otimes X & U^\dagger(I \otimes I \otimes Z)U &= Y \otimes Y \otimes Z \\
U^\dagger(I \otimes Y \otimes I)U &= X \otimes Y \otimes X
\end{aligned} \tag{4.14}$$

Similar arguments can be made for the unitary depicted in **Figure 4.8**, where each individual single-qubit Pauli operator is transformed into many-qubit Pauli operators. As mentioned, this is the signature of quantum scrambling. While performing these calculations are straightforward and sufficient to show that a unitary has

scrambling dynamics, large systems will become impossible to similarly simulate. Instead, one can use the experimental framework proposed in this chapter to test if a unitary scrambles with minimal overhead.

Lastly, we used **Figure 4.10** to move gates around to simplify the circuit. Since two maximally entangling XX gates in sequence are equivalent to performing $R_X(\pi)$ gates on both qubits involved, we could cancel out several gates. Finally, the experimental circuit we used takes the form of **Figure 4.9**.

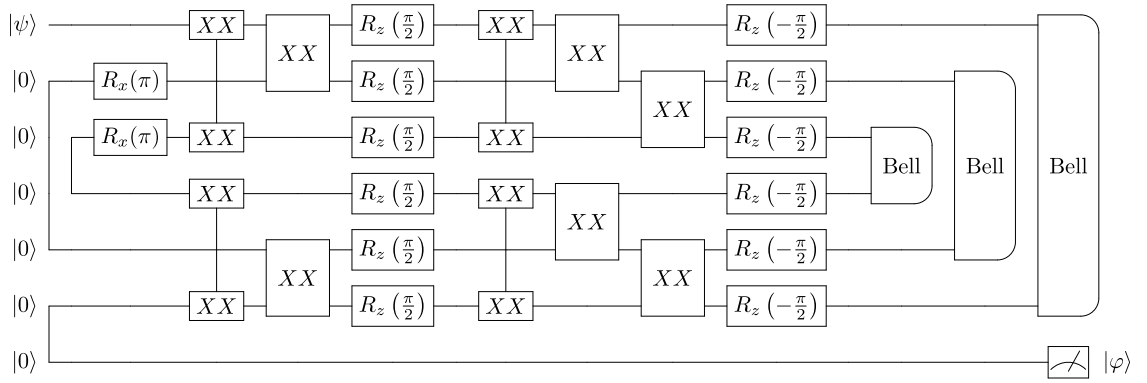


Figure 4.9: Optimized quantum circuit used to measure quantum scrambling using the identity in **Equation 4.10** and the unitary operator in **Figure 4.7**.

4.5 Results

To begin with, we wanted to demonstrate how the circuit in **Figure 4.1** really works to distinguish scrambling for experimental errors. Therefore, we turned \hat{U}_s into single-qubit rotations of angle θ and left \hat{U}_d as the identity operator, depicted in **Figure 4.10a**. Both sets of identity operations were generated using several maximally entangling $\hat{X}\hat{X}$ gates that cancel out, generating enough noise to ensure that the levels of experimental error stayed consistent throughout the set of experiments we performed. As we increased θ , we measured the decay of the OTOC measurement despite knowing that no scrambling had occurred. Meanwhile, the teleportation fidelity stayed at its minimum value of 0.5, see the orange data in **Figures 4.10b** and **d**. This proves that our OTOC measurement is sensitive to experimental errors like all other OTOCs.

Next, we realized that we could parameterize the amount of scrambling done by **Figure 4.7** by changing the angle of rotation of the R_z gates between $[\pi, \pi/2]$. Maximal scrambling occurs when these gates have an angle of $\pi/2$, and no scrambling occurs when the angle is π . The variable α is used to depict the absence ($\alpha = 0$) or presence ($\alpha = 1$) of scrambling. The data is presented in the dark purple points in **Figures 4.10c** and **d**. As α grows, we see the expected behavior of increased teleportation fidelity and a decreased OTOC measurement, suggesting that our experiment is behaving as expected.

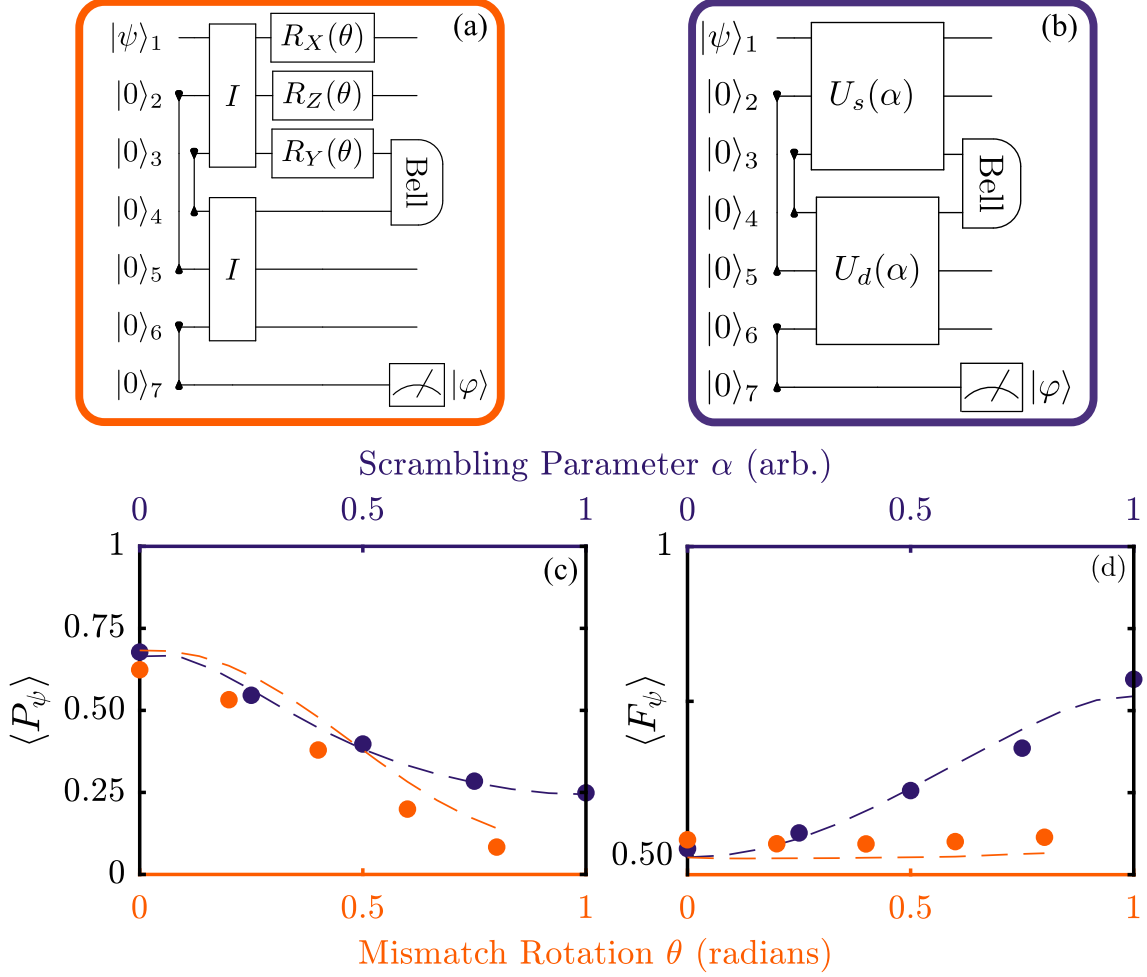


Figure 4.10: (a) Quantum circuit for parameterizing the amount of mismatch between \hat{U}_s and \hat{U}_d . The mismatch is parameterized by simply applying single qubit rotations of an angle θ to three of the qubits and not the other three. Corresponding data appears as orange data points. (b) Quantum circuit for parameterizing the amount of quantum scrambling performed for a given value of α . Corresponding data appears as purple data points. (c) The OTOC measurement while scanning θ and α . Both experiments feature a decaying OTOC measurement despite only one having an increase in the amount of quantum scrambling. (d) The teleportation fidelity while scanning θ and α . Only the purple data points change because the amount of scrambling has changed in that experiment. Error bars are too small to be seen and are generated from statistical uncertainties.

Also, we teleported the eigenstates of every Pauli operator and heralded teleportation using every Bell measurement pair. The data is depicted in **Figure 4.11**, and the average teleportation success rate is roughly 80%. The OTOC registers at its minimum value of 25% in the maximally scrambled case. The wide variety of teleportation experiments demonstrates that the once local information of qubit 1's state, $|\psi\rangle$, is now entangled with every qubit in the 7-qubit system. This shows quantitatively that we have scrambled $|\psi\rangle$. In addition, we perform the same experiment using a non-scrambling unitary, equivalent to the first three $\hat{X}\hat{X}$ gates of **Figure 4.7**. This circuit can entangle but not scramble, so it can only teleport information along specific axes. Indeed, we see that it only teleports z-basis states: $|0\rangle$ and $|1\rangle$. This teleportation can be reduced to a traditional quantum teleportation scheme [98]. In contrast to this, the scrambling-based teleportation is caused by the delocalization of the teleported state throughout the entire system. We see the OTOC measurement is much higher in the case of the non-scrambling unitary, due to simpler experimental requirements.

Lastly, we performed the Grover's search variants of the experiment, depicted in **Figure 4.12**. The color of the data matches the circuits in **Figure 4.4**. This data was only teleported in a few eigenbasis states and with only one Bell measurement pair. Despite the additional gates required for this data, the teleportation fidelities are still roughly 80%.

By performing these experiments, we show the impressive capabilities of our experimental apparatus and the theoretical framework we used to measure scrambling. Performing experiments with 7 qubits with similar fidelities as we had with 5

qubits demonstrates the extensibility of our experimental architecture. Secondly, a large-scale quantum computer could use our method of measuring scrambling with relatively low overhead: the procedure only requires a few measurements per unitary regardless of system size. The procedure can be used to understand properties of a collection of gates that is too large to simulate.

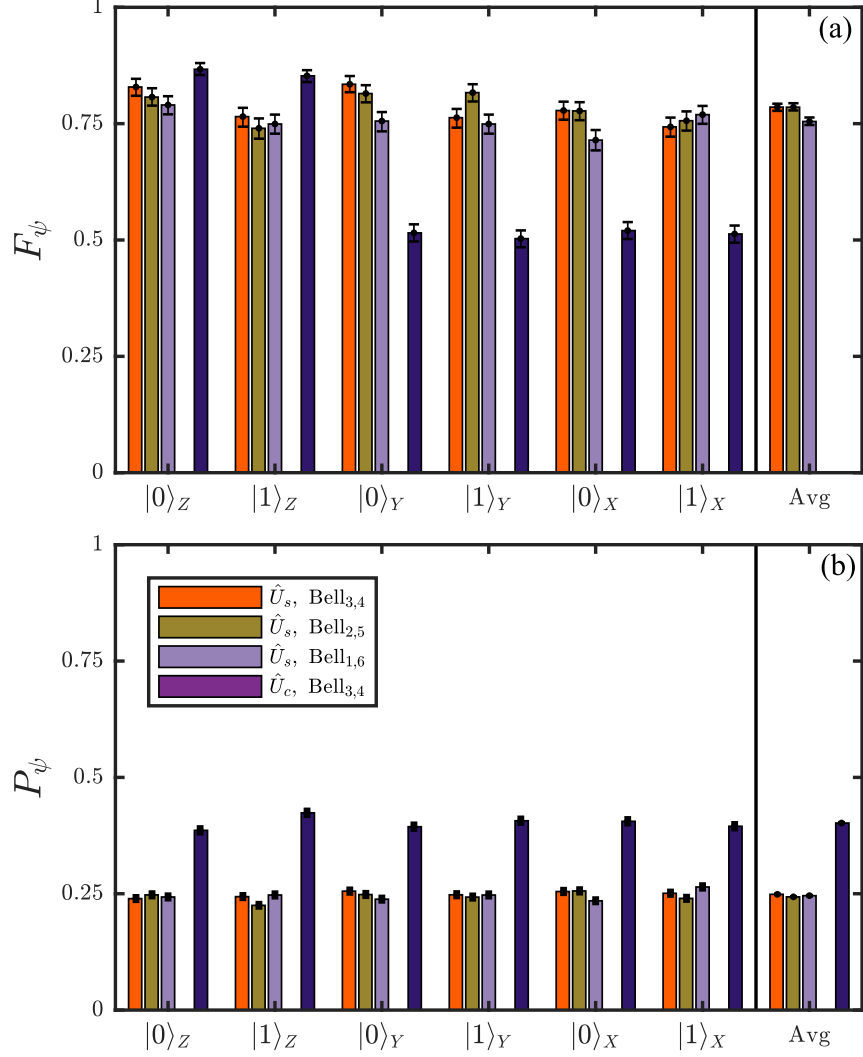


Figure 4.11: Results from teleporting different the basis states of each of the Pauli operators using quantum scrambling. $|0(1)\rangle_i$ is the positive (negative) eigenstate of the i -Pauli operator. Each of the three available Bell measurement pairs are used to teleport each state using the scrambling unitary in **Equation 4.7**. The measurement pair used are labeled in (b). We also attempted to use a non-scrambling unitary that could only teleport z-basis states. For the maximally scrambling unitary, the teleportation fidelities are included in (a) and are $\sim 80\%$. The OTOC measurements are reported in (b) and are fairly flat at their minimum of 25%.

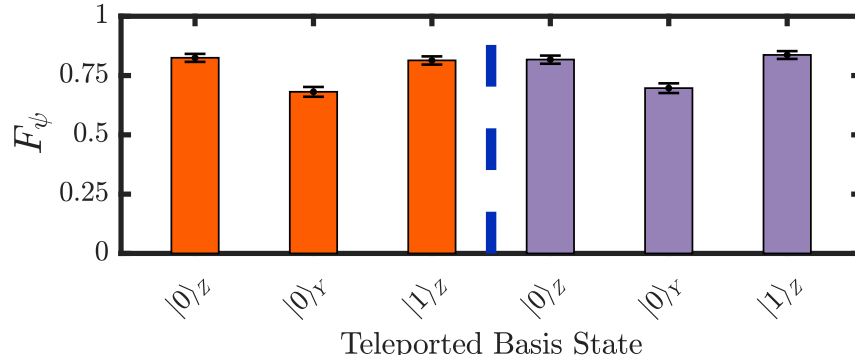


Figure 4.12: Results from teleporting information with a Grover’s search variant. The quantum circuit that depicts this experiment is portrayed in **Figure 4.4**. Two circuits are described there, one has additional post-selection features to flag failed experimental runs and the matching data is depicted here in light purple. Another has no post-selection features and the data is as collected, in orange. In either case, the teleportation fidelity around 80%, similar to the data in **Figure 4.11** despite having many more entangling operations.

Chapter 5: Quantum Error Correction

5.1 Introduction

Classical computers use signals defined by macroscopic properties like voltages and magnetic polarity that are inherently error-resistant. Components of such computers have error rates below 10^{-17} [99], making them famously reliable. When such high-fidelity components are not available, error-correction protocols are used with acceptable overheads. Quantum computers, as has been made clear throughout **Part 1** of this thesis, are far from boasting comparable error rates.

Some errors on quantum computers are coherent, meaning the imperfect operations are still Hermitian and applying their inverse will return the system to its previous state. Examples of such errors include rotating qubits with miscalculated Rabi frequencies or resonant frequencies. These can be eliminated with improved control schemes, such as the SK1 pulses or improved beam delivery, as discussed in **Chapter 3**.

Another, more insidious source of error is decoherence, where the qubit irreversibly turns into a mixed state containing no computational information. Such errors cannot be readily undone and the information is generally lost. Examples of

this include off-resonant photon scattering during Raman transitions and residual ion-phonon entanglement at the end of an entangling gate, as discussed in **Chapter 3**. Put another way, in the case of Schrödinger’s cat, the cat’s life is entangled with a qubit whose information is becoming increasingly unknowable. After some time, measuring the qubit state will no longer effect correlations with the cat’s life.

No matter how much improvement is made to the experimental system to minimize these types of errors, there will always remain some error rate on a quantum computer. Decoherence, most notably, is a fundamental *feature* of quantum mechanics [100, 101]; it is not merely a spurious behavior arising from a poorly controlled and imperfectly understood quantum system. If the qubit operations have sufficiently high fidelity, these errors can be dramatically reduced using quantum error correction (QEC) codes.

QEC codes work by entangling several physical qubits to create so-called logical qubits. The basis states of the logical qubit are spanned by different maximally entangled states [102, 103]. These logical states are more resistant to errors compared with bare qubits. Certain errors can be completely corrected using stabilizer measurement schemes, where errors in the logical qubit, called syndromes, are written onto ancillae qubits. By performing syndrome measurements, the experimentalist can determine which gates to apply onto the logical qubit to fix it [102].

The ability of a QEC code to run stabilizer circuits and correct for errors is limited by the fidelity of the QC’s operations and its idle errors. Idle errors are negligible in $^{171}\text{Yb}^+$ qubits [104], so the main determining factor is the fidelity of the operations, like those discussed in **Chapter 3**. If the operations are sufficiently high

fidelity, the logical qubit will be improved by every application of the stabilizers and the system is termed fault-tolerant [105]. If one builds a device with operations below the threshold, QEC will not improve the system and the qubit is not fault-tolerant [106]. In the experiments discussed below, we will demonstrate the *preparation* of a logical qubit that is fault-tolerant. Stabilizer measurements were performed, but were not able to improve the qubit. Therefore, only the preparation of the logical qubit is termed fault-tolerant and the rest of the QEC code cannot make the same claim.

5.2 Experimental Effort

On our experimental apparatus, we implemented elements of an error correcting code to see how the logical qubit shows improvements over our physical qubits [82]. A common naming convention for these codes is $[[n, k, d]]$. Where n is the number of physical qubits required to encode k logical qubits. The code has the ability to correct measured errors on up to $d - 1$ qubits. The Hamming distance is a measure of the single qubit operations necessary to move from one logical qubit state to another. The code we chose to use is the $[[4,2,2]]$ code, which requires 4 physical qubits. This code appears as part of the Steane code [102] as well as a face of a distance-3 color code [107], among others. The logical states ($|L_A L_B\rangle$) in the

z-basis are:

$$|00\rangle_L = (|0000\rangle + |1111\rangle)/\sqrt{2} \quad (5.1)$$

$$|01\rangle_L = (|0011\rangle + |1100\rangle)/\sqrt{2} \quad (5.2)$$

$$|10\rangle_L = (|0101\rangle + |1010\rangle)/\sqrt{2} \quad (5.3)$$

$$|11\rangle_L = (|0110\rangle + |1001\rangle)/\sqrt{2} \quad (5.4)$$

$$(5.5)$$

The logical states in the x-basis ($|+\rangle = (|0\rangle + |1\rangle)/\sqrt{2}$ and $|-\rangle = (|0\rangle - |1\rangle)/\sqrt{2}$)

are:

$$|++\rangle_L = (|++++\rangle + |-- --\rangle)/\sqrt{2} \quad (5.6)$$

$$|+-\rangle_L = (|+-+-\rangle + |-+-+\rangle)/\sqrt{2} \quad (5.7)$$

$$|-+\rangle_L = (|++--\rangle + |--++\rangle)/\sqrt{2} \quad (5.8)$$

$$|--\rangle_L = (|+- -+\rangle + |-++-\rangle)/\sqrt{2} \quad (5.9)$$

$$(5.10)$$

These states form a complete, normalized set of even parity states, each having an equal number of qubits in the $|0\rangle$ ($|+\rangle$) and $|1\rangle$ ($|-\rangle$) states in the z- (x-) basis. Later, we will exploit the parity of the states to write single-qubit errors onto an ancilla qubit.

Evolving the logical qubits from one state to another requires logical operations

of the form:

$$\hat{Z}_A = \hat{Z} \otimes \hat{Z} \otimes \hat{I} \otimes \hat{I} \quad (5.11)$$

$$\hat{Z}_B = \hat{Z} \otimes \hat{I} \otimes \hat{Z} \otimes \hat{I} \quad (5.12)$$

$$\hat{X}_A = \hat{X} \otimes \hat{I} \otimes \hat{X} \otimes \hat{I} \quad (5.13)$$

$$\hat{X}_B = \hat{X} \otimes \hat{X} \otimes \hat{I} \otimes \hat{I} \quad (5.14)$$

$$(5.15)$$

We created the $|00\rangle_L$ logical qubits using the circuit in **Figure 5.2**. If single error occurs at any point of this circuit, the error will propagate in one of two ways. Either $|L_B\rangle$ will be wrong, as seen in **Figure 5.2**, or the qubit state will fall outside of the logical codespace, see **Figure 5.2**.

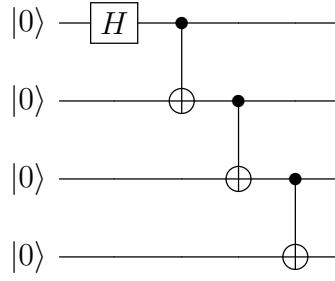


Figure 5.1: Circuit for preparing $|00\rangle_L$.

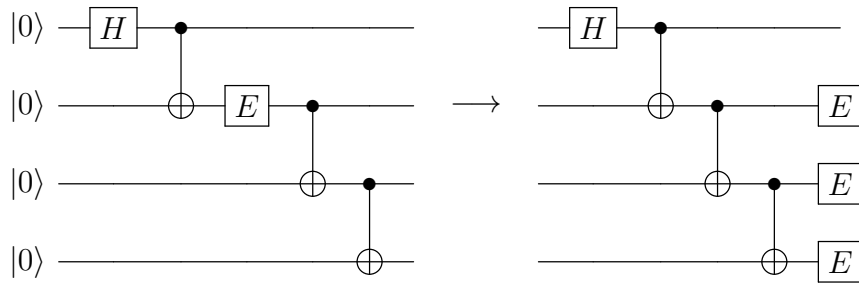


Figure 5.2: Error propagation example where the single-qubit error creates odd-parity states that are outside the QEC code subspace.

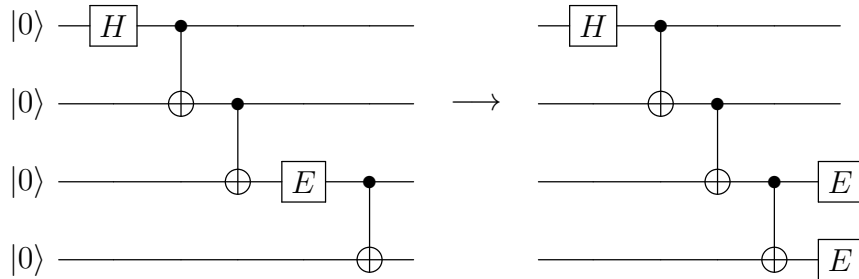


Figure 5.3: Error propagation example where the logical state remains in the logical subspace, but logical qubit $|L_B\rangle$ experiences an error.

In both cases, $|L_A\rangle$ is protected. In the first case, we see an example of how $|L_A\rangle$ is unaffected by single-qubit Pauli error, while $|L_B\rangle$ is not. In the second case, the qubits are not found to be in the four logical states and the data is discarded. In these ways, we claim that $|L_A\rangle$ does not have a single-qubit error channel while $|L_B\rangle$ does. If the main source of noise on our system is single-qubit errors and this error is sufficiently low, the preparation of $|L_A\rangle$ might be fault-tolerant.

To show this behavior, we created the $|00\rangle_L$ state and measured the qubits in the z basis, as seen in **Figure 5.4**. Data is presented as measured as well as SPAM-corrected. We disregard experimental runs where odd-parity qubit states are measured, the yield of preparing even-parity states is 91.1%, which means we lose 8.9% of the data. The inset shows the data after odd-parity states have been discarded. As we can see, $|L_A\rangle$ ($|L_B\rangle$) is measured correctly with 99.7% (98.1) probability. Despite using entangling gates with 96 – 97% fidelity, we created a logical qubit with only 0.2% error. The large difference in prepared fidelity between the two logical qubits shows how $|L_A\rangle$ is unaffected by single-qubit errors, while $|L_B\rangle$ is not. This suggests that our discussion of propagation of single Pauli errors is correct, and that the major sources of error on our system are random, single-body errors that are below the threshold required to fault-tolerantly prepare $|L_A\rangle$.

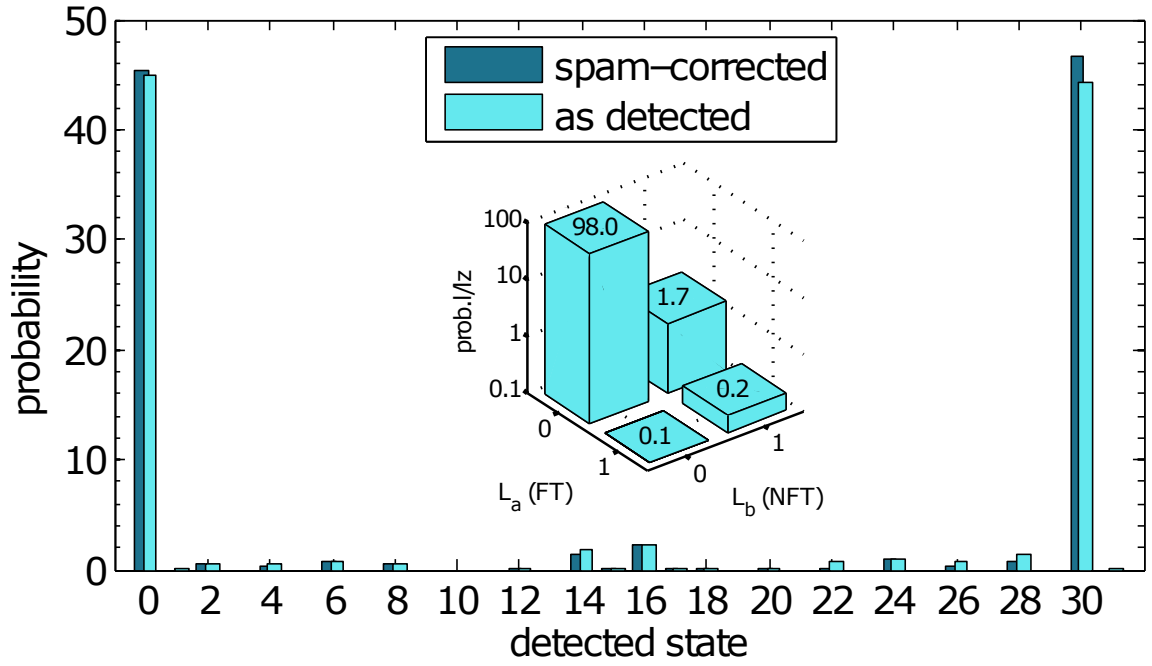


Figure 5.4: We prepare the logical state $|00\rangle_L$ state using the circuit in [Figure 5.2](#) and measure it in the z-basis. Raw data as well as SPAM-corrected data are included on the graph. The inset compares the errors on the preparation of the fault-tolerant logical qubit and the non-fault-tolerant logical qubit.

As with any QEC code, the code has stabilizers that can be used for local syndrome extraction via an ancilla qubit [5, 108]. We can use a bare, physical qubit as an ancilla during the stabilizer circuits depicted in **Figure 5.5** and **Figure 5.6**. These circuits write the syndrome information onto the ancilla that tells the user if the qubits have fallen outside the codespace using a non-destructive measurement. While other codes have more detailed syndromes like type and location of the error, the Hamming distance here is too small and we only learn if an error has occurred.

These stabilizer measurements write bit-flip (Z basis) or phase flip (X basis) errors onto the ancilla qubit. We perform them with the circuits depicted in Figs. 5.5 and 5.6. If the ancilla is measured to be in the $|0\rangle$ state, then no error has occurred. Otherwise, the run can be discarded. The stabilizers are performed in separate experiments because only one ancilla was available.

We performed the stabilizer measurement on our $|00\rangle_L$ state and measured in both the Z- and X-axes, see **Figure 5.7**. Again, we see errors on $|L_A\rangle$ that are an order of magnitude less likely than on $|L_B\rangle$. When the ancilla is measured in the $|1\rangle$ state, we conclude that an error has occurred, though we do not know where. This was significantly more likely after the S_X stabilizer. This tells us that our preparation of $|00\rangle_L$ has significant phases errors, but not bit-flip errors. Different logical states were prepared and analyzed with stabilizer measurements. The results are summarized in **Table 5.1**.

$S_X :$

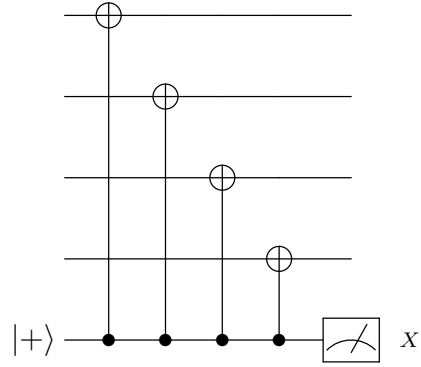


Figure 5.5: This circuit writes z-basis errors from the logical qubit onto the ancilla, despite being called S_X . Ideally, the ancilla qubit would be measured independently from the rest of the qubit register, and the quantum computer would fix single-qubit x-basis errors using this information.

$S_Z :$

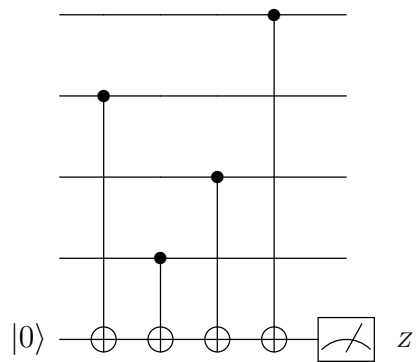


Figure 5.6: This circuit writes x-basis errors from the logical qubit onto the ancilla, despite being called S_Z . Like above, an ideal implementation of an error correction code would extract the information about the logical qubits using the ancilla and use that information to correct its own errors.

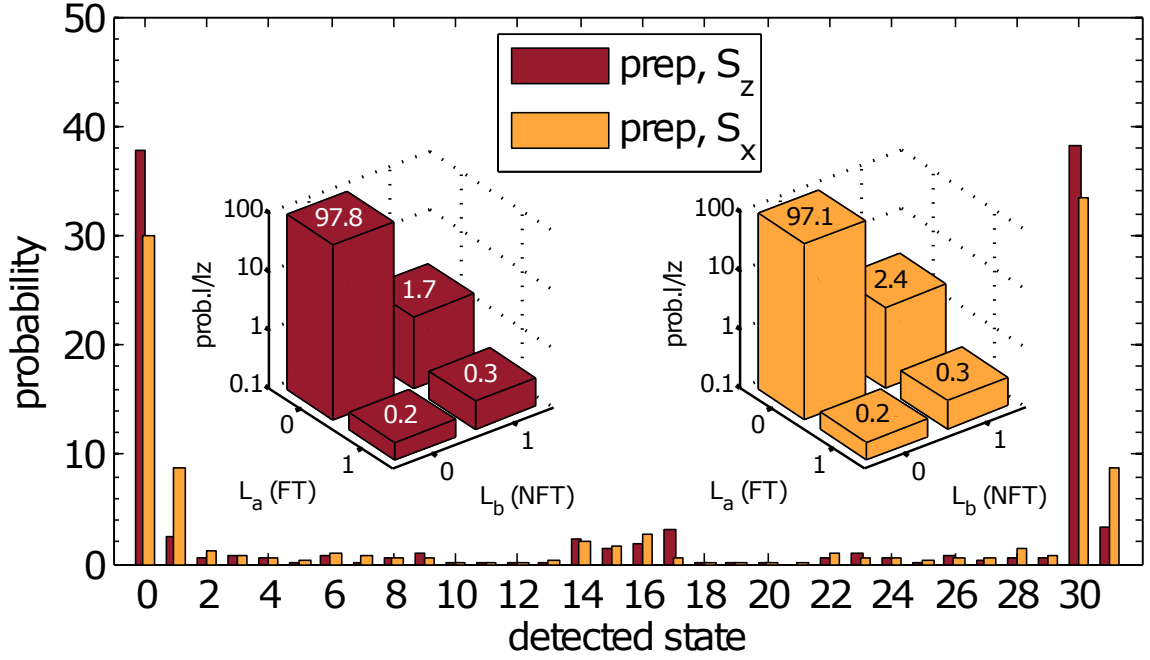


Figure 5.7: We prepare the $|00\rangle_L$ state and performing stabilizer measurements as described in the circuit in **Figure 5.5** and **5.6**. The relatively poor fidelity of the S_X stabilizer demonstrates the phase error of the entangling gates discussed in **Chapter 3**. This data was taken prior to the improvement to the $\hat{X}\hat{X}$ gate phase. Again, the inset shows the relative errors on the fault-tolerant qubit and the non-fault-tolerant qubit.

	yield	meas. logical state $ L_a L_b\rangle$				meas. basis
		$ 00\rangle$ $ ++\rangle$	$ 01\rangle$ $ +-\rangle$	$ 10\rangle$ $ -+\rangle$	$ 11\rangle$ $ --\rangle$	Z X
$ 00\rangle_L$	91.1	98.0	1.7	0.1	0.2	Z
$ 00\rangle_L S_z$	77.8	97.8	1.7	0.2	0.3	Z
$ 00\rangle_L S_x$	65.2	97.1	2.4	0.2	0.3	Z
$ ++\rangle_L$	91.1	94.8	3.9	0.2	0.2	X
$ ++\rangle_L S_z$	68.2	93.0	4.2	1.3	1.5	X
$ ++\rangle_L S_x$	72.1	94.3	4.5	0.5	0.7	X
$ - 1\rangle_L$	90.1	0.2	50.5	0.1	49.2	Z
$ - 1\rangle_L$	87.0	0.3	0.3	50.4	48.9	X
$ - 1\rangle_L S_z$	79.9	0.2	50.0	0.1	49.7	Z
$ - 1\rangle_L S_x$	75.5	0.4	0.3	50.0	49.2	X
$ - 1\rangle_L S_z$	72.1	0.6	50.2	0.5	48.7	Z
$ - 1\rangle_L S_x$	76.2	0.4	0.4	50.0	49.2	X
$ 0+\rangle_L$	93.2	47.4	52.5	0.06	0.05	Z
$ 0+\rangle_L$	92.4	50.0	0.04	49.8	0.09	X
$ 0+\rangle_L S_z$	81.6	48.3	51.3	0.2	0.2	Z
$ 0+\rangle_L S_x$	68.5	47.1	2.4	47.4	3.1	X
$ 0+\rangle_L S_z$	72.0	48.3	51.5	0.2	0.1	Z
$ 0+\rangle_L S_x$	70.9	49.4	0.4	49.7	0.5	X
$ 11\rangle_L S_z$	73.3	0.4	0.3	2.8	96.5	Z

Table 5.1: A summary of results from preparing logical states and applying stabilizer measurements.

Another experiment was performed by purposefully introducing calibration errors in the entangling gates during the preparation of the logical states. The results are plotted in **Figure 5.8**. It is not surprising that the yield suffers due to miscalibration, the fact that the likelihood of an error occurring on the logical qubits stays quite flat has major ramifications. Miscalibration of the $\hat{X}\hat{X}$ gates reflects a very realistic experimental noise source of under/over rotations of the $\hat{X}\hat{X}$ gates due to imperfectly calibrated Rabi frequencies. This type of error is a correlated error, since it causes bit flip errors on multiple qubits due to their entangled state. In fact, unwanted entanglement is the major source of correlated errors possible in the system. Another common cause of unwanted entanglement is crosstalk entanglement. Since there is $\sim 1 - 2\%$ addressing crosstalk of the Raman beams on neighboring ions, undesirable entanglement will happen between target ions and their nearest neighbors. Similar to the miscalibrated $\hat{X}\hat{X}$ gates, this will produce unwanted correlations within the system. Severely minimizing crosstalk entanglement and imperfect entanglement from miscalibrated Rabi frequencies is essential because correlated noise raises the fidelity threshold of the qubit operations required to reach fault tolerance [109]. In the experiment plotted in **Figure 5.8**, the naturally-occurring correlated noise from crosstalk entanglement is convolved with the artificially introduced miscalibration errors. Despite the potentially large source of correlated errors, the fault-tolerant preparation of the code is maintained. This suggests that the level of correlated errors in our system is below the threshold necessary for fault-tolerant preparation of the logical state.

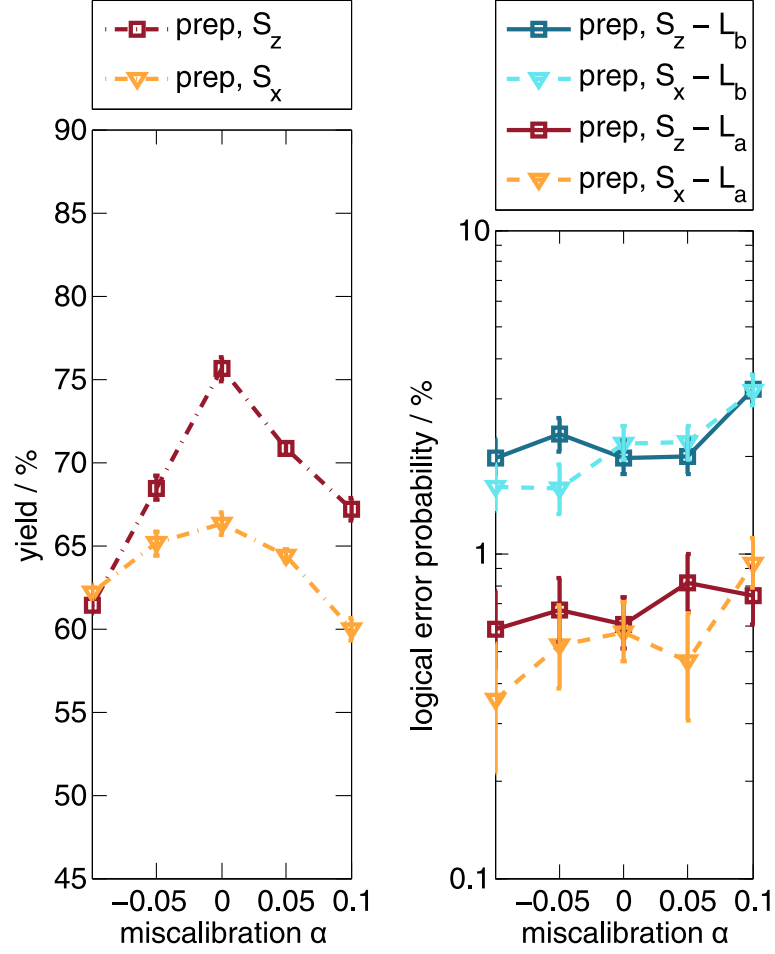


Figure 5.8: Preparing $|00\rangle_L$ with miscalibrated entangling gates and then extracting syndrome measurements using properly calibrated gates. (a) Since the calibration has a larger effect on the z -basis error, it is no surprise that the yield for S_x stabilizer is effected more than the S_z stabilizer. (b) In either case, the logical error probability is relatively flat.

Chapter 6: Measuring Rényi Entropy

6.1 Measuring Entanglement

Entanglement is a precious resource in quantum computing. It is the backbone of every non-trivial multi-qubit quantum gate and enables quantum error correction, as seen in **Chapter 5**. Therefore, quantifying and measuring the amount of entanglement produced by a given Hamiltonian or set of quantum gates is an important and open question. Here, we will present a method for measuring entanglement using the Rényi entropy. As done in Ref. [110], we begin our discussion by considering a system with two subsystems:

$$|\Psi\rangle = \sum_{i,j} c_{i,j} |a_i\rangle \otimes |b_j\rangle \quad (6.1)$$

Where states $|a_i\rangle$ and $|b_j\rangle$ form complete, orthonormal bases A and B . The reduced density matrix of subsystem A is defined by performing a partial trace over subsystem B [99]:

$$\rho_A = \text{Tr}_B(|\Psi\rangle \langle\Psi|) = \sum_{i,j} c_{i,j} |a_i\rangle \langle a_i| \text{Tr}(|b_j\rangle \langle b_j|) = \sum_{i,j} c_{i,j} |a_i\rangle \langle a_i| \langle b_j|b_j\rangle \quad (6.2)$$

The reduced density matrix reports the population statistics of subsystem A and is also a witness of the entanglement of the entire system. The simplest example of two such subsystems are two qubits. Let's consider several sets of qubit states and their respective reduced density matrices:

$$\begin{aligned}\Psi_1 &= |0\rangle_A \otimes |0\rangle_B \\ \rho_1 &= \begin{bmatrix} 1 & 0 \\ 0 & 0 \end{bmatrix}\end{aligned}\tag{6.3}$$

$$\begin{aligned}\Psi_2 &= \frac{1}{2}(|0\rangle_A + |1\rangle_A \otimes |0\rangle_B + |1\rangle_B) \\ \rho_2 &= \frac{1}{2} \begin{bmatrix} 1 & 1 \\ 1 & 1 \end{bmatrix}\end{aligned}\tag{6.4}$$

$$\begin{aligned}\Psi_3 &= \frac{1}{\sqrt{2}}(|0\rangle_A \otimes |0\rangle_B + |1\rangle_A \otimes |1\rangle_B) \\ \rho_3 &= \frac{1}{2} \begin{bmatrix} 1 & 0 \\ 0 & 1 \end{bmatrix}\end{aligned}\tag{6.5}$$

In **equations 6.3** and **6.4**, the two subsystems are unentangled and their reduced matrices are reflective of that fact: they both look like systems in a pure state. In contrast we have **Equation 6.5**, where the reduced density matrix looks like that of a decoherent or mixed state. It has the same diagonal components as in **Equation 6.4**, but the off diagonal components have disappeared. The correlations between the two levels of subsystem A cannot be described without also representing its entangled partner. We can use the reduced density matrix to quantify the

amount of entanglement between the subsystems using the Rényi entropy [110]:

$$S_n = \frac{1}{1-n} \log_2(R_n) \quad (6.6)$$

$$R_n = \text{Tr}(\rho_A^n)$$

In the limit of $n \rightarrow 1$, this is equivalent to the von Neumann entropy, another important information theoretic quantity that can also be considered when studying entanglement. The log of the second Rényi entropy, $\log(R_2)$, decays from 1 as entanglement grows between the subsystems. In the example in **equations 6.3, 6.4, and 6.5**, the Rényi entropy would be measured as 1, 1, and 0.5 respectively. These measurements can be taken on a quantum computer, though measuring full density matrices quickly becomes difficult on systems greater than 3 qubits. Instead, the Rényi entropy can be directly measured using two identical experimental systems with the proper quantum control [111]:

$$R_2 = \langle \Psi | \langle \Psi | \text{Swap}_A | \Psi \rangle | \Psi \rangle \quad (6.7)$$

where we define Swap_A as:

$$\begin{aligned} \text{Swap}_A | \Psi \rangle | \Psi' \rangle &= \text{Swap}_A \sum_{i,j} c_{i,j} |a_i\rangle \otimes |b_j\rangle \sum_{i',j'} c_{i',j'} |a_{i'}\rangle \otimes |b_{j'}\rangle \\ &= \sum_{i,j} c_{i,j} \sum_{i',j'} c_{i',j'} |a_{i'}\rangle \otimes |b_j\rangle |a_i\rangle \otimes |b_{j'}\rangle \end{aligned} \quad (6.8)$$

Furthermore, we can directly measure the Rényi entropy using only an ancilla qubit by preparing the ancilla in the $|+\rangle$ state and placing it as the control of a

CSwap, or Fredkin, gate. The single ancilla measures the expectation value of the CSwap operator. Put another way, the sequence affects a phase kickback if the Swap occurs between subsystems that are both part of an entangled state [112], so measuring the ancilla in state $|0\rangle$ ($|1\rangle$) reveals the absence (presence) of entanglement. If $|\Psi\rangle$ grows to any arbitrary size, the number of ancillae needed stays constant at 1, and the number of *CSwap* gates grows linearly with the size of subsystem A . Every component of A will be acted on by a Fredkin gate controlled by the single ancilla.

With our experimental apparatus, we implemented the CSwap gate with a process fidelity of 86.8(3)%, and the state of the control qubit is correct with 94.0(2)% probability. These reported numbers are SPAM corrected and the uncertainties are statistical. See **Figure 6.1**. Next, we set our sights on a sensible simulation that generates entanglement over time.

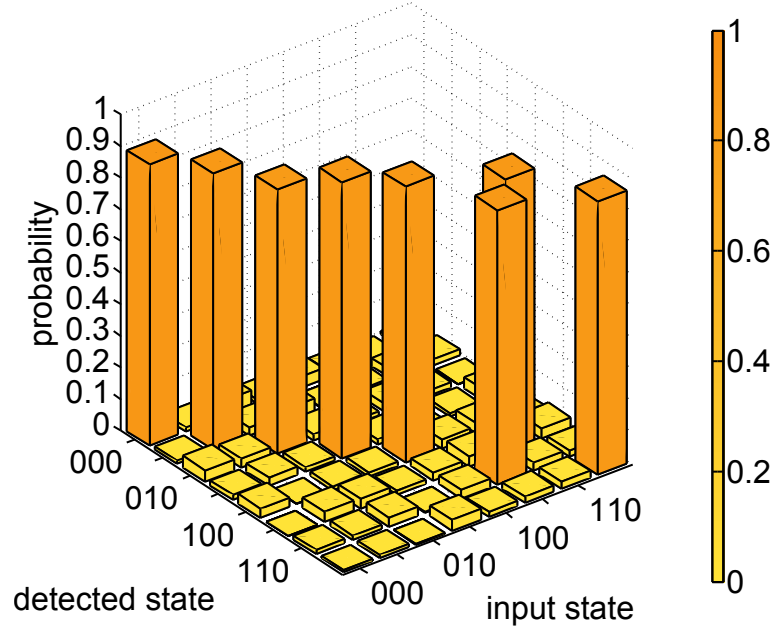


Figure 6.1: State-to-state transfer matrix after applying a Fredkin gate optimized for our native quantum gates and error model. The gate is performed with an average fidelity of 94.0(2)%. Data is corrected for SPAM errors.

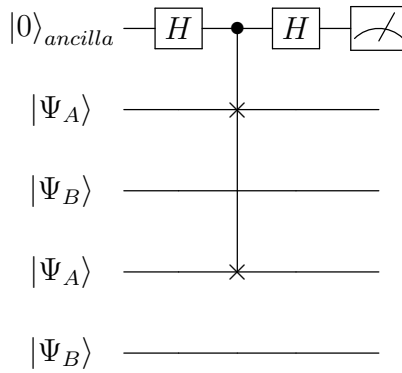


Figure 6.2: CSwap operator applied onto a four-qubit system in such a way that the Rényi entropy is readout onto an ancilla qubit. Two copies of a quantum system $|\Psi\rangle$ are needed to measure the entanglement within $|\Psi\rangle$.

6.2 Hamiltonian Mapping

To test this measurement protocol, we developed a simulation of two electrons in a lattice, a toy version of the Fermi-Hubbard model [113, 114]. The Hamiltonian takes the form:

$$\hat{H} = -J \sum_{\langle i,j \rangle, \phi} (\hat{c}_{i,\phi}^\dagger \hat{c}_{j,\phi} + \hat{c}_{j,\phi}^\dagger \hat{c}_{i,\phi}) + U \sum_{i=1}^N \hat{n}_{i,\uparrow} \hat{n}_{i,\downarrow} \quad (6.9)$$

where $\hat{c}_{i,\phi}^\dagger$ and $\hat{c}_{i,\phi}$ are respective creation and annihilation operators for electrons in spin state $\phi \in \{\downarrow, \uparrow\}$ and site i . J is the hopping strength between lattice sites, U is the on-site interaction, and $\hat{n}_{i,\phi} = \hat{c}_{i,\phi}^\dagger \hat{c}_{i,\phi}$ is the electron number operator for site i . By considering two electrons, two sites, and conservation of total spin ($S_z = 0$), we can study the simplest non-trivial implementation of the Hamiltonian [71]. Though simply describing electrons on a lattice and their interactions, the Fermi-Hubbard model has massive implications and may describe high-temperature superconductivity. Solving such a problem at the thermodynamic limit is beyond the capabilities of classical computers, but can be efficiently simulated on a quantum computer using many of the same techniques described here [10, 115].

State of the art experiments that study this Hamiltonian typically use lattices of ultra-cold Fermi gases, where very large numbers of fermions are readily available [116, 117] and the toolbox necessary to implement the interaction is highly developed [118]. Our experiment, in contrast, has no direct method for engineering the Hamiltonian. Instead, our system is a universal quantum computer that

can efficiently simulate many different problems as long as a sufficient mapping is available.

To understand such mappings, we need to understand the difference between the Pauli-type unitaries native to digital quantum systems (see Sec.3) and fermionic creation and annihilation operators. Let's begin by looking at how these fermionic operators effect a particle's state alongside a somewhat analogous Pauli-type operator.

$$\begin{aligned}\hat{a}^\dagger |0\rangle &= |1\rangle, \hat{a} |1\rangle = |0\rangle \\ \hat{\sigma}_+ |0\rangle &= |1\rangle, \hat{\sigma}_- |1\rangle = |0\rangle\end{aligned}\tag{6.10}$$

The fermionic operators flip spin states, just like $\hat{\sigma}_{+(-)} = \frac{1}{2}(\sigma_x - (+)i\sigma_y)$ operators. From here, we see that there is a native operator, that seems to match the creation and annihilation operators. The problem arises when we want to consider the fermionic canonical anticommutation relations:

$$\begin{aligned}\{\hat{a}_i, \hat{a}_i\} &= \{\hat{a}_i^\dagger, \hat{a}_i^\dagger\} = 0, \{\hat{\sigma}_i^+, \hat{\sigma}_i^+\} = \{\hat{\sigma}_i^-, \hat{\sigma}_i^-\} = 0 \\ \{\hat{a}_i \hat{a}_j, \hat{a}_i^\dagger \hat{a}_j^\dagger\} &= I, \{\hat{\sigma}_i^+ \hat{\sigma}_j^+, \hat{\sigma}_i^- \hat{\sigma}_j^-\} \neq I\end{aligned}\tag{6.11}$$

As we can see the Pauli operators fail to obey the proper anticommutation relations for qubit registers of larger than a single qubit. The simplest way to correct this mapping is to use the Jordan-Wigner transformation of the form [119]:

$$\hat{a}_i = \sigma_i^- \bigotimes_{j<i} \sigma_j^z, \hat{a}_i^\dagger = \sigma_i^+ \bigotimes_{j<i} \sigma_j^z\tag{6.12}$$

Another popular choice is the Bravyi-Kitaev transformation [7], which uses parity information to improve mapping efficiency and can substantially reduce the number of gates required for a simulation [120]. Both transformation techniques use the second-quantization Fock basis.

For our simple example of two electrons in two sites of a Fermi-Hubbard model, the number of qubits required (N_q) is equal to the number of electron states for each electron ($N_s = 4 = N_q$). In certain cases like ours, one can use the inherent symmetries and conservation laws within a Hamiltonian to map it onto a smaller Hilbert space. Since our Hamiltonian in **Equation 6.9** conserves total spin, S_z , as well as the number of electrons, N_e , we can use the following first-quantization mapping that uses a number of qubits equal to the number of electrons $N_e = N_q = 2$:

$$\begin{aligned}
|00\rangle &= \{1_\uparrow, 1_\downarrow\} \\
|01\rangle &= \{1_\uparrow, 2_\downarrow\} \\
|10\rangle &= \{2_\uparrow, 1_\downarrow\} \\
|11\rangle &= \{2_\uparrow, 2_\downarrow\}
\end{aligned} \tag{6.13}$$

In this formalism, $\{i_{\phi_i} j_{\phi_j}\}$ are Slater determinants that describe the different configurations of possible electron occupations. States $|00\rangle$ and $|11\rangle$ represent both electrons occupying lattice site 1 and 2, respectively. States $|01\rangle$ and $|10\rangle$ refer to the spin-up (-down) electron residing in site 1 (2) and vice versa. With this mapping,

we can rewrite our Hamiltonian as unitary operators:

$$H = \begin{bmatrix} 0 & -J & -J & 0 \\ -J & 0 & 0 & -J \\ -J & 0 & 0 & -J \\ 0 & -J & -J & 0 \end{bmatrix} + \begin{bmatrix} U & 0 & 0 & 0 \\ 0 & 0 & 0 & 0 \\ 0 & 0 & 0 & 0 \\ 0 & 0 & 0 & U \end{bmatrix} \quad (6.14)$$

The first term of the Hamiltonian effects the creation or annihilation operators. Each state in the mapping described in **Equation 6.13** can evolve into only two other states as determined by the Hamiltonian. Therefore, we see two $-J$ terms on each row of the Hamiltonian. The electron number operator observes population in a given site, so we only see U terms in the diagonal corners of this 2-site system.

Up to a constant, the Hamiltonian written in our first-quantization mapping can be written in a Pauli operator Hamiltonian of the form:

$$H(t) = -J(\hat{\sigma}_1^x + \hat{\sigma}_2^x) + U\hat{\sigma}_1^z\hat{\sigma}_2^z \quad (6.15)$$

Because this Hamiltonian has two terms that do not commute, we cannot directly apply it on our system and must rely on applying each term individually using Trotterization.

6.3 Trotterization

The Trotter formula is a method to adiabatically combine non-commuting matrices [99, 121]. It is necessary because digital quantum computers can only apply native interactions onto qubits and only one operation can be applied onto

a given qubit at a time. If the operators commute and are well-described by the native interaction, this issue is circumvented by applying them sequentially with no introduced error. More commonly, we are interested in applying arbitrary operators that do not generally commute and we need to rely on some other method to create the desired evolution like Trotterization.

Trotterization works by preparing the ground state of a known Hamiltonian and then adiabatically evolving the system with a second, non-commuting Hamiltonian [122]. The adiabaticity is achieved using short-time evolution steps, during which the Hamiltonian is approximately time independent. In this way, the system evolves from the ground state of the first Hamiltonian to the ground state of the second, target Hamiltonian. Mathematically, the approach can be written as:

$$U = e^{-i(H_a+H_b)\tau} = (e^{-iH_a\tau/n} e^{-iH_b\tau/n})^n + \epsilon_{\mathcal{O}(\delta^2)} \quad (6.16)$$

$$\approx (e^{-iH_a\delta} e^{-iH_b\delta})^n \quad (6.17)$$

where $\delta = \tau/n$ is the small step size through the evolution up to the full time τ , and $\epsilon_{\mathcal{O}(\delta^2)}$ is the error inherent in this method. For a constant τ , the accuracy of the Trotterization improves when δ is made smaller, though this increases the computational complexity and the likelihood for systematic errors. We can re-write our Fermi-Hubbard Hamiltonian using the Trotter formula to first order:

$$\hat{U}_{FH} = \prod_{m=1}^N \left(e^{i\hat{\sigma}_1^x \delta} e^{i\hat{\sigma}_2^x \delta} e^{-i\frac{\delta^2}{2\tau} m \hat{\sigma}_1^z \hat{\sigma}_2^z} \right) \quad (6.18)$$

Each application of \hat{U}_{FH} evolves the system by δ towards the final evolution time of τ . Using the quantum gate definitions from **Chapter 3**, we can implement this Hamiltonian using native gates with the circuit in **Figure 6.3**. We begin the circuit by preparing the qubits in the ground state of the Hamiltonian at time $t = 0$, which is $H = -\hat{\sigma}_1^x - \hat{\sigma}_2^x$. This is accomplished by the Hadamard gates, which put each qubit into the state $\frac{1}{\sqrt{2}}(|0\rangle + |1\rangle)$. The adiabatic evolution describes one of N steps of evolution towards $\delta = Nt = \tau$. The circuit also includes the Fredkin gate, which projects Rényi entropy information onto the ancilla qubit as discussed. The last set of Hadamard gates on the non-ancilla qubits, will be discussed in the following section.

With a two-qubit Hamiltonian in hand, we can simulate two copies of this system and have an ancilla qubit available using only five qubits.

6.4 Experimental Results

Several different experiments were performed using the methods described above. Firstly, we calculated Hamiltonian expectation values and Rényi entropies *in silico* for sets of durations and interaction strengths without Trotterization to get some idea of what to expect from the dynamics of our simulations. Since the inherent Trotter errors cause deviations from these actual values, we also simulated *in silico* the Trotterized experiments to understand the size of these deviations. Next, we ran the experiment on our quantum computer using two different methods of evolution:

Method 1, Scan the number of adiabatic evolution steps (N_{steps}) and hold τ and δ constant. This method **increases** the number of quantum gates as we scan N_{steps} . This is termed Method 1.

Method 2, Hold N_{steps} constant and scan τ and δ . Here, the number of gates is **constant** at every step through the evolution, termed Method 2.

We implemented both types of evolution and measured the expectation value of the Hamiltonian $\langle H \rangle$. This is done by measuring each term of the Hamiltonian and summing them appropriately. We measure $\langle \sigma_1^z \sigma_2^z \rangle$, $\langle \sigma_1^x \rangle$, and $\langle \sigma_2^x \rangle$. The z-basis correlation measurement is performed by measuring in the z-basis and calculating $Prob(11) + Prob(00) - Prob(01) - Prob(10)$. The x-basis measurements are single-qubit measurements, so we simply measure in the x-basis with Hadamard gates before measuring in the native z-bases, and calculate $Prob(1) - Prob(0)$. Experimental and theoretical data is plotted in **Figure 6.4(a)**, alongside the exact solution without the Trotter approximation. We found that the number of entangling gates performed in each circuit lowers the fidelity of the result by some constant amount. As such, we subtracted a straight line with slope 0.063 from the results in Method I and a constant value of 0.58 from Method II. Mitigation errors in this manner are useful on so-called noisy, intermediate-scale quantum devices [123]. Subtracting a linear error-model is based on a first-order expansion of applying quantum gates with 98 – 99% fidelity, where the leading-order term is linear [124]. Subtracting a constant energy error from the results can be seen in a similar light, though we do not need to consider a growing amount of error since the number of operations

is constant. The value of 0.58 was determined from measuring the energy offset at $U = 0$, where no evolution has taken place. Clearly, Method II has less Trotter error compared with Method I.

Next, we measured the Rényi energy using both methods, as depicted in **Figure 6.4** (b-c). Both methods are similar, but have different amounts of Trotter error. Because we have significant systematic errors due to imperfect quantum gates, we need to consider which method is preferable. Method I has more systematic errors as the evolution gets longer, as seen by larger discrepancies with the theoretical curve. Initially, with no evolution, the measured Rényi entropy is roughly 10% from the ideal value using Method I. By the end of the evolution, the gap has widened to nearly 30%. In contrast, the error in method II stays constant at around 30%. Comparing either method to the exact solution (also plotted), we see that the experimental errors are dominant compared to the Trotterization errors in **Equation 6.16**.

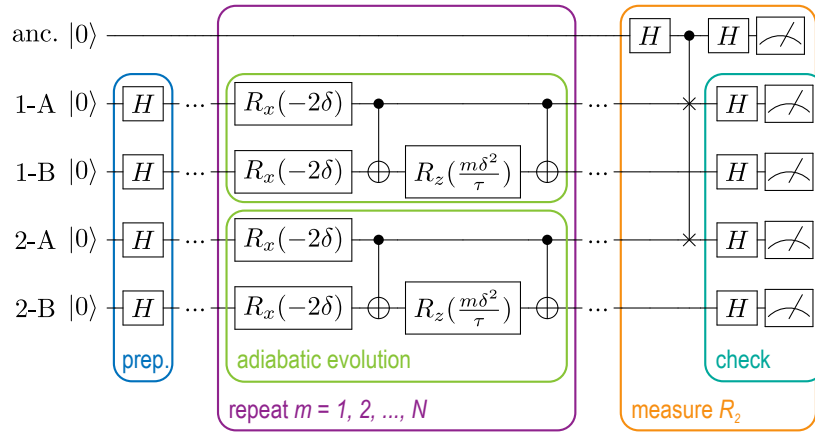


Figure 6.3: Quantum circuit depicting the central experiment on this topic. The first Hadamard gates prepare the subsystems into ground states of the Hamiltonian. Next, we repeat a Trotterization of the Fermi-Hubbard Hamiltonian using our native gate set. This is repeated an integer number of times before we apply the Fredkin gate to readout the Rényi entropy of the two copies of the systems. Lastly, the final Hadamard gates are used to enable a post-selection argument that we use to ignore failed experimental runs in post-processing.

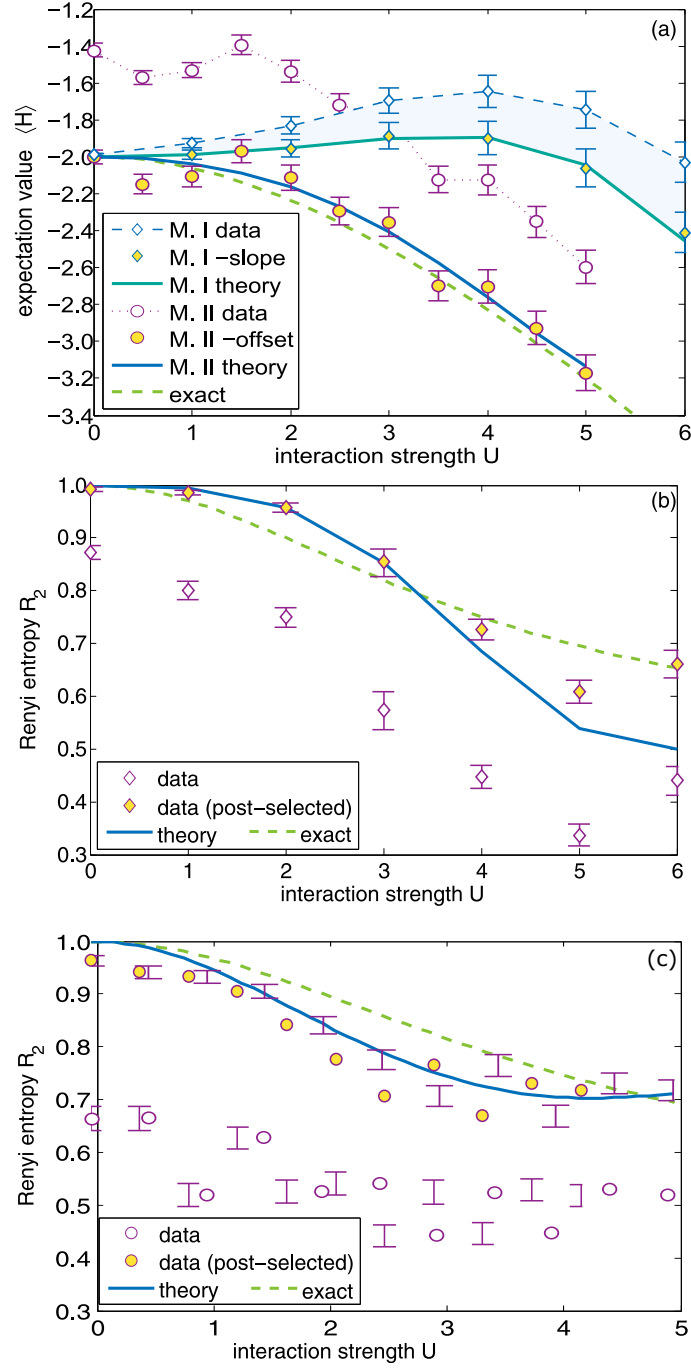


Figure 6.4: (a) Measuring the expectation value of the Fermi-Hubbard Hamiltonian using two different Trotterized evolution schemes, as explained in the text. (b) Method I is used to measure the Rényi entropy. The data is post-selected to remove failed runs with the process discussed in the main text. (c) Method II is used to measure the Rényi entropy.

To filter out failed experimental runs from our results, we developed a method to distinguish between failed and successful runs of our experiment. The additional Hadamard gates at the conclusion of the algorithm on the lower four qubits in **Figure 6.3** enable us to extract additional information from the qubit register, which we can use to post-select failed runs from successful runs. We noted that the ancilla should be measured in the bright state only if subsystems 1-A and 2-A were in different states and then swapped their states. Afterwards, the subsystems should still be in different states. If both qubits were measured in the same state and the ancilla was measured in the bright state, then the experiment clearly failed. Therefore, of the 32 possible qubit states, we can deduce that twelve should have no probability of being measured. If they are measured, it is a flag that something has gone wrong experimentally. Therefore, we can disregard such experimental runs during the data analysis. For example, if qubits 1-A, 1-B, 2-A, and 2-B are in respective states $|0\rangle|1\rangle|0\rangle|1\rangle$ and the ancilla is measured in $|1\rangle$, we know that the Fredkin gate failed to write the correct information on the ancilla and we can discard the experimental run. The data with this post-selection method is included in **Figure 6.4** (b-c). With this technique, our results match theoretical values well. This technique and others like it take advantage of symmetries inherent in the measurement scheme; they can be used on both larger quantum computers and other Hamiltonians.

Bibliography

- [1] F. Bloch. Nuclear Induction. *Physical Review*, 70(7-8):460–474, October 1946.
- [2] A. Einstein, B. Podolsky, and N. Rosen. Can Quantum-Mechanical Description of Physical Reality Be Considered Complete? *Physical Review*, 47(10):777–780, May 1935.
- [3] Richard P. Feynman. Simulating physics with computers. *Int J Theor Phys*, 21(6):467–488, June 1982.
- [4] Lov K. Grover. A Fast Quantum Mechanical Algorithm for Database Search. In *Proceedings of the Twenty-eighth Annual ACM Symposium on Theory of Computing*, STOC '96, pages 212–219, New York, NY, USA, 1996. ACM.
- [5] Peter W. Shor. Scheme for reducing decoherence in quantum computer memory. *Physical Review A*, 52(4):R2493–R2496, October 1995.
- [6] I. M. Georgescu, S. Ashhab, and Franco Nori. Quantum simulation. *Rev. Mod. Phys.*, 86(1):153–185, March 2014.
- [7] Sergey B. Bravyi and Alexei Yu. Kitaev. Fermionic Quantum Computation. *Annals of Physics*, 298(1):210–226, May 2002.
- [8] Alán Aspuru-Guzik, Anthony D. Dutoi, Peter J. Love, and Martin Head-Gordon. Simulated Quantum Computation of Molecular Energies. *Science*, 309(5741):1704–1707, September 2005.
- [9] Markus Reiher, Nathan Wiebe, Krysta M. Svore, Dave Wecker, and Matthias Troyer. Elucidating reaction mechanisms on quantum computers. *PNAS*, 114(29):7555–7560, July 2017.
- [10] Dave Wecker, Matthew B. Hastings, Nathan Wiebe, Bryan K. Clark, Chetan Nayak, and Matthias Troyer. Solving strongly correlated electron models on a quantum computer. *Physical Review A*, 92(6), December 2015.

- [11] Shantanu Debnath. *A Programmable Five Qubit Quantum Computer Using Trapped Atomic Ions*. PhD thesis, University of Maryland College Park, 2016.
- [12] Caroline Figgatt. *Building and Programming a Universal Ion Trap Quantum Computer*. PhD thesis, University of Maryland College Park, 2018.
- [13] Hans G. Dehmelt. Entropy reduction by motional sideband excitation. *Nature*, 262(5571):777, August 1976.
- [14] D. J. Wineland and Wayne M. Itano. Laser cooling of atoms. *Physical Review A*, 20(4):1521–1540, October 1979.
- [15] Wayne M. Itano and D. J. Wineland. Laser cooling of ions stored in harmonic and Penning traps. *Physical Review A*, 25(1):35–54, January 1982.
- [16] A. Steane. The ion trap quantum information processor. *Appl Phys B*, 64(6):623–643, June 1997.
- [17] David P. DiVincenzo. The Physical Implementation of Quantum Computation. *Fortschritte der Physik*, 48(9-11):771–783, 2000.
- [18] S. Olmschenk, K. C. Younge, D. L. Moehring, D. N. Matsukevich, P. Maunz, and C. Monroe. Manipulation and detection of a trapped Yb^+ hyperfine qubit. *Phys. Rev. A*, 76(5):052314, November 2007.
- [19] T. P. Harty, D. T. C. Allcock, C. J. Ballance, L. Guidoni, H. A. Janacek, N. M. Linke, D. N. Stacey, and D. M. Lucas. High-Fidelity Preparation, Gates, Memory, and Readout of a Trapped-Ion Quantum Bit. *Physical Review Letters*, 113(22), November 2014.
- [20] Stephen Crain, Clinton Cahall, Geert Vrijsen, Emma E. Wollman, Matthew D. Shaw, Varun B. Verma, Sae Woo Nam, and Jungsang Kim. High-Speed, Low-Crosstalk Detection of a Trapped $^{171}\mathrm{Yb}^+$ Ion Ancilla Qubit using Superconducting Nanowire Single Photon Detectors. *arXiv:1902.04059 [quant-ph]*, February 2019. arXiv: 1902.04059.
- [21] A. H. Myerson, D. J. Szwer, S. C. Webster, D. T. C. Allcock, M. J. Curtis, G. Imreh, J. A. Sherman, D. N. Stacey, A. M. Steane, and D. M. Lucas. High-Fidelity Readout of Trapped-Ion Qubits. *Physical Review Letters*, 100(20), May 2008.
- [22] J. P. Gaebler, T. R. Tan, Y. Lin, Y. Wan, R. Bowler, A. C. Keith, S. Glancy, K. Coakley, E. Knill, D. Leibfried, and D. J. Wineland. High-Fidelity Universal Gate Set for Be^9+ Ion Qubits. *Physical Review Letters*, 117(6), August 2016.
- [23] C. Monroe and J. Kim. Scaling the Ion Trap Quantum Processor. *Science*, 339(6124):1164–1169, March 2013.

- [24] C. Monroe, R. Raussendorf, A. Ruthven, K. R. Brown, P. Maunz, L.-M. Duan, and J. Kim. Large-scale modular quantum-computer architecture with atomic memory and photonic interconnects. *Physical Review A*, 89(2), February 2014.
- [25] David Hucul, Justin E. Christensen, Eric R. Hudson, and Wesley C. Campbell. Spectroscopy of a Synthetic Trapped Ion Qubit. *Physical Review Letters*, 119(10), September 2017.
- [26] John Hannegan, James Siverns, and Qudsia Quraishi. Quantum Frequency Conversion of Ba⁺ Photons. In *Frontiers in Optics / Laser Science*, page JW3A.60, Washington, DC, 2018. OSA.
- [27] Ye Wang, Mark Um, Junhua Zhang, Shuoming An, Ming Lyu, Jing-Ning Zhang, L.-M. Duan, Dahyun Yum, and Kihwan Kim. Single-qubit quantum memory exceeding ten-minute coherence time. *Nature Photonics*, 11(10):646–650, October 2017.
- [28] D. T. C. Allcock, T. P. Harty, M. A. Sepiol, H. A. Janacek, C. J. Ballance, A. M. Steane, D. M. Lucas, and D. N. Stacey. Dark-resonance Doppler cooling and high fluorescence in trapped Ca-43 ions at intermediate magnetic field. *New J. Phys.*, 18(2):023043, February 2016.
- [29] C. J. Foot. *Atomic physics*. Oxford master series in atomic, optical and laser physics. Oxford University Press, Oxford ;, 2005.
- [30] F. G. Major and H. G. Dehmelt. Exchange-Collision Technique for the rf Spectroscopy of Stored Ions. *Physical Review*, 170(1):91–107, June 1968.
- [31] Wolfgang Paul. Electromagnetic traps for charged and neutral particles. *Reviews of Modern Physics*, 62(3):531–540, July 1990.
- [32] M. Ahmadi, B. X. R. Alves, C. J. Baker, W. Bertsche, E. Butler, A. Capra, C. Carruth, C. L. Cesar, M. Charlton, S. Cohen, R. Collister, S. Eriksson, A. Evans, N. Evetts, J. Fajans, T. Friesen, M. C. Fujiwara, D. R. Gill, A. Gutierrez, J. S. Hangst, W. N. Hardy, M. E. Hayden, C. A. Isaac, A. Ishida, M. A. Johnson, S. A. Jones, S. Jonsell, L. Kurchaninov, N. Madsen, M. Mathers, D. Maxwell, J. T. K. McKenna, S. Menary, J. M. Michan, T. Momose, J. J. Munich, P. Nolan, K. Olchanski, A. Olin, P. Pusa, C. Ø Rasmussen, F. Robicheaux, R. L. Sacramento, M. Sameed, E. Sarid, D. M. Silveira, S. Stracka, G. Stutter, C. So, T. D. Tharp, J. E. Thompson, R. I. Thompson, D. P. van der Werf, and J. S. Wurtele. Observation of the hyperfine spectrum of antihydrogen. *Nature*, 548(7665):66–69, August 2017.
- [33] Jens Dilling, Klaus Blaum, Maxime Brodeur, and Sergey Eliseev. Penning-Trap Mass Measurements in Atomic and Nuclear Physics. *Annu. Rev. Nucl. Part. Sci.*, 68(1):45–74, October 2018.

- [34] K. Blaum, Yu N. Novikov, and G. Werth. Penning traps as a versatile tool for precise experiments in fundamental physics. *Contemporary Physics*, 51(2):149–175, March 2010.
- [35] Martin Gärttner, Justin G. Bohnet, Arghavan Safavi-Naini, Michael L. Wall, John J. Bollinger, and Ana Maria Rey. Measuring out-of-time-order correlations and multiple quantum spectra in a trapped-ion quantum magnet. *Nature Physics*, 13(8):781–786, May 2017.
- [36] A. Safavi-Naini, R. J. Lewis-Swan, J. G. Bohnet, M. Gärttner, K. A. Gilmore, J. E. Jordan, J. Cohn, J. K. Freericks, A. M. Rey, and J. J. Bollinger. Verification of a Many-Ion Simulator of the Dicke Model Through Slow Quenches across a Phase Transition. *Physical Review Letters*, 121(4), July 2018.
- [37] Jonathan Albert Mizrahi. *Ultrafast Control of Spin and Motion in Trapped Ions*. PhD thesis, University of Maryland College Park, 2013.
- [38] D. J. Berkeland, J. D. Miller, J. C. Bergquist, W. M. Itano, and D. J. Wineland. Minimization of ion micromotion in a Paul trap. *Journal of Applied Physics*, 83(10):5025–5033, April 1998.
- [39] D.F.V. James. Quantum dynamics of cold trapped ions with application to quantum computation. *Applied Physics B: Lasers and Optics*, 66(2):181–190, February 1998.
- [40] S. R. Bastin and Tony E. Lee. Ion crystals in anharmonic traps. *Journal of Applied Physics*, 121(1):014312, January 2017.
- [41] T. P. Perng and C. J. Altstetter. Hydrogen effects in austenitic stainless steels. *Materials Science and Engineering: A*, 129(1):99–107, October 1990.
- [42] Hiroji Katsuta and Kazuo Furukawa. Hydrogen and Deuterium Transport through Type 304 Stainless Steel at Elevated Temperatures. *Journal of Nuclear Science and Technology*, 18(2):143–151, February 1981.
- [43] Manoj Kumar Gupta, Abhinav Priyadarshi, and Ziauddin Khan. Hydrogen in Stainless Steel as Killing Agent for UHV: A Review. *Materials Today: Proceedings*, 2(4-5):1074–1081, 2015.
- [44] A. Zverev and H. Blinchikoff. Realization of a Filter with Helical Components. *IRE Transactions on Component Parts*, 8(3):99–110, September 1961.
- [45] W. W. Macalpine and R. O. Schildknecht. Coaxial Resonators with Helical Inner Conductor. *Proceedings of the IRE*, 47(12):2099–2105, December 1959.
- [46] G.-D. Lin, S.-L. Zhu, R. Islam, K. Kim, M.-S. Chang, S. Korenblit, C. Monroe, and L.-M. Duan. Large-scale quantum computation in an anharmonic linear ion trap. *EPL (Europhysics Letters)*, 86(6):60004, June 2009.

- [47] Chr. Balzer, A. Braun, T. Hannemann, Chr. Paape, M. Ettler, W. Neuhauser, and Chr. Wunderlich. Electrodynamically trapped Yb^+ ions for quantum information processing. *Phys. Rev. A*, 73(4):041407, April 2006.
- [48] William D. Phillips and Harold Metcalf. Laser Deceleration of an Atomic Beam. *Physical Review Letters*, 48(9):596–599, March 1982.
- [49] A. S. Bell, P. Gill, H. A. Klein, A. P. Levick, Chr. Tamm, and D. Schnier. Laser cooling of trapped ytterbium ions using a four-level optical-excitation scheme. *Physical Review A*, 44(1):R20–R23, July 1991.
- [50] A. Seif, K.A. Landsman, N.M. Linke, C. Figgatt, C. Monroe, and M. Hafezi. Machine learning assisted readout of trapped-ion qubits. *J. Phys. B: At. Mol. Opt. Phys.*, 51(17):174006, 2018.
- [51] Philip Richerme. Two-dimensional ion crystals in radio-frequency traps for quantum simulation. *Physical Review A*, 94(3), September 2016.
- [52] S. Debnath, N. M. Linke, C. Figgatt, K. A. Landsman, K. Wright, and C. Monroe. Demonstration of a small programmable quantum computer with atomic qubits. *Nature*, 536(7614):63–66, August 2016.
- [53] T. Monz, K. Kim, W. Hänsel, M. Riebe, A. S. Villar, P. Schindler, M. Chwalla, M. Hennrich, and R. Blatt. Realization of the Quantum Toffoli Gate with Trapped Ions. *Physical Review Letters*, 102(4), January 2009.
- [54] Timothy Andrew Manning. *Quantum Information Processing with Trapped Ion Chains*. PhD thesis, University of Maryland College Park, 2014.
- [55] S. Debnath, N. M. Linke, S.-T. Wang, C. Figgatt, K. A. Landsman, L.-M. Duan, and C. Monroe. Observation of Hopping and Blockade of Bosons in a Trapped Ion Spin Chain. *Physical Review Letters*, 120(7), February 2018.
- [56] D. Porras and J. I. Cirac. Bose-Einstein Condensation and Strong-Correlation Behavior of Phonons in Ion Traps. *Physical Review Letters*, 93(26), December 2004.
- [57] Alexander Mering, Michael Fleischhauer, Peter A. Ivanov, and Kilian Singer. Analytic approximations to the phase diagram of the Jaynes-Cummings-Hubbard model. *Physical Review A*, 80(5), November 2009.
- [58] P. A. Ivanov, S. S. Ivanov, N. V. Vitanov, A. Mering, M. Fleischhauer, and K. Singer. Simulation of a quantum phase transition of polaritons with trapped ions. *Physical Review A*, 80(6), December 2009.
- [59] P J Lee, K-A Brickman, L Deslauriers, P C Haljan, L-M Duan, and C Monroe. Phase control of trapped ion quantum gates. *Journal of Optics B: Quantum and Semiclassical Optics*, 7(10):S371–S383, October 2005.

- [60] J. I. Cirac and P. Zoller. Quantum Computations with Cold Trapped Ions. *Phys. Rev. Lett.*, 74(20):4091–4094, May 1995.
- [61] Chris Monroe, D. M. Meekhof, B. E. King, Wayne M. Itano, and David J. Wineland. Demonstration of a fundamental quantum logic gate. *Physical review letters*, 75(25):4714, 1995.
- [62] Klaus Mølmer and Anders Sørensen. Multiparticle entanglement of hot trapped ions. *Physical Review Letters*, 82(9):1835, 1999.
- [63] E. Solano, R. L. de Matos Filho, and N. Zagury. Deterministic Bell states and measurement of the motional state of two trapped ions. *Phys. Rev. A*, 59(4):R2539–R2543, April 1999.
- [64] G. J. Milburn, S. Schneider, and D. F. V. James. Ion trap quantum computing with warm ions. *Fortschritte der Physik*, 48(9-11):801–810, 2000.
- [65] D.J. Wineland, C. Monroe, W.M. Itano, D. Leibfried, B.E. King, and D.M. Meekhof. Experimental issues in coherent quantum-state manipulation of trapped atomic ions. *Journal of Research of the National Institute of Standards and Technology*, 103(3):259, May 1998.
- [66] D M Meekhof, D Leibfried, C Monroe, B E King, W M Itano, and D J Wineland. Experimental Creation and Measurement of Motional Quantum States of a Trapped Ion. *Brazilian Journal of Physics*, 27(2):15, 1997.
- [67] C. Figgatt, D. Maslov, K. A. Landsman, N. M. Linke, S. Debnath, and C. Monroe. Complete 3-Qubit Grover search on a programmable quantum computer. *Nature Communications*, 8(1):1918, December 2017.
- [68] K. A. Landsman, C. Figgatt, T. Schuster, N. M. Linke, B. Yoshida, N. Y. Yao, and C. Monroe. Verified quantum information scrambling. *Nature*, 567(7746):61–65, March 2019.
- [69] G Pagano, P W Hess, H B Kaplan, W L Tan, P Richerme, P Becker, A Kyprianidis, J Zhang, E Birkelbaw, M R Hernandez, Y Wu, and C Monroe. Cryogenic trapped-ion system for large scale quantum simulation. *Quantum Science and Technology*, 4(1):014004, October 2018.
- [70] T. Choi, S. Debnath, T. A. Manning, C. Figgatt, Z.-X. Gong, L.-M. Duan, and C. Monroe. Optimal Quantum Control of Multimode Couplings between Trapped Ion Qubits for Scalable Entanglement. *Physical Review Letters*, 112(19), May 2014.
- [71] Norbert M. Linke, Sonika Johri, Caroline Figgatt, Kevin A. Landsman, Anne Y. Matsuura, and Christopher Monroe. Measuring the Renyi entropy of a two-site Fermi-Hubbard model on a trapped ion quantum computer. *arXiv:1712.08581 [quant-ph]*, December 2017. arXiv: 1712.08581.

- [72] Christian Kokail, Christine Maier, Rick van Bijnen, Tiff Brydges, Manoj K. Joshi, Petar Jurcevic, Christine A. Muschik, Pietro Silvi, Rainer Blatt, Christian F. Roos, and Peter Zoller. Self-Verifying Variational Quantum Simulation of the Lattice Schwinger Model. *arXiv:1810.03421 [cond-mat, physics:quant-ph]*, October 2018. arXiv: 1810.03421.
- [73] J. True Merrill, S. Charles Doret, Grahame Vittorini, J. P. Addison, and Kenneth R. Brown. Transformed composite sequences for improved qubit addressing. *Physical Review A*, 90(4), October 2014.
- [74] Daniel C. Murphy and Kenneth R. Brown. Controlling error orientation to improve quantum algorithm success rates. *Physical Review A*, 99(3), March 2019.
- [75] Kenneth R. Brown, Aram W. Harrow, and Isaac L. Chuang. Arbitrarily accurate composite pulse sequences. *Physical Review A*, 70(5), November 2004.
- [76] Yao Lu, Shuaining Zhang, Kuan Zhang, Wentao Chen, Yangchao Shen, Jialiang Zhang, Jing-Ning Zhang, and Kihwan Kim. Scalable global entangling gates on arbitrary ion qubits. *arXiv:1901.03508 [physics, physics:quant-ph]*, January 2019. arXiv: 1901.03508.
- [77] Yunseong Nam, Jwo-Sy Chen, Neal C. Pienti, Kenneth Wright, Conor Delaney, Dmitri Maslov, Kenneth R. Brown, Stewart Allen, Jason M. Amini, Joel Apisdorf, Kristin M. Beck, Aleksey Blinov, Vandiver Chaplin, Mika Chmielewski, Coleman Collins, Shantanu Debnath, Andrew M. Ducore, Kai M. Hudek, Matthew Keesan, Sarah M. Kreikemeier, Jonathan Mizrahi, Phil Solomon, Mike Williams, Jaime David Wong-Campos, Christopher Monroe, and Jungsang Kim. Ground-state energy estimation of the water molecule on a trapped ion quantum computer. *arXiv:1902.10171 [quant-ph]*, February 2019. arXiv: 1902.10171.
- [78] K. Wright, K. M. Beck, S. Debnath, J. M. Amini, Y. Nam, N. Grzesiak, J.-S. Chen, N. C. Pienti, M. Chmielewski, C. Collins, K. M. Hudek, J. Mizrahi, J. D. Wong-Campos, S. Allen, J. Apisdorf, P. Solomon, M. Williams, A. M. Ducore, A. Blinov, S. M. Kreikemeier, V. Chaplin, M. Keesan, C. Monroe, and J. Kim. Benchmarking an 11-qubit quantum computer. *arXiv:1903.08181 [quant-ph]*, March 2019. arXiv: 1903.08181.
- [79] E. I. Gordon. A Review of Acoustooptical Deflection and Modulation Devices. *Appl. Opt.*, AO, 5(10):1629–1639, October 1966.
- [80] A. C. Lee, J. Smith, P. Richerme, B. Neyenhuis, P. W. Hess, J. Zhang, and C. Monroe. Engineering large Stark shifts for control of individual clock state qubits. *Physical Review A*, 94(4), October 2016.

- [81] N.M. Linke, D. Maslov, M. Roetteler, S. Debnath, C. Figgatt, K.A. Landsman, K. Wright, and C. Monroe. Experimental comparison of two quantum computing architectures. *Proceedings of the National Academy of Sciences*, 114(13):3305–3310, March 2017.
- [82] N.M. Linke, M. Gutierrez, K.A. Landsman, C. Figgatt, S. Debnath, K.R. Brown, and C. Monroe. Fault-tolerant quantum error detection. *Science Advances*, 3(10):e1701074, October 2017.
- [83] R. Islam, W. C. Campbell, T. Choi, S. M. Clark, C. W. S. Conover, S. Debnath, E. E. Edwards, B. Fields, D. Hayes, D. Hucul, I. V. Inlek, K. G. Johnson, S. Korenblit, A. Lee, K. W. Lee, T. A. Manning, D. N. Matsukevich, J. Mizrahi, Q. Quraishi, C. Senko, J. Smith, and C. Monroe. Beat note stabilization of mode-locked lasers for quantum information processing. *Optics Letters*, 39(11):3238, June 2014.
- [84] K. G. Johnson, J. D. Wong-Campos, A. Restelli, K. A. Landsman, B. Neyenhuis, J. Mizrahi, and C. Monroe. Active stabilization of ion trap radiofrequency potentials. *Review of Scientific Instruments*, 87(5):053110, May 2016.
- [85] J. Smith, A. Lee, P. Richerme, B. Neyenhuis, P. W. Hess, P. Hauke, M. Heyl, D. A. Huse, and C. Monroe. Many-body localization in a quantum simulator with programmable random disorder. *Nature Physics*, 12(10):907–911, October 2016.
- [86] Todd J. Green and Michael J. Biercuk. Phase-Modulated Decoupling and Error Suppression in Qubit-Oscillator Systems. *Physical Review Letters*, 114(12), March 2015.
- [87] P.H. Leung, K.A. Landsman, C. Figgatt, N.M. Linke, C. Monroe, and K.R. Brown. Robust 2-Qubit Gates in a Linear Ion Crystal Using a Frequency-Modulated Driving Force. *Physical Review Letters*, 120(2), January 2018.
- [88] Pak Hong Leung and Kenneth R. Brown. Entangling an arbitrary pair of qubits in a long ion crystal. *Physical Review A*, 98(3), September 2018.
- [89] Shi-Liang Zhu, C. Monroe, and L.-M. Duan. Trapped Ion Quantum Computation with Transverse Phonon Modes. *Physical Review Letters*, 97(5), August 2006.
- [90] Yukai Wu, Sheng-Tao Wang, and L.-M. Duan. Noise analysis for high-fidelity quantum entangling gates in an anharmonic linear Paul trap. *Physical Review A*, 97(6), June 2018.
- [91] D. Zhu, N. M. Linke, M. Benedetti, K. A. Landsman, N. H. Nguyen, C. H. Alderete, A. Perdomo-Ortiz, N. Korda, A. Garfoot, C. Brecque, L. Egan, O. Perdomo, and C. Monroe. Training of Quantum Circuits on a Hybrid Quantum Computer. *arXiv:1812.08862 [quant-ph]*, December 2018. arXiv: 1812.08862.

- [92] N. Solmeyer, N.M. Linke, C. Figgatt, K.A. Landsman, R. Balu, G. Siopsis, and C. Monroe. Demonstration of a Bayesian quantum game on an ion-trap quantum computer. *Quantum Sci. Technol.*, 3(4):045002, 2018.
- [93] Patrick Hayden and John Preskill. Black holes as mirrors: quantum information in random subsystems. *J. High Energy Phys.*, 2007(09):120, 2007.
- [94] Alexei Kitaev. Hidden correlations in the hawking radiation and thermal noise, November 2014.
- [95] Beni Yoshida and Alexei Kitaev. Efficient decoding for the Hayden-Preskill protocol. *arXiv:1710.03363 [hep-th, physics:quant-ph]*, October 2017. arXiv: 1710.03363.
- [96] Beni Yoshida and Norman Y. Yao. Disentangling Scrambling and Decoherence via Quantum Teleportation. *Physical Review X*, 9(1), January 2019.
- [97] V. Nebendahl, H. Häffner, and C. F. Roos. Optimal control of entangling operations for trapped-ion quantum computing. *Physical Review A*, 79(1), January 2009.
- [98] Charles H. Bennett, Gilles Brassard, Claude Crépeau, Richard Jozsa, Asher Peres, and William K. Wootters. Teleporting an unknown quantum state via dual classical and Einstein-Podolsky-Rosen channels. *Physical Review Letters*, 70(13):1895–1899, March 1993.
- [99] Michael A. Nielsen and Isaac L. Chuang. *Quantum computation and quantum information*. Cambridge University Press, Cambridge ;, 10th anniversary ed. edition, 2010.
- [100] Landauer Rolf, Welland Mark Edward, and Gimzewski James Kazimierz. Is quantum mechanics useful? *Philosophical Transactions of the Royal Society of London. Series A: Physical and Engineering Sciences*, 353(1703):367–376, December 1995.
- [101] Wojciech H. Zurek. Preferred States, Predictability, Classicality and the Environment-Induced Decoherence. *Prog Theor Phys*, 89(2):281–312, February 1993.
- [102] Steane Andrew. Multiple-particle interference and quantum error correction. *Proceedings of the Royal Society of London. Series A: Mathematical, Physical and Engineering Sciences*, 452(1954):2551–2577, November 1996.
- [103] A. R. Calderbank and Peter W. Shor. Good quantum error-correcting codes exist. *Physical Review A*, 54(2):1098–1105, August 1996.
- [104] Natalie C. Brown and Kenneth R. Brown. Comparing Zeeman qubits to hyperfine qubits in the context of the surface code: $^{174}\mathrm{Yb}^{+}$ and $^{171}\mathrm{Yb}^{+}$. *Phys. Rev. A*, 97(5):052301, May 2018.

- [105] Peter W. Shor. Fault-tolerant quantum computation. *arXiv:quant-ph/9605011*, May 1996. arXiv: quant-ph/9605011.
- [106] Muyuan Li, Daniel Miller, and Kenneth R. Brown. Direct measurement of Bacon-Shor code stabilizers. *Physical Review A*, 98(5), November 2018.
- [107] H. Bombin and M. A. Martin-Delgado. Topological Quantum Distillation. *Physical Review Letters*, 97(18), October 2006.
- [108] Dave Bacon. Operator quantum error-correcting subsystems for self-correcting quantum memories. *Physical Review A*, 73(1), January 2006.
- [109] James P Clemens, Shabnam Siddiqui, and Julio Gea-Banacloche. Quantum error correction against correlated noise. *PHYSICAL REVIEW A*, page 9, 2004.
- [110] Sonika Johri, Damian S. Steiger, and Matthias Troyer. Entanglement spectroscopy on a quantum computer. *Physical Review B*, 96(19), November 2017.
- [111] Matthew B. Hastings, Iván González, Ann B. Kallin, and Roger G. Melko. Measuring Renyi Entanglement Entropy in Quantum Monte Carlo Simulations. *Physical Review Letters*, 104(15), April 2010.
- [112] R. Cleve, A. Ekert, C. Macchiavello, and M. Mosca. Quantum algorithms revisited. *Proceedings of the Royal Society of London A: Mathematical, Physical and Engineering Sciences*, 454(1969):339–354, January 1998.
- [113] Hubbard J. and Flowers Brian Hilton. Electron correlations in narrow energy bands. *Proceedings of the Royal Society of London. Series A. Mathematical and Physical Sciences*, 276(1365):238–257, November 1963.
- [114] Hubbard J. and Flowers Brian Hilton. Electron correlations in narrow energy bands. II. The degenerate band case. *Proceedings of the Royal Society of London. Series A. Mathematical and Physical Sciences*, 277(1369):237–259, January 1964.
- [115] Dave Wecker, Matthew B. Hastings, and Matthias Troyer. Progress towards practical quantum variational algorithms. *Physical Review A*, 92(4), October 2015.
- [116] Anton Mazurenko, Christie S. Chiu, Geoffrey Ji, Maxwell F. Parsons, Márton Kanász-Nagy, Richard Schmidt, Fabian Grusdt, Eugene Demler, Daniel Greif, and Markus Greiner. A cold-atom Fermi–Hubbard antiferromagnet. *Nature*, 545(7655):462–466, May 2017.
- [117] Michael Messer, Kilian Sandholzer, Frederik Görg, Joaquín Minguzzi, Rémi Desbuquois, and Tilman Esslinger. Floquet Dynamics in Driven Fermi-Hubbard Systems. *Physical Review Letters*, 121(23), December 2018.

- [118] W. Vincent Liu, Frank Wilczek, and Peter Zoller. Spin-dependent Hubbard model and a quantum phase transition in cold atoms. *Physical Review A*, 70(3), September 2004.
- [119] P. Jordan and E. Wigner. Über das Paulische äquivalenzverbot. *Z. Physik*, 47(9):631–651, September 1928.
- [120] Andrew Tranter, Peter J. Love, Florian Mintert, and Peter V. Coveney. A Comparison of the Bravyi–Kitaev and Jordan–Wigner Transformations for the Quantum Simulation of Quantum Chemistry. *J. Chem. Theory Comput.*, 14(11):5617–5630, November 2018.
- [121] Tameem Albash and Daniel A. Lidar. Adiabatic quantum computation. *Rev. Mod. Phys.*, 90(1):015002, January 2018.
- [122] Yin Sun, Jun-Yi Zhang, Mark S. Byrd, and Lian-Ao Wu. Adiabatic Quantum Simulation Using Trotterization. *arXiv:1805.11568 [quant-ph]*, May 2018. arXiv: 1805.11568.
- [123] John Preskill. Quantum Computing in the NISQ era and beyond. *Quantum*, 2:79, August 2018.
- [124] Kristan Temme, Sergey Bravyi, and Jay M. Gambetta. Error Mitigation for Short-Depth Quantum Circuits. *Physical Review Letters*, 119(18), November 2017.